DEVELOPMENT AND APPLICATION OF A NEW SET OF TDM-BASED SEMI-ANALYTICAL SOLUTIONS TO THE PROBLEM OF PRESSURE INTERFERENCE IN A HYDRAULICALLY-FRACTURED RESERVOIR

A Thesis

by

NIWIT ANANTRAKSAKUL

Submitted to the Office of Graduate and Professional Studies of
Texas A&M University
in partial fulfillment of the requirements for the degree of

MASTER OF SCIENCE

Chair of Committee,	George J. Moridis
Co-Chair of Committee,	Thomas A. Blasingame
Committee Member,	Zhengdong Cheng
Head of Department,	Jeff Spath

May 2020

Major Subject: Petroleum Engineering

ABSTRACT

The analysis of production from fractured Ultra-Low Permeability (ULP) reservoirs is routinely conducted using numerical simulation, which requires large 3D grids, a very large number of time-steps, numerous input data, long execution times, and the specialized computational expertise. The main objective of this research is to develop a set of new semi-analytical results that reduce or eliminate the need for spatial and temporal discretization of numerical models and address their shortcomings, thus providing fast and simpler alternatives that can deliver reliable results for the analysis of production and reservoir performance, as well as for history matching.

The new set of solutions is based on variants of a hybrid analytical-numerical approach called the Transformational Decomposition Method (TDM) that involves successive applications of Finite Cosine Transforms for the elimination of multiple dimensions in space, and Laplace Transforms for the elimination of the time variable. Application of this method reduces the 3D diffusivity equation of the nearly-incompressible oil flow into either an algebraic equation (referred to as TD-0D) or a simple Ordinary Differential Equation (ODE) in the x-dimension (referred to as TD-1D). The strongly non-linear 3D flow of compressible gas does not allow the application of Laplace transforms, leading to the development and application of the Partial Transformational Decomposition Method (PTDM), which reduces the 3D gas diffusivity equation into either a simple ODE in time (referred to as PTD-0D) or a 1D Partial Differential Equation (PDE) in space and time

(referred to as PTD-1D). Both the TDM and PTDM solutions exist in multi-transformed space and/or time environments, from which they are inverted numerically to obtain solutions at any point in space and time through a process that vastly simplifies and decreases the size of the simulation problem, as well as the execution time.

Both the TDM and the PTDM solution were coded in a FORTRAN90. Using a 3D stencil (the minimum repeatable element in hydraulically-fractured reservoirs produced by horizontal wells), solutions over an extended production period and covering a substantial pressure drop were obtained for (a) a range of isotropic and anisotropic matrices and fracture properties, (b) constant and time-variable flow rates and bottomhole pressure regimes, and (c) combinations of Stimulated Reservoir Volume (SRV) and non-SRV subdomains. The results were compared to the solutions from the FTSim code -- a fully-implicit 3D simulator -- using a finely-discretized (high-definition) 3D domain. The TDM results of oil flow and production were shown to be in excellent agreement with the FTSim numerical solutions during the entire production periods. The PTDM performance was not uniform across the time spectrum: the FTSim solutions were in excellent agreement with the PTD-1D results at any time during production and with the PTD-0D solutions at early times, but the PTD-0D performance deteriorated at later times.

DEDICATION

This work is dedicated to my father, my mother, and my little brother who always give me unconditional love and support.

ACKNOWLEDGEMENTS

First and foremost, I would like to thank the chair of my committee, Dr. George Moridis, for his advice, his inspiration for this work, and his dedication to me and to my project. Dr. Moridis has given me this valuable opportunity and experience that I would have never been able to achieve on my own. I am eternally grateful for his supervision and guidance.

I also would like to thank the co-chair of my committee, Dr. Tom Blasingame, for his kind support and also his dedication to help me to improve as a person. Not to mention that Dr. Blasingame was the first person who gave me an opportunity to evolve professionally by inviting me to work in this research group. I also thank Dr. Blasingame for his "perfection is the standard" work ethic which always reminds me that I must always give my absolute best effort.

Lastly, I would like to thank Dr. Zhengdong Cheng for serving as the external member of my advisory committee.

CONTRIBUTORS AND FUNDING SOURCES

Contributors

This work was supervised by a thesis committee consisting of Professor Moridis [advisor] and Professor Blasingame [co-advisor] of the Department of Petroleum Engineering, and Professor Cheng of the Department of Chemical Engineering.

The computations in Case 6 (denoted by an asterisk in **Table 2.2**) were provided directly by Professor Moridis [advisor].

All other work conducted for the thesis was completed by Niwit Anantraksakul [student] under the close supervision by Professor Moridis [advisor].

Funding Sources

This graduate study was supported by the Crisman Institute for Petroleum Research at Texas A&M University through project 7.01.18.

TABLE OF CONTENTS

Page

LIST OF FIGURES

Page

LIST OF TABLES

Page

CHAPTER I

INTRODUCTION AND LITERATURE REVIEW

1.1 Background

The advent and advances in reservoir stimulation technologies (mainly hydraulic fracturing) since the beginning of the 21st century have resulted in an explosive growth in the production of hydrocarbons from unconventional resources such as tight sand and shale reservoirs. Such stimulation methods have enabled production from reservoirs that were previously considered uneconomical (or even technically impossible) because of ultra-low permeability (ULP). Thus, oil production from ULP reservoirs as a fraction of total crude oil production in the U.S. has experienced a dramatic growth, from practically nil in 2005 to 59% in 2018 (U.S. EIA, 2019), when daily production at the end of the year reached 6.5 million barrels. Additionally, the stimulation process has been so successful that currently, the majority of the natural gas production in the U.S. comes from shale gas and tight oil plays (US DOE, 2019).

The importance of tight-gas/oil and shale-gas/oil reservoirs as energy resources necessitates the ability to accurately estimate reserves, to analyze and interpret well performance, and to evaluate, design, manage and predict production from such systems over a wide range of time frames and spatial scales. Analytical and numerical models provide the necessary tools for these activities. Simple analytical and semi-analytical

models to predict flow in fractured shale-gas and tight-gas reservoirs have been proposed early on (*e.g.*, Gringarten, 1971; Gringarten et al., 1974; Blasingame and Poe, 1993), but the geometry they described was inflexible and limited to single fractures, thus limiting severely their applicability. Since then, more powerful analytical and semi-analytical models for multi-fractured horizontal wells have been developed (Medeiros et al., 2006; Bello and Wattenbarger, 2008; Mattar, 2008; Anderson et al., 2010), but these suffer from a fixed and inflexible geometry that limit their applications to very limited configurations of the fracture-matrix-well system that do not lend themselves to critical engineering activities such as predicting well and reservoir performance and the analysis of well tests. In the case of gas flow, the problem is further complicated by the strong dependence of the gas properties that inserts strong non-linearities into the equation of flow and significantly reduces the scope for, and validity of, analytical solutions.

The complex geometries and the heterogeneity in the properties of the matrix, of the hydraulic or native fractures and of the well in such multi-fractured systems have led to the development of numerical reservoir simulators that address the particularities of these systems. These constitute powerful tools that have significant advantages over analytical solutions, being the only realistic option in most (if not all) cases as they can routinely handle the complexities of real-life systems without the need for simplifications of geometry, boundaries, heterogeneity and fluid properties. They do so by using fine spatial and temporal discretization to capture complex geometries and accurately describe changes in the properties and composition of the reservoir fluids (an impossible task for

analytical solutions), resulting in a large number of space and time subdomains (cells or elements) into which the reservoir and the production period are subdivided. The equations of fluid mass and energy balance need to be solved in each one of these cells, resulting in matrix equations that are solved simultaneously.

Recent numerical studies (Cipolla et al., 2009; Miller et al., 2010; Freeman, 2010; Freeman et al., 2009; 2013; Moridis and Freeman, 2014; Moridis et al., 2017) conducted sensitivity analyses using high fidelity grids to identify the most important mechanisms and factors that affect shale-gas and shale-oil reservoir performance. Such numerical models are a very powerful tool in the solution of the problem of flow, production and pressure interference in multi-fractured systems involving horizontal wells. They have the ability to describe systems of complex (even arbitrary) geometry with challenging boundary conditions and can easily handle any kind of non-linearity (especially those arising from strong fluid compressibility regimes and multi-phase flows). Thus, such methods are widely used – and may even be considered indispensable — in extensive forward and backward (history-matching) studies analyzing the flow through, and production of fluids from, fractured hydrocarbon reservoirs such as the unconventional (shale gas and shale oil) plays that have exploded in importance as energy resources over the last decade.

Despite their power and importance, numerical modeling and its applications poses some significant challenges in forward modeling and, more importantly, in history-matching

studies. Domain discretization for accurately capturing the system behavior is an art as well as a science, and it is a time-consuming process that requires significant experience and expertise. The numerical simulation process (a) has significant input data requirements, (b) requires the involvement of specially-trained individuals, (c) necessitates the solution of matrix equations that may involve millions of equations that are often beyond the capabilities of serial simulators on most desktop computers, requiring the use of codes of parallel architecture and their application on clusters and supercomputers, (d) requires long execution times and specialized skills for the analysis and interpretation of the outputs, and, for all these reasons and more, (e) is cumbersome, and often arduous. In the case of ULP gas reservoirs, the problem is exacerbated by the high compressibility of the fluid (and the associated strong non-linearity) and the extremely low permeability, which lead to very steep gradients and solution surfaces and require extremely fine discretization (often on the order of mm in the vicinity of the hydraulic fractures) in order to accurately capture the curvature of the flow lines and the transient flow regimes (Freeman et al., 2013; Moridis and Freeman, 2014). These challenges make predictions and the analysis of production data slow and expensive, and often beyond the reach of practicing engineers without the necessary specialized background.

1.2 General Equation of Flow

The flow of fluids through porous media and fractured media can be described by the following diffusivity equation that reflects the mass balance of the fluid within and across a control volume:

$$\nabla \cdot \left[k \frac{\rho}{\mu} \left(\nabla p - \rho g \nabla z \right) \right] = \frac{\partial}{\partial t} \left(\rho \phi \right) \quad \text{..... (1.1)}$$

where

g = gravitational acceleration, (= 9.806) m/s^2

k = is permeability, m^2

μ = is fluid viscosity, Pa-s

p = is pressure, Pa

ϕ = is porosity, fraction

ρ = is fluid density, kg/m^3

t = is time, sec

z = is elevation, m

Eq. 1.1 applies to all fluids, *i.e.*, liquid and gaseous and is valid while Darcy's law (which is represented on the left-hand side of the equation) is valid, (*i.e.*, when the fluid flow is laminar). The solution of this diffusivity equation can be obtained with the various methods that were briefly discussed in the previous section, some of which are dictated by the properties of the fluids. Thus, liquids have very low fluid compressibility (*i.e.*, very

weak dependence on pressure) and their viscosity is practically insensitive to pressure, attributes that allow linearization of Eq. 1.1 and the development of analytical solutions with relatively few assumptions and simplifications. Conversely, the high compressibility of gases and the strong dependence of their density and viscosity on pressure preclude the easy development of closed-form analytical solutions, which are made possible only after the introduction of complex artificial variables and are valid only within the limited range of pressures in which the significant assumptions and simplifications (that were necessary for the development of the solutions) are valid.

The effort to develop analytical or semi-analytical solutions to the problem of flow through multi-fractured ULP reservoirs produced by horizontal wells faces particular challenges: strong heterogeneities, defined by significant differences in the properties of (a) the proppant-impregnated hydraulic fractures, (b) the Stimulated Reservoir Volume (SRV) and (c) the virgin (unfractured) matrix of the ULP reservoir, in addition to 3D flows that do not lend themselves to simplification and complex boundary conditions. Thus, for reasons already discussed, numerical solutions are currently the most commonly-used methods, and often the only option, to solve the problem of flow in multi-fractured ULP systems. The main objective of this study is to develop a powerful semi-analytical alternative to the numerical simulation of this problem.

1.3 Methods Eliminating the Temporal Discretization

Because of the aforementioned difficulties and shortcomings, several attempts have been made to minimize the problems posed by the use of numerical simulators by reducing (at a minimum) the simulation times while maintaining their power and flexibility. Reduction in the space and time discretization were the obvious first targets because these were the main reasons for the significant computational effort of standard numerical models. New numerical approaches, such as the use of fully implicit schemes that allowed fewer and longer time steps (*i.e.,* coarser time discretization) and fewer computations were introduced as the first step in this direction. These approaches maintained the high level of spatial discretization to attain the desired spatial resolution, thus allowing accurate description of a reservoir geometry and heterogeneity.

The next step in this direction was the complete elimination of the need for time discretization through the introduction of Laplace transforms and their coupling with conventional space discretization schemes. Thus, Sudicky (1989) coupled Laplace transforms (LTs) with a standard Galerkin-based Finite Element space discretization method to solve the problem of contaminant transport in groundwater that involved advection, diffusion and mechanical dispersion. Later, the LTFD model of Moridis and Reddell (1991a) and Moridis et al. (1994) coupled standard Finite Difference (FD) models with LT to solve the problems of slightly compressible liquids in geologic media. LTs were also coupled with other spatial discretization methods such as boundary elements

(Moridis and Reddell, 1991b; Moridis, 1992) and multi-quadrics (Moridis and Kansa, 1992; 1994). All these methods to provided solutions that were numerical in space (and thus capable of describing heterogeneity at any desired level of resolution) and analytical in time at any desired time. Because of the strong (and intractable) non-linearities associated with multi-phase flows, these models could only resolve single-phase, single-component isothermal flows.

1.4 Methods Eliminating Both the Temporal and the Spatial Discretization

Because of the difficulty of the endeavor, there have been far fewer attempts to eliminate both the space and time discretization in the solutions of PDEs of flow through porous media. Goode and Thambynayagam (1987) provided a first window in this approach in an analytical/semi-analytical (A/SA) method that combined LTs and Finite Cosine Transforms (FCTs) to solve the 3D problem of oil production using a horizontal well. Their solution and its approximations were analytical in space and time, and was sufficiently general to account for anisotropy (although not for spatial heterogeneity).

The Transformational Decomposition Method (TDM) proposed by Moridis (1995) followed the same general approach in the solution of multi-dimensional problems: it first used LTs to eliminate the need for time discretization, followed by successive FCTs to eliminate the spatial coordinates in either the entire domain (in homogeneous systems) or in heterogeneous subdomains that were analytically interconnected. TDM provided A/SA solutions at any point in space and time without the need for discretization. These solutions

were analytical in space (obtained through successive inverse FCTs) and semi-analytical in time: the inability to derive closed-form equations from the inversion of the Laplace-space solutions necessitated the use of numerical inversions to obtain the solutions in time.

Recently, a powerful new semi-analytical method for describing flow to a well in a multi-fractured reservoir was proposed by Stalgorova and Mattar (2013). Their solution is applicable to both liquids and gases, involves subdividing the heterogeneous domain in five 2D regions in an approach similar to that of earlier work (Medeiros et al., 2010; Brown et al., 2011), and assumes that flow in each region is linear (1D) and parallel to the coordinate axes of the system. In the solution of several problems, the method of Stalgorova and Mattar (2013) showed some very good agreements with results from a numerical simulator, but still suffered from weaknesses that are associated with the geometry of the system (as it affects the flow regime). In addition to the assumption of linear 1D flows in 2D subdomains (a simplification that cannot describe the curvature of flow lines in any of the subdomains and especially close to the fracture and the well), their method (a) cannot accurately describe flow in 3D domains but relies on a "curvature skin" approximation, (b) cannot describe partial vertical fracture penetration into the reservoir, (c) assumes that the well lies on the plane of symmetry at the middle of the reservoir thickness and (d) can only consider fluid production at a constant well rate.

1.5 Impetus for the Study

Because of the aforementioned difficulties posed by standard numerical methods, there would be significant benefit in the availability of fast, yet robust, A/SA alternatives that can provide some basic information for the analysis of the properties and behavior of multi-fractured horizontal well systems under production without having to resort to numerical modeling. A new generation of analytical or semi-analytical solutions that eliminate space and time discretization and are free of the limitations of the earlier, simplest solutions to this problem can fulfill that role. Note that such solutions would require limited data inputs and would be expected to be fast because they do not involve domain discretization and solution of large matrix equations, but may not necessarily be "simple" in terms of their functional forms. However, they would be invariably simple in their application in a computer application and readily usable by non-specialist engineers.

A further motivation for the development of such capabilities comes from the recent interest in the study of problems in which fine scale features are unknown, making high fidelity numerical solution inefficient. For hydraulic fractured reservoirs, the subdivision of the reservoir into subdomains with characteristic properties (permeability) has proven popular in currently available A/SA solutions (Medeiros et al., 2010; Brown et al., 2011; Stalgorova and Mattar, 2013), but also suffers from the significant limitations that the study of Stalgorova and Mattar (2013) clearly identified.

In this study, we aim to propose an alternative to the solution of the problem of oil flow and production in a multi-fractured shale oil reservoir serviced by horizontal wells by applying the concepts of the Transformational Decomposition Method (TDM) of Moridis (1995), building on the accumulated experience on the subject of discretization-free models, and attempting to overcome their limitations.

1.6 Objectives

The overall objectives of this work are:

- To extend the Transformational Decomposition Method (TDM) proposed by Moridis (1995) to the solution of three-dimensional problems of fluid flow through multi-fractured horizontal well systems in ULP reservoirs;
- To further extend the TDM by introducing advanced capabilities such as (a) time-variable production rates or bottomhole pressures, (b) fully or partially penetrating hydraulic fractures and (c) heterogeneity at the sub-domain scale;
- To develop a compact and easy-to-use FORTRAN program implementing the TDM solutions;
- To validate the TDM solutions against (a) the results from existing analytical solutions and (b) the predictions of a numerical reservoir simulator;
- To extend the concept of TDM to ULP gas systems by developing the Partial Transformational Decomposition Method (PTDM) that addresses the challenge posed

by the severe non-linearity caused by the strong pressure dependence of gas density and viscosity;

- To *develop* a compact and easy-to-use FORTRAN program implementing the PTDM solutions;
- To *validate* the TDM solutions against the predictions of a numerical reservoir simulator;
- To *demonstrate* the power, efficiency, accuracy and other advantages of the TDM and PTDM solutions in the solution of a variety of complex problems of flow and production of oil and gas, respectively;

CHAPTER II

DEVELOPMENT AND APPLICATION OF THE TRANSFORMATIONAL DECOMPOSITION METHOD (TDM) TO THE PROBLEM OF 3D FLOW OF OIL THROUGH FRACTURED MEDIA

This chapter discusses in-detail the development of a TDM-based solution to the problem of 3D oil flow through, and production from, a multi-fractured shale oil reservoir. The work is an expansion of the TDM to three-dimensional problems of oil flow through fracture and matrix complex systems after its earlier application to one- and two-dimensional problems of flow through porous media. In the subsequent sections, we present the development of the method, provide validation examples through comparisons to analytical and numerical solutions, and demonstrate application of the TDM method to complex 3D problems.

2.1 Objectives and General Description of the Transformational Decomposition Method (TDM)

The main objective of this study is to expand the concepts of the Transformational Decomposition Method (Moridis, 1995) to the solution of the 3D PDE of flow of oil in ultra-tight permeability media (such as shale oil reservoirs), thus developing fast analytical/semi-analytical solutions (and the corresponding simulators) to the problem of production, flow and pressure interference of multi-fractured systems developed between parallel horizontal wells. These solutions have the potential to provide a reliable and fast

tool to identify the dominant mechanisms and factors controlling the system behavior, to provide early estimates of expected production rates and recovery, and can act as the basis for a rapid initial parameter identification in a history-matching process, for possible further refinement using full numerical modeling (if necessary).

The TDM process involves first the selection of a primary variable that allows recasting the 3D general PDE of flow of slightly compressible liquids (such as water and oil) into a completely linearized form without loss of generality. The resulting linearized 3D PDE is then subjected to Laplace Transform (LTs) to eliminate time. The subsequent 'Decomposition Stage' involves the application of successive Finite Cosine Transforms (FCTs) to eliminate either (a) all three dimensions, yielding a simple algebraic equation or (b) two dimensions, yielding an ODE in time only. In the final 'Reconstruction Stage', the solutions of the multi-transformed space equations are inverted (in a reverse order than that followed in the Decomposition Stage) to provide solutions that are analytical in space and semi-analytical in time because the complexity of the resulting equations precludes the development of closed-form relationships of time dependence from the LT inversion of LTs, thus necessitating numerical inversion.

TDM is expected to offer some significant advantages. The elimination of the spatial and temporal discretization reduces the computer memory storage needs to a trivial level and saves time and effort required for the creation of a grid system. Because it treats the 3D space and time as a continuum, it can provide solutions only at the desired point and time

without the requirement of numerical simulators to obtain results at times and locations of no interest. The simplicity of the concept does not pose significant coding challenges and leads to the generation of a compact code that uses limited input data, is easy to implement and does not require highly specialized personnel (as do numerical simulators) for its application. This compact, very fast code can be used to conduct a large number of simulations within a limited time that can serve a number of purposes: Monte Carlo simulations, history matching, sensitivity analyses, evaluation of alternative production scenarios, etc.

2.2 TDM Approach and Implementation

2.2.1 Underlying Assumptions

The current stage of the TDM development involves some assumptions. These include single phase oil flow, indicating flow at pressures P higher than the bubble pressure P_b (aqueous and/or gas phases, if present, are assumed immobile, and the oil effective permeability is taken as the matrix permeability of the reservoir); the hydraulic fracture (HF) has a very high permeability, with flow exhibiting negligible pressure loss along and across it; the oil flow is isothermal (a valid assumption over long production periods); the flow properties may be anisotropic but homogeneous within regularly-shaped subdomains, although the domain may be heterogeneous as a whole; the size of the horizontal well is very small compared to the dimensions of the domain (a reasonable assumption); and gravitational effects are negligible (a valid assumption, given the high pressure of the system, especially in shale oil reservoirs with limited thickness). As will

become obvious in the ensuing discussion, TDM can deal with subdomain-based heterogeneity of the domain and can easily describe the behavior of partial penetration HFs (*i.e.*, HFs with a surface area that is smaller than that of the vertical surface (i.e. $Y_F \times Z_F$ at $x = 0$) for production at a constant or time-variable rate. Its current development cannot yet address the case of production at a constant or time-variable pressure with a partially-penetrating HF, as well as that of a HF with sufficiently low permeability to affect a measurable pressure drop along its length. However, work to resolve these limitations is well advanced.

2.2.2 The TDM Simulator and the Code Validation Approach

The mathematical equations describing the decomposition and reconstitution stages of the TDM were coded in a computer program written in FORTRAN 95. The code was written in a general fashion, allowing either double or quad-precision variables through the value of a single input. Compared to the double-precision, the quad-precision version that was also developed (providing 32 decimal digits of precision in the computations) required significantly longer execution times without any significant difference in the results; consequently, the quad-precision option was used rarely and mainly for testing and confirmation purposes. Note that memory requirements in TDM are minimal (if not trivial) because the nature of the solution (fully analytical in space and semi-analytical in time) does not require the large storage needed (a) for the description of the discretized domain and (b) for the coefficients of matrix equation of flow that need to be solved to provide the required solution. To maximize computational efficiency, the infinite

summations in the computations of the inverse FCTs (see **Appendix A**) were conducted in 'batches' of 100, after the end of which the convergence of the solutions was checked. Continuation of the computations ceased when the partial sums fell below a very tight criterions (10^{-8} %), thus ensuring a very accurate solution for the subsequent inversions of the LT equations.

The TDM results were compared to the results obtained from FTSim with the oil property module. FTSim is a simplified version of the TOUGH+ compositional numerical simulator (Moridis and Pruess, 2016) with the OilGasBrine V1.0 option that has been extensively validated and used in important investigations (*e.g.*, Reagan et al., 2015; 2019; Sarkar et al., 2020; Moridis and Reagan, 2020). As in TOUGH+, FTSim is a family of codes that comprises (a) a core component that is based on the Integral Finite Difference (IFD) method for space discretization, and which is common to the simulations of all the problems that can be solved by this code and (b) a case-specific component (option) that solves a particular type of problem. It provides a general-purpose simulation framework and has been used in a wide range of applications covering practically all aspects of fluids and heat flow and transport through porous and fractured media.

2.2.3 The Simulation Domain

The TDM solutions are based on a stencil, *i.e.*, the smallest repeatable symmetric element that can be identified within the domain of multi-fractured systems in reservoirs produced by parallel horizontal wells. It can accurately describe the performance and behavior of a subset of the well-HF system continuum and its use has additive properties, *i.e.*,

production from the entire system can be accurately estimated through a simple summation of the stencil-based results. The work of Olorode (2011), Olorode et al. (2013) and Freeman et al. (2013) has provided conclusive evidence of the usefulness and accuracy of stencils to predict the behavior of the entire horizontal well + HF system for very long times. Additionally, the use of stencils allows investigation of processes and phenomena occurring at very fine (mm-level) scales that may be have important effects on production, the results of which may be attenuated at the coarser scales of numerical simulator discretization that are dictated by the need to keep the size of the simulated problem to manageable levels.

Fig. 2.1 shows the domain of the simulated Cartesian stencils in our study, which is typical of a Type I fractured system (Freeman et al., 2013) and represents 1/8th of the reservoir volume drained by a single HF connected to a horizontal well. The sufficiency of such a small subset of the horizontal well + HFs system to describe the system behavior stems from (a) the significant symmetries in its geometry, *i.e.*, the vertical (y,z) planes of symmetry at $x = 0$ and $x = L_x$, the vertical (x,z) planes of symmetry at $y = 0$ and $y = L_y$ and (b) the assumption of negligible gravitational effects, which creates a horizontal (x,y) plane of symmetry at $z = 0$. The stencil is bounded by an impermeable overburden that begins at $z = L_z$. Production from a horizontal well with N_{HF} hydraulic fractures can be estimated by multiplying the results from the study of a single stencil by $8N_{HF}$ after ensuring the appropriate representation of the boundary stencils.

Note that investigation of flow through, and production from, such stencils is by no means an easy task, as accurate description that captures all important processes requires a very fine spatial discretization that results in 100,000s of elements (Freeman et al., 2013; Sarkar et al., 2020; Moridis and Reagan, 2020). The IFD grid of the stencil for the FTSim simulations (needed for comparisons to the TDM solutions) in this study involved over 356,000 cells because of the need for very fine (mm-level) spatial discretization in the vicinity of the HF.

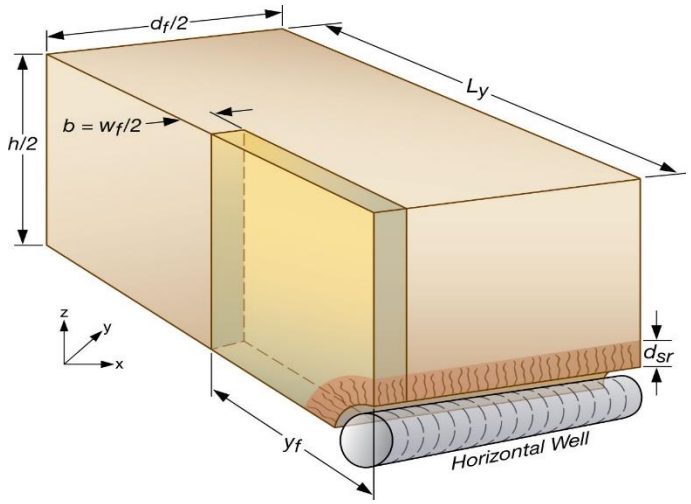

Figure 2.1 — The TDM domain: the stencil of the multi-fractured shale oil/gas reservoir used in this study (reprinted from Freeman et al., 2013).

2.2.4 Properties, Initial and Boundary Conditions

The oil and reservoir properties, as well as the initial reservoir conditions, are listed in **Table 2.1**. The paucity of the data in **Table 2.1** attests to the limited input needs (and the associated storage requirements) for the TDM solution and compares very favorably with

the input needs for the FTSim solution, for which the size of the grid-associated inputs and information exceeds 115 MB. The boundary conditions include no-flow (Neuman) boundaries at $x = L_x$, $y = 0$, $y = L_y$, $z = 0$ because of symmetry; a no flow boundary at and $z = L_z$ because the assumption of an impermeable boundary at that elevation; a no flow boundary at the $x = 0$ at any location of the vertical *(y,z)* plane outside the HF; either a prescribed-rate (constant or time-variable, Neuman type) or a prescribed-pressure (constant or time-variable, Dirichlet conditions) boundary on the surface of the HF on the vertical (*y,z*) plane at $x = 0$.

2.3 TDM Development

2.3.1 The General Equation of Flow

2.3.1.1 The Linearized Form

Following Moridis et al. (1994) and ignoring gravitational effects, the linearized general equation of flow is

$$\sum_{d^\circ \equiv x,y,z} \lambda_{d^\circ} \left(\frac{\partial^2 \delta}{\partial d^{\circ 2}} \right) = C_T \frac{\partial \delta}{\partial t}, \quad \text{where} \quad \lambda_{d^\circ} = \frac{k_{d^\circ}}{\mu c_o} \quad \text{.....(2.1)}$$

and $\delta = \delta(x,y,z,t)$ is the primary variable of Eq. 2.1, defined from the following equations.

$$R = \exp\left[c_o \left(p - p_0 \right) \right] \quad \text{and} \quad R = 1 + \delta \quad \text{.....(2.2)}$$

i.e., δ is the deviation of R from unity. This formulation of the general equation of flow imparts practically complete linearity and involves the following important equations (Moridis et al., 1994).

$$\rho = \rho_{STC}\beta_0\ R = \ \rho_0 R,\ \ p = p_0 + \frac{1}{c_o}\ln R \quad \text{..... (2.3)}$$

from which

$$\frac{\partial \rho}{\partial d^\circ} = \frac{1}{c_o R}\frac{\partial \delta}{\partial d^\circ} \quad \text{and} \quad \frac{\partial \rho}{\partial R} = \frac{1}{c_o R} \quad \text{..... (2.4)}$$

It is obvious that, in the absence of gravitational effects and at $t = 0$, $R_0 = 1$ and $\delta_0 = 0$.

The same analysis has provided the following porosity-associated equations.

$$\phi = \phi_0 \exp\left[c_m\left(p - p_0\right)\right] = \phi_0 R^{c_m/c_o} \quad \text{and} \quad \frac{\partial \phi}{\partial p} = \phi_0 c_m R^{c_m/c_o} \quad \text{..... (2.5)}$$

leading to the following estimate of $C_T\ = \phi + \left(1/c_o\right)\left(\partial\phi/\partial p\right)$.

$$C_T = \phi_0\left(1 + \frac{c_m}{c_o}\right)R^{c_m/c_o} \simeq \phi_0\left(1 + \frac{c_m}{c_o}\right) \quad \text{..... (2.6)}$$

This approximation is accurate when the matrix porosity is invariable ($c_m = 0$). It is also valid for small pressure changes, and practically for all pressures above the bubble point when $c_m/c_o \leq 0.1$.

There are two options for the boundary conditions at $x = 0$, *i.e.*, at the face of the hydraulic fracture. For Dirichlet (constant or known time-variable pressure) conditions at the hydraulic fracture, the known boundary pressure $p_{x=0}$ yields

$$\delta_{x=0} = \exp\left[c_o\left(p_{x=0} - p_0\right)\right] - 1 \quad \text{..... (2.7)}$$

Some possible options for $\delta_{x=0}$ and its relationship to the boundary pressure $p_{x=0}$ are

$$\delta_{x=0} = \begin{cases} \delta_c = \exp\left[c_o\left(p_c - p_0\right)\right] - 1 & \text{for a constant } p_{x=0} = p_c \\ \exp\left(c_o p_t t\right) - 1 & \text{for } p_{x=0} = p_0 + p_t t \\ \delta_1 U\left(t\right) - \delta_N U\left(t - t_N\right) & \text{for } p_{x=0} = p_1 U\left(t\right) - p_N U\left(t - t_N\right) \\ \quad + \sum_{j=1}^{N-1}\left(\delta_{j+1} - \delta_j\right) U\left(t - t_j\right) & \quad + \sum_{j=1}^{N-1}\left(p_{j+1} - p_j\right) U\left(t - t_j\right) \end{cases} \tag{2.8}$$

where

p_c = the constant pressure at $x = 0$, Pa

p_i = the initial pressure at $x = 0$, Pa

p_t = dp/dt, Pa/s

p_j = the step-wise constant pressure at $x = 0$ and at the j-th step, Pa

δ_c = the constant δ at $x = 0$, as computed by Eq. 2.8

δ_j = $\exp[c_o(p_j - p_0)] - 1$: the step-wise constant δ at $x = 0$

$U(t - t_j)$ = the Heavyside step function

For Neuman conditions with known constant or time variable flux $Q_{x=0}$ (associated with the production rate $q_{x=0} = A_F Q_{x=0}$, with A_F being the area of flow), the boundary at $x = 0$ is described by

$$Q_{x=0} = \left(\frac{k_x \rho}{\mu}\right)\left(\frac{\partial p}{\partial x}\right)_{x=0} = \lambda_x \rho_0 \left(\frac{\partial \delta}{\partial x}\right)_{x=0} \quad \text{..... (2.9)}$$

Obviously, Eq. 2.9 can be used to compute the unknown time-variant flux $Q_{x=0}$ (and the oil production rate $q_{x=0}$) at the $x = 0$ boundary (*i.e.*, the Dirichlet boundary at the hydraulic fracture surface) when the pressure $p_{x=0}$ is known. Some possible options for $Q_{x=0}$ are

$$Q_{x=0} = \begin{cases} Q_c & \text{time - invariant} \\ Q_i + Q't & \text{linear} \\ Q_i \exp(-bt) & \text{exponential} \\ Q_1 U(t) - Q_N U(t - t_N) & \text{step - wise constant} \\ + \sum_{j=1}^{N-1} (Q_{j+1} - Q_j) U(t - t_j) & \end{cases} \quad \text{..... (2.10)}$$

where

b = a constant, s^{-1}

Q_c = the constant flux at $x = 0$, $kg/s/m^2$

Q_i = the initial flux, $kg/s/m^2$

Q' = dQ/dt, $kg/s^2/m^2$

Q_j = the step-wise constant flux at $x = 0$ and at the j-th step, $kg/s/m^2$

$U(t-t_j)$ = the Heavyside step function

All other boundary conditions are of the Neuman type, and are defined as follows.

$$Q_{z=0} = Q_{z=L_z} = 0, \quad Q_{y=0} = Q_{y=L_y} = 0, \quad \text{and} \quad Q_{x=L_x} = 0 \quad \text{..... (2.11)}$$

2.3.2 The TDM Decomposition Stage: Successive Transforms

2.3.2.1 Step D1: The Laplace Transform of the General Equation of Flow

Taking the Laplace transform of Eq. 2.1 yields

$$\sum_{d^\circ \equiv x,y,z} \lambda_{d^\circ} \left(\frac{\partial^2 \Psi}{\partial d^{\circ 2}} \right) = C_T s \Psi \quad \text{..... (2.12)}$$

where s is the Laplace space parameter and

$$\Psi = \Psi\left(x, y, z, s\right) = \mathcal{L}\left\{\delta\right\}, \quad \text{..... (2.13)}$$

with $\mathcal{L}\{\}$ denoting the Laplace transform of the quantity within the braces.

For Dirichlet (constant or time-variable pressure) conditions at the hydraulic fracture at $x = 0$, the Laplace transform of the boundary condition yields

$$\Psi_{x=0} = \mathcal{L}\left\{\delta_{x=0}\right\} \quad \text{..... (2.14)}$$

The Laplace transforms of Eq. 2.8 provides the following options:

$$\Psi_{x=0} = \begin{cases} \dfrac{\delta_c}{s} & \text{when} \quad \delta_{x=0} = \delta_c \\ \dfrac{1}{s - c_o p_t} - \dfrac{1}{s} & \text{when} \quad \delta_{x=0} = \exp\left(c_o p_t t\right) - 1 \\ \dfrac{1}{s}\Big[\delta_1 - \delta_N e \exp\left(-s t_N\right) & \text{when} \quad \delta_{x=0} = \delta_1 U\left(t\right) - \delta_N U\left(t - t_N\right) \\ \quad + \sum_{j=1}^{N-1} \left(\delta_{j+1} - \delta_j\right) \exp\left(-s t_j\right) \Big] & \qquad + \sum_{j=1}^{N-1} \left(\delta_{j+1} - \delta_j\right) U\left(t - t_j\right) \end{cases} \quad \text{. (2.15)}$$

For Neuman (constant or time-variable flux Q) conditions, the Laplace transform of the boundary at $x = 0$ results in

$$\mathcal{Q}_{x=0} = \mathcal{L}\{Q_{x=0}\} = \lambda_x \rho_0 \left(\frac{\partial \Psi}{\partial x} \right)_{x=0} \quad \text{..... (2.16)}$$

Note that if $x = 0$ and/or $Q_{x=0}$ are constants or known functions of time, the estimation of appropriate expression for $\mathcal{Q}_{x=0}$ is almost certain. Eq. 2.16 applies to the estimation of the unknown flux when the pressure at $x = 0$ is known (Dirichlet-type boundary). The Laplace transforms of Eq. 2.10 provides the following options:

$$\mathcal{Q}_{x=0} = \begin{cases} \dfrac{Q_c}{s} & \text{time - invariant} \\ \dfrac{Q_i}{s} + \dfrac{Q'}{s^2} & \text{linear} \\ \dfrac{Q_i}{s+b} & \text{exponential} \\ \dfrac{1}{s}\left[Q_1 - Q_N \exp(-st_N) \right. & \text{step - wise constant} \\ \left. + \sum_{j=1}^{N-1} \left(Q_{j+1} - Q_j \right) \exp(-st_j) \right) & \end{cases} \quad \text{..... (2.17)}$$

All other boundary conditions are of the Neuman type and unimportant because of Eq. 2.11.

2.3.2.2 Step D2: The First Finite Cosine Transform (FCT) of the z-Coordinate

Taking the FCT of the first kind (hereafter referred to as FCT-1) of the Laplace-transformed Eq. 2.12 along the z-coordinate, and considering that $Q_{z=0} = Q_{z=L_z} = 0$, we obtain

$$\sum_{d^\circ \equiv x,y} \lambda_{d^\circ} \left(\frac{\partial^2 \Theta}{\partial d^{\circ 2}} \right) - \left(L_l + C_T s \right) \Theta = 0 \quad \text{..... (2.18)}$$

where

$$\Theta = \Theta\left(x, y, l, s\right) = \mathcal{F}_{\mathrm{c1}}\left\{\Psi\right\},\ L_l = \lambda_z \left(\frac{l\pi}{L_z} \right)^2 \quad \text{..... (2.19)}$$

l is the integer parameter of the FCT-1 space along the z-coordinate, and $\mathcal{F}_{\mathrm{c1}}\{\}$ denotes the FCT-1 of the quantity within the braces (see **Appendix A**).

The FCT-1 of the Dirichlet boundary condition at a hydraulic fracture that span the entire reservoir thickness L_z at $x = 0$ results in

$$\Theta_{x=0} = \mathcal{F}_{\mathrm{c1}}\left\{\Psi_{x=0}\right\} = \begin{cases} L_z\ \Psi_{x=0} & \text{if } l = 0 \\ 0 & \text{if } l > 0 \end{cases} \quad \text{..... (2.20)}$$

Assuming that fluid removal occurs along the entire thickness of the reservoir at $x = 0$, the FCT-1 of the Neuman boundary condition at $x = 0$ results in

$$\dot{\mathcal{Q}}_{x=0} = \mathcal{F}_{\mathrm{c1}}\left\{\mathcal{Q}_{x=0}\right\} = \lambda_{\mathrm{x}} \rho_0 \left(\frac{\partial \Theta}{\partial x} \right)_{x=0} = \begin{cases} L_z\ \mathcal{Q}_{x=0} & \text{if } l = 0 \\ 0 & \text{if } l > 0 \end{cases} \quad \text{..... (2.21)}$$

If the hydraulic fracture occurs in the interval between Z_b and Z_e of the reservoir thickness, then the FCT-1 of the Neuman boundary condition yields

$$\dot{\mathcal{Q}}_{x=0} = \mathcal{F}_{c1}\left\{\mathcal{Q}_{x=0}\right\} = \lambda_x \rho_0 \left(\frac{\partial \Theta}{\partial x}\right)_{x=0} = \begin{cases} Z_F \;\; \mathcal{Q}_{x=0} & \text{if } l = 0 \\ Z_n \;\; \mathcal{Q}_{x=0}\left[\sin Z_{ne} - \sin Z_{nb}\right] & \text{if } l > 0 \end{cases} \quad \text{..... (2.22)}$$

where $Z_F = Z_e\text{-}Z_b$, $Z_n = L_z/(l\pi)$, $Z_{ne} = Z_e/Z_n$, $Z_{nb} = Z_b/Z_n$ and $\mathcal{Q}_{x=0}$ is obtained from Eq. 2.16 or 2.17.

2.3.2.3 Step D3: The Second FCT-1 of the y-Coordinate

2.3.2.3.1 Finite boundary at $y = L_y$

Taking the FCT-1 of Eq. 2.18 along the y-axis, and considering that $Q_{y=0} = Q_{y=L_y} = 0$, we obtain

$$\lambda_x \left(\frac{\partial^2 \Phi}{\partial x^2}\right) - \left(L_n + L_l + C_T s\right)\Phi = 0 \quad \text{..... (2.23)}$$

where

$$\Phi = \Phi\left(x,n,l,s\right) = \mathcal{F}_{c1}\left\{\Theta\right\},\; L_n = \lambda_y \left(\frac{n\pi}{L_y}\right)^2 \quad \text{..... (2.24)}$$

and n is the integer parameter of the FCT-1 space along the y-coordinate.

The FCT-1 of the Dirichlet boundary condition at a hydraulic fracture that spans the entire length L_y along the y-direction at $x = 0$ results in

$$\Phi_{x=0} = \mathcal{F}_{c1}\left\{\Theta_{x=0}\right\} = \begin{cases} L_y \;\; \Theta_{x=0} & \text{if } n = 0 \\ 0 & \text{if } n > 0 \end{cases} = \begin{cases} L_y \, L_z \;\; \Psi_{x=0} & \text{if } n = 0 \text{ and } l = 0 \\ 0 & \text{if } n > 0 \text{ or } l > 0 \end{cases} \quad \text{..... (2.25)}$$

because of Eq. 2.20.

Assuming that fluid removal occurs along the entire length L_y of the reservoir along the y-direction at $x = 0$, the FCT-1 of the Neuman boundary condition at $x = 0$ results in

$$\ddot{\mathcal{Q}}_{x=0} = \mathcal{F}_{c1}\left\{\dot{\mathcal{Q}}_{x=0}\right\} = \lambda_x \rho_0 \left(\frac{\partial \Phi}{\partial x}\right)_{x=0} = \begin{cases} L_y \ \dot{\mathcal{Q}}_{x=0} & \text{if } n = 0 \\ 0 & \text{if } n > 0 \end{cases} \quad \text{..... (2.26)}$$

in which $\dot{\mathcal{Q}}_{x=0}$ is provided by Eq. 2.21 or 2.22. If the hydraulic fracture extends from Y_b to Y_e along the y-direction, the FCT-1 of the Neuman boundary condition yields

$$\ddot{\mathcal{Q}}_{x=0} = \begin{cases} Y_F \ \dot{\mathcal{Q}}_{x=0} & \text{if } n = 0 \\ Y_n \ \dot{\mathcal{Q}}_{x=0}\left[\sin Y_{ne} - \sin Y_{nb}\right] & \text{if } n > 0 \end{cases} \quad \text{..... (2.27)}$$

where $Y_F = Y_e - Y_b$, $Y_n = L_y/(n\pi)$, $Y_{ne} = Y_e/Y_n$, $Y_{nb} = Y_b/Y_n$ and $\dot{\mathcal{Q}}_{x=0}$ is obtained from Eq. 2.21 or 2.22.

Note that $Y_{nb} = 0$ always because the beginning of the HF occurs always at $y = 0 \Rightarrow Y_b = 0$, given the domain symmetry about the (x,z) plane.

2.3.2.3.2 Infinite boundary at $y = L_y$

This case represents the conditions in a stencil associated with an outermost horizontal well in a system of parallel wells. The solution to this problem can be adequately represented by the Eqs. 2.23 to 2.27 using a very large value of L_y. The use of quad precision real variables in the FORTRAN code implementing these solutions (which allows for 32 decimal places and a maximum value of $\pm 1.1897 \times 10^{4932}$) makes this approach possible.

2.3.2.4 Step D4: First Option - The ODE in x and the TD-1D Solution

After a minor manipulation, Eq. 2.23 is rendered in the form of an ODE as

$$\frac{\mathrm{d}^2\Phi}{dx^2} - \frac{1}{\lambda_x}\left(L_n + L_l + C_T s\right)\Phi = \frac{\mathrm{d}^2\Phi}{dx^2} - A\Phi = 0 \quad \text{..... (2.28)}$$

its characteristic equation is

$$\alpha^2 - A = 0 \;\Rightarrow\; \alpha_{1,2} = \pm\sqrt{A}, \quad \text{..... (2.29)}$$

and the general solution to Eq. 2.28 is

$$\Phi = \Phi\left(x, n, l, s\right) = B_1 \exp\left(\sqrt{A}\,x\right) + B_2 \exp\left(-\sqrt{A}\,x\right) \quad \text{..... (2.30)}$$

where B_1 and B_2 are parameters to be determined. Eq. 2.30 is a simple one-dimensional ODE in x in the multi-transformed (x+n+l+s) space into which the original three-dimensional, time-dependent PDE of flow has been decomposed, and is hereafter referred to as the *TD-1D* solution.

The derivative of Eq. 2.30 is

$$\frac{d\Phi}{dx} = \sqrt{A}\left[\, B_1 \exp\left(\sqrt{A}\,x\right) - B_2 \exp\left(-\sqrt{A}\,x\right)\right] \quad \text{..... (2.31)}$$

and the Neuman (no-flow) conditions at the $x = L_x$ boundary (the fracture face) necessitate that

$$B_1 \exp\left(\sqrt{A}\,x\right) - B_2 \exp\left(-\sqrt{A}\,x\right) = 0 \quad \text{..... (2.32)}$$

2.3.2.5 Dirichlet conditions (constant or time-variable $p_{x=0}$) at $x = 0$, finite no-flow boundary at $x = \pm L_x$

For an internal stencil (*i.e.*, not involving the $x = 0$ and the $x = L_x$ boundaries) with Dirichlet conditions at the local $x = 0$ boundary (the hydraulic fracture), Eq. 2.30 imposes that

$$B_1 + B_2 = \Phi_{x=0} \Rightarrow B_2 = \Phi_{x=0} - B_1 \quad \text{..... (2.33)}$$

From Eq. 2.32

$$B_1 = \frac{\Phi_{x=0} \exp\left(-\sqrt{A}\, x\right)}{\left[\exp\left(\sqrt{A}\, x\right) + \exp\left(-\sqrt{A}\, x\right)\right]}, \quad \text{..... (2.34)}$$

where $\Phi_{x=0}$ is provided by Eq. 2.25. Knowledge of B_1 and B_2 allows the estimation of Φ at any point x in the domain through the application of Eq. 2.30.

Estimation of the flux at the $x = 0$ boundary (= the oil production rate) is obtained from the application of Eqs. 2.26 and 2.31 as

$$\ddot{\mathcal{Q}}_{x=0} = \lambda_x \rho_0 \left(\frac{\partial \Phi}{\partial x}\right)_{x=0} = \lambda_x \rho_0 \sqrt{A}\left(B_1 - B_2\right) \quad \text{..... (2.35)}$$

2.3.2.6 Dirichlet conditions (constant or time-variable $p_x = 0$) at $x = 0$, infinite $x \rightarrow \pm\infty$ boundary

These conditions describe an edge stencil associated with the last horizontal fracture ($L_x \rightarrow \infty$, Right Infinite Boundary or RIB) or the first horizontal fracture ($L_x \rightarrow -\infty$, Left

Infinite Boundary or LIB). Then, Eq. 2.32 dictates that $B_1 = 0$ for ($L_x \rightarrow \infty$, and Eq. 2.33 yields $B_2 = \Phi_{x=0}$. Conversely, when $L_x \rightarrow -\infty$, $B_2 = 0$ and $B_1 = \Phi_{x=0}$.

Note that in the case of RIB, an accurate computation of production from this hydraulic fracture cannot be accommodated by simply doubling the RIB-associated estimate, but it necessitates computation and addition of the contribution of the finite semi-domain to the left of the hydrate fracture, which is estimated from the equations in this section but with the L_x related to this sub-domain (stencil) being replaced by the finite - L_x of the adjacent stencil in the Eqs. 2.33 to 2.35. The opposite occurs in the case of a LIB; the effect of the LIB is estimated using a very large negative value for L_x in the Eqs. 2.33 to 2.35, and then it is necessary to estimate (and to add to the LIB estimate of production from the hydraulic fracture) the contribution of the finite semi-domain to the right of the hydraulic fracture (obtained by using the finite L_x of the adjacent stencil in the Eqs 2.33 to 2.35).

2.3.2.7 Neuman conditions (constant or time-variable *Q*) at *x* = 0, finite no-flow boundary at *x* = $\pm L_x$

For an internal stencil and for Neuman conditions at the $x = 0$ boundary, Eqs. 2.26 and 2.31 impose that

$$\left(B_1 - B_2\right) = \frac{\ddot{Q}_{x=0}}{\lambda_x \rho_0 \sqrt{A}} = D \quad \Rightarrow \quad B_2 = B_1 - D \qquad (2.36)$$

From Eq. 2.32.

$$B_1 = \frac{D\exp\left(-\sqrt{A}\,x\right)}{\left[\exp\left(-\sqrt{A}\,x\right)-\exp\left(\sqrt{A}\,x\right)\right]} \quad \text{..... (2.37)}$$

Eq. 2.30, with the coefficients described by Eqs. 2.33, 2.34, 2.36 and 2.37, are the solution of the analytical solution of the original 3D time-variable problem of Eq. 2.1 in the multi-transformed space (x+n+l+s). It is referred to as the TD-1D solution because it is the solution of the final multi-transformed ODE in a single dimension (x).

2.3.2.8 Neuman conditions (constant or time-variable *Q*) at *x* = 0, infinite $x \to \pm\infty$ boundary

These conditions describe an edge stencil associated with the last horizontal fracture ($L_x \to \infty$,, *i.e.,* the RIB) or the first horizontal fracture ($L_x \to -\infty$, *i.e.,* the LIB). The approach to be followed is exactly analogous to that in corresponding Dirichlet conditions, and the associated discussion will not be repeated here.

2.3.2.9 Step D5: Second Option - The FCT of the x-Coordinate and the TD-0D Solution

Under Neuman conditions (constant or time-variable Q) at $x = 0$ and at the finite $x = \pm L_x$ boundary (where $Q_{x=L_x} = 0$), the FCT-1 of Eq. 2.23 along the x-axis yields

$$-\left(L_{m1} + L_n + L_l + C_T s\right)\Upsilon_1 = \lambda_x \left(\frac{\partial \Phi}{\partial x}\right)_{x=0} \quad \text{..... (2.38)}$$

where

$$\Upsilon_1 = \Upsilon_1\left(m,n,l,s\right) = \boldsymbol{\mathcal{F}}_{c1}\left\{\Phi\right\} \text{ and } L_{m1} = \lambda_x\left(\frac{m\pi}{L_x}\right)^2 \quad \text{..... (2.39)}$$

For Dirichlet conditions (constant or time-variable $p_{x=0}$) at the hydraulic fracture at $x = 0$ and for the known condition of $Q_{x=L_x} = 0$, taking the 2nd type FCT (hereafter referred to as FCT-2, see **Appendix A**) of Eq. 2.23 along the x-axis results in

$$-\left(L_{m2} + L_n + L_l + C_T s\right)\Upsilon_2 = \left(-1\right)^m \lambda_x\left(\frac{\left(2m-1\right)\pi}{2L_x}\right)\Phi_{x=0}, \quad \text{..... (2.40)}$$

where

$$\Upsilon_2 = \Upsilon_2\left(m,n,l,s\right) = \boldsymbol{\mathcal{F}}_{c2}\left\{\Phi\right\}, L_{m2} = \lambda_x\left(\frac{\left(2m-1\right)\pi}{2L_x}\right)^2, \quad \text{..... (2.41)}$$

$\Phi_{x=0}$ is provided by Eq. 2.25 and $\boldsymbol{\mathcal{F}}_{c2}\{\}$ denotes the FCT-2 of the quantity within the brackets.

For a time-variable pressure at the $x = 0$ boundary, the treatment is somewhat more complicated. In that case, application of the FCT-2 requires that $\delta_{x=0}$ be unconditionally a constant at all times. This necessitates replacement of the primary variable by $\delta_D = \delta - \delta_{x=0}$ in Eq. 2.1. The time dependence of $\delta_{x=0}$ is resolved during the Laplace transform stage, which eliminates time from consideration in all subsequent steps. Additionally, the consistent value of $\delta_D = 0$ at $x = 0$ relieves the need to deal with its FCT transforms there. Because the TDM process in this case is straightforward and analogous to the process followed in all other cases, it will not be further described here.

2.3.2.10 General form of the zero-dimension TD-0D solution in the multi-transformed space

Eq. 2.38 or 2.40 lead to

$$\Upsilon_i = \frac{E_i}{\left(L_{mi} + L_n + L_l + C_T s\right)},\ i = 1, 2 \quad \text{..... (2.42)}$$

where

$$E_1 = \begin{cases} \dfrac{L_y\ L_z\ \mathcal{Q}_{x=0}}{\rho_0} & \text{if } n = 0 \text{ and } l = 0 \\ 0 & \text{if } n > 0 \text{ or } l > 0 \end{cases} \quad \text{..... (2.43)}$$

and

$$E_2 = \begin{cases} (-1)^{m+1} L_y\ L_z\ \lambda_x \dfrac{(2m-1)\pi}{2L_x} \Psi_{x=0} & \text{if } n = 0 \text{ and } l = 0 \\ 0 & \text{if } n > 0 \text{ or } l > 0 \end{cases} \quad \text{..... (2.44)}$$

Eq. 2.42 is a simple algebraic equation in the multi-transformed (m+n+l+s) space into which the original three-dimensional, time-dependent PDE of flow has been decomposed. As the solution of Eq. 2.42 no longer involves spatial dimensions, it is hereafter referred to as the *TD-0D* solution.

Because of the conditions in the domain of the stencil of the shale oil problem, this approach is applicable only to problems involving Neuman-type boundary conditions (*i.e.*, involving known fluxes) at both the $x = 0$ and $x = L_x$ boundaries, and cannot be applied to problems involving a known time-variable pressure at the hydraulic fracture face. Thus,

this approach has a much narrower applicability than the one involving the solution of the ODE described in Step D4.

2.3.3 The TDM Reconstruction Stage: Successive Inverse Transforms

The reconstruction stage includes successive inverse transforms: two or three inverse FCT transforms (depending on whether the decomposition process was terminated that the TD-1D or TD-0D solutions, respectively), and an inverse Laplace transform. At the end of the reconstruction process, the collapsed TDM solution in the multi-transformed space yields solutions at any point in space and time.

2.3.3.1 Step R1: Inversion of the TD-0D Equation and Retrieval of the Solution Along the x-Axis

If the solution involves the FCT of the x-coordinate (*i.e.*, if the decomposition process reaches the stage of the collapsed TD-0D equation), the first step in the process to obtain a solution in the (x+y+z+t) space involves the application of the inverse FCT of the solution Υ_i (Eq. 2.42) to obtain the solution at any point x in the multi-transformed space (x+n+l+s), leading to

$$\Phi = \Phi\left(x,n,l,s\right) = \mathcal{F}_{c1}^{-1}\left\{\Upsilon_1\right\} = \frac{1}{L_x}\left[\Upsilon_1\left(0,n,l,s\right) + 2\sum_{m=1}^{\infty}\Upsilon_1\left(m,n,l,s\right)\cos\left(\frac{m\pi x}{L_x}\right)\right] \quad \text{..... (2.45)}$$

or

$$\Phi = \Phi\left(x,n,l,s\right) = \mathcal{F}_{c2}^{-1}\left\{\Upsilon_2\right\} = \frac{2}{L_x}\left[\sum_{m=1}^{\infty}\Upsilon_2\left(m,n,l,s\right)\cos\left(\frac{\left(2m-1\right)\pi x}{2L_x}\right)\right] \quad \text{..... (2.46)}$$

where $\mathcal{F}_{ci}^{-1}\{\}$ $\{i=1,2\}$ denotes the inverse FCT-i of the quantity within the brackets.

2.3.3.2 Step R2: Inversion of the TD-1D Equation and Retrieval of the Solution Along the y-Axis

The next step involves the restoration of the y-coordinate by applying the inverse FCT-1 to Φ from Step R1 according to

$$\Theta = \Theta(x,y,l,s) = \mathcal{F}_{c1}^{-1}\{\Phi\} = \frac{1}{L_y}\left[\Phi(x,0,l,s) + 2\sum_{n=1}^{\infty}\Phi(x,n,l,s)\cos\left(\frac{n\pi y}{L_y}\right)\right] \text{ ..... (2.47)}$$

This inversion provides a solution at any point (x,y) in the transformed space (x+y+l+s).

2.3.3.3 Step R3: Inversion of the FCT Transform and Retrieval of the Solution Along the z-Axis

The final step in the multi-stage inversion process involves the application of the inverse FCT to the Θ solution from Step R2 in order to restore the z-coordinate, thus providing the Laplace-space solution at any point in the (x+y+z+s) domain according to

$$\Psi = \Psi(x,y,z,s) = \mathcal{F}_{c1}^{-1}\{\Theta\} = \frac{1}{L_z}\left[\Theta(x,y,0,s) + 2\sum_{l=1}^{\infty}\Theta(x,y,l,s)\cos\left(\frac{l\pi z}{L_z}\right)\right] \text{ ..... (2.48)}$$

2.3.3.4 Step R4: Inversion of the Laplace Space Solution

Because of the complexity of the Laplace-space equation provided by the inverse FCT-1 in Eq. 2.48, it is not possible to invert it analytically to obtain a closed form of the time-dependent equation of three-dimensional flow. Thus, inversion of any Laplace space

solution $\Psi(x,y,z,s)$ from Step R3 is accomplished through a numerical process according to the general relationship

$$\delta = \delta(x,y,z,t) = \mathcal{L}^{-1}\{\Psi(x,y,z,s)\} \quad \text{.....(2.49)}$$

where $\mathcal{L}^{-1}\{\}$ denotes the inverse Laplace transform of the quantity within the brackets. The pressure $p = p(x,y,z,t)$ at any point in space and time is then obtained from the p vs δ relationship in Eq. 2.3.

The numerical inversion of the LT-space solutions can be accomplished by any robust numerical method of the several available in the literature. In this study, we use two methods. on one of the following two methods (or any other robust numerical inversion method). The first is the Stehfest algorithm (Stehfest, 1970a;b) (hereafter referred to as StA), a simple and computationally efficient method, This algorithm has been shown to be powerful and applicable to most LT inversion equations, but may exhibit limitations in the accuracy of the inversion of particularly steep or complex functions (Moridis et al., 1999) because of limitations associated with the real nature of the Laplace-space parameter *s* used in the computations (as opposed to the advantages of a complex *s*).

The other alternative is the very robust inversion method of DeHoog et al. (1982), hereafter referred to as the DHM. This method has been shown to provide very accurate solutions in the inversion even of complex functions with steep fronts (such as step functions), and to be accurate in the description of the challenging problem of transport of both parent radionuclides and all their daughters (Moridis et al., 1999). More information

on the StA and DHM inversion options, as well as on the sensitivity of the TDM solutions to the StA and DHM parameters, can be found in **Appendix C**.

2.4 TDM Validation and Application

To validate TDM and gain confidence in its abilities and power, we compared its predictions in a wide range of problems of results from analytical solutions (where available) and from FTSim simulations involving a grid comprising 356,000 elements. In the following sections, we present the analytical, FTSim and TDM (TD-1D and TD-0D) solutions to the following types of problems; (a) prescribed (constant and time-variable) production rate q in a stencil with a fully-penetrating HF, (b) prescribed (constant and time-variable bottomhole) pressure p_{wf} at a fully-penetrating HF, (c) production under constant q and p_{wf} regimes in a heterogeneous system with an SRV in a stencil with a fully penetrating fracture, and (d) constant production rate from a partially-penetrating fracture. We compared the evolution of (a) the pressure distributions at particular locations in the domain (pressure along x-direction for fully-penetrating HF and pressure on the horizontal (x,y) plane at $z = 0$ for partially-penetrating HF), and (b) the production rates for q for prescribed p_{wf}, or (c) the flowing pressures at the HF when producing for prescribed q. Additionally, we compared the TDM results from the two different numerical methods of LT inversion in order to evaluate their relative performance and strengths. Note that production results presented here correspond to a system involving 50 HFs, *i.e.*, 50 x 8 = 400 stencils (see **Table 2.1**). The input to the study is shown as follows.

Table 2.1 — Inputs in the TDM and the FTSim simulations.

Parameter	Value
Initial pressure P_i	2.5×10^7 Pa ≈ 3,626 psi
Fracture pressure p_{wf}	6.894757×10^6 Pa ≈ 1,000 psi
Production rate q_c	0.0003 kg/s ≈ 90 bopd from 400 stencils
Temperature T	30°C = 303.15 K
Matrix reference porosity ϕ_0	0.3
Matrix compressibility c_m	1×10^{-9} Pa^{-1}
Oil compressibility c_o	2.5×10^{-9} Pa^{-1}
Oil density ρ_o	750 kg/m^3
Oil viscosity μ_o	2.96×10^{-4} Pa-s
Matrix permeability (undisturbed) $k_x = k_y = k_z$	1.5×10^{-19} ≈ 0.15 μD
Matrix permeability (SRV) $k_x = k_y = k_z$	1.5×10^{-18} ≈ 1.50 μD
Stencil length (Half of fracture interval) L_x	10 m
Stencil depth L_y	60 m
Stencil height L_z	5 m
Fracture Dimensions (Y_F, Z_F)	
Fully-penetrating fracture (Case 1, 2, 3, 4, 5, 7, and 8)	
Half of fracture length Y_F	60 m
Half of fracture height Z_F	5 m
Fracture Dimensions (Y_F, Z_F)	
Partially-penetrating fracture (Case 6)	
Half of fracture length Y_F	40 m
Half of fracture height Z_F	3 m
Specifications of Laplace Inversion Methods	
Number of terms (N_s) for the Stehfest algorithm	8 (all cases)
Number of terms (M_H) for the DeHoog Method	10 (all cases except Case 8) 14 (Case 8)

2.4.1 Validation Cases

2.4.1.1 Case 1: Constant Production Rate q at $x = 0$ (Neuman Boundary)

Fig. 2.2 presents the evolution of the pressure distribution along the x-direction at $z = 0$ and $y = 0$ in response to production at a constant rate q (a Neuman-type boundary, see **Table 2.1**). This figure shows that the TDM results from both the TD-1D and the TD-0D solutions practically coincide with the numerical results from the FTSim simulations (considered as the reference solution). There are two additional sets of results that are not included in this figure because they are identical to those obtained from the TDM solutions; results from an analytical solution (AS) to this problem, as well as from a TD-1D study in which the domain was subdivided by a vertical (y,z) at $x = 5$ m in two separate, equally sized subdomains with identical properties (the HS solutions). The latter study was conducted in order to test and evaluate the validity of the TD-1D solution for heterogeneous systems (see **Appendix B**).

The TDM results in **Fig. 2.2** were obtained using the StA for the numerical inversion of the LTs in the R4 stage of reconstruction (which yields the solution in time), and they are identical with those in **Fig. 2.3** that were obtained using the DHM. The evolution of the StA-based solutions of the flowing pressure p_{wf} over time in **Fig. 2.4** shows the coincidence of the TD-1D and (the FTSim solutions, and the AS and HS results mentioned earlier are not included because they differ only in the 3rd decimal place and beyond. For both the StA and the DHM inversions, the average deviation between the FTSim and both

the TD-0D and TD-1D results was 0.11%. **Figs. 2.2** and **2.3** provide evidence of the validity and accuracy of the TDM solutions.

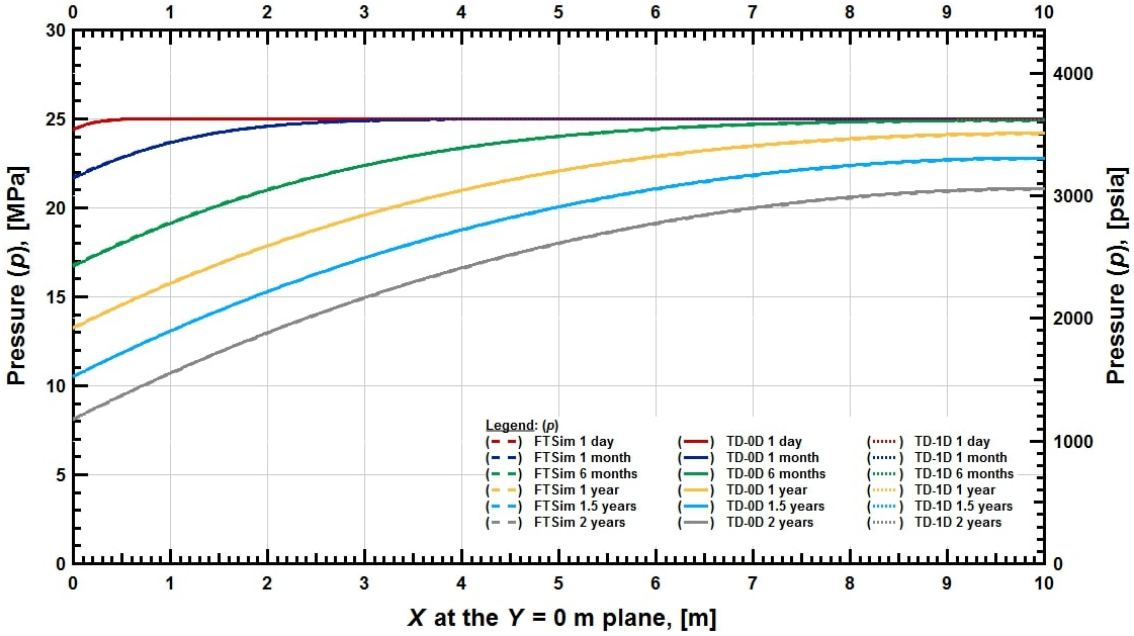

Figure 2.2 — Case 1: Evolution of pressure distribution over time in the x-direction at $z = 0$ and $y = 0$ for constant-rate production: comparison of the TD-1D and TD-0D solutions with the Stehfest (1970a;b) algorithm ($N_s = 8$) for the LT numerical inversions. The FTSim numerical solution is included for reference.

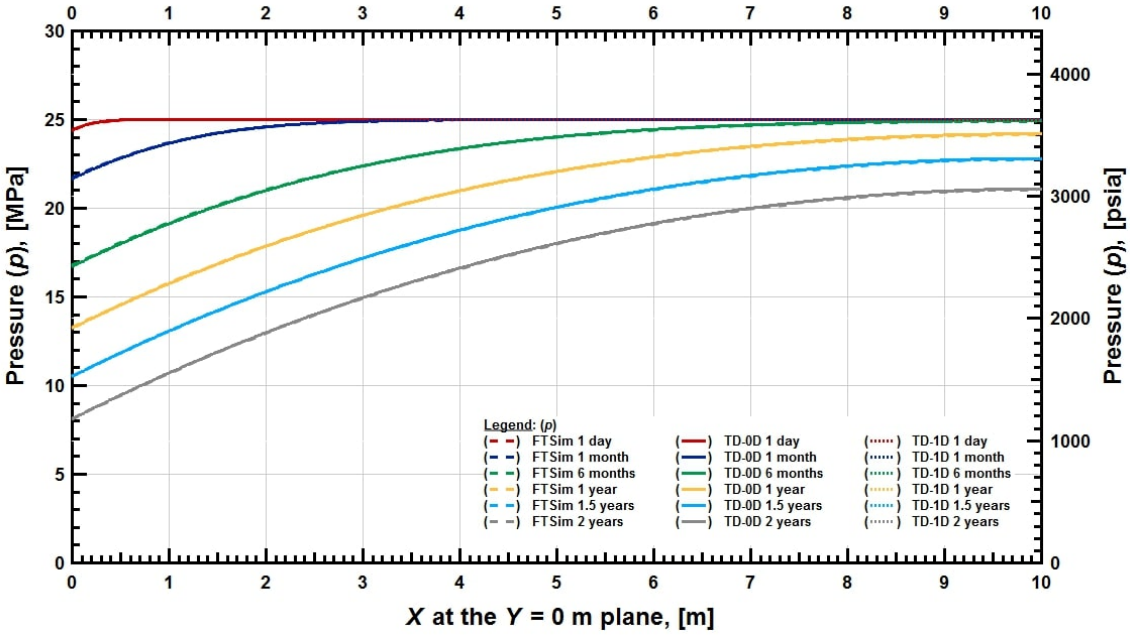

Figure 2.3 — Case 1: Evolution of pressure distribution over time in the x-direction at $z = 0$ and $y = 0$ for constant-rate production: comparison of the FTSim to the TD-1D and TD-0D solutions with the DeHoog et al. (1982) method ($M_H = 10$) for the LT numerical inversions. The results are identical to those in **Fig. 2.2**.

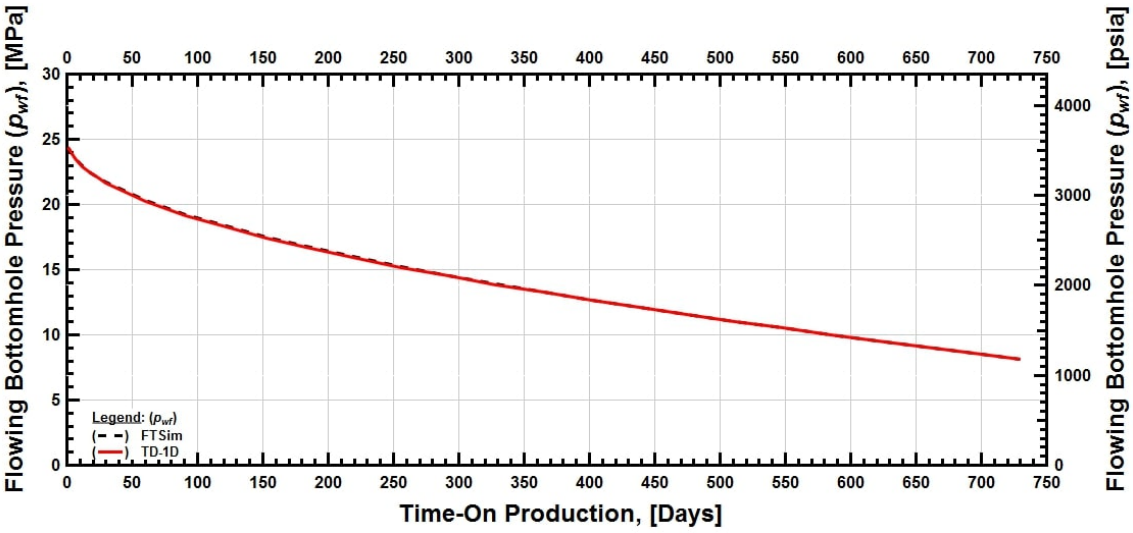

Figure 2.4 — Case 1: Evolution of the flowing bottomhole pressure p_{wf} over time at x = 0 for constant-rate production: comparison of the FTSim and the TD-1D solution with the StA (N_s = 8) inversion of the LT-space solution.

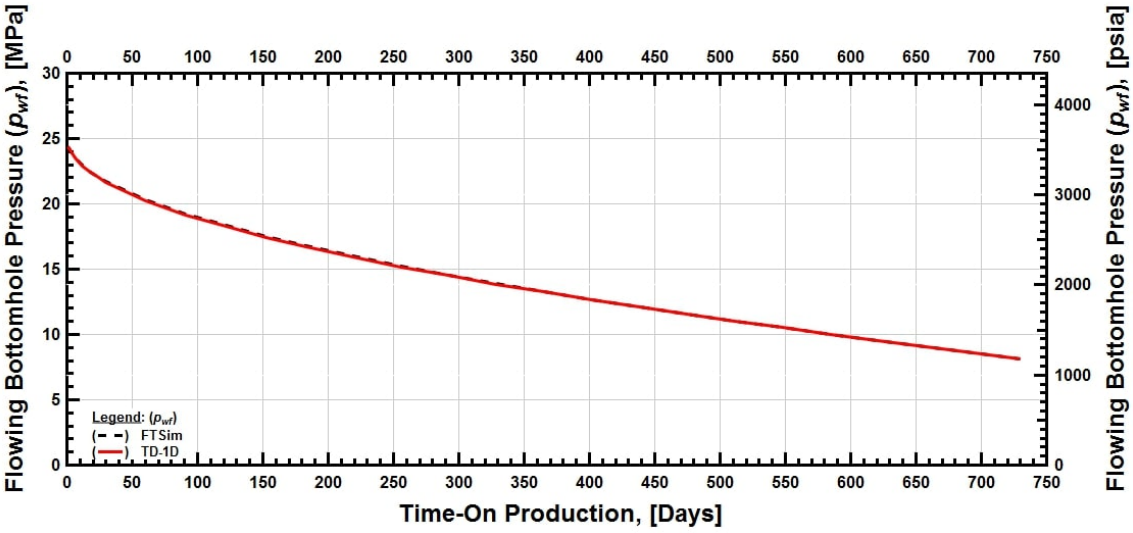

Figure 2.5 — Case 1: Evolution of the flowing bottomhole pressure p_{wf} over time at x = 0 for constant-rate production: comparison of the FTSim and the TD-1D solution with the DHM (M_H = 10) inversion of the LT-space solution. The results are identical to those in **Fig. 2.4**.

2.4.1.2 Case 2: Constant Bottomhole Pressure p_{wf} at $x = 0$ (Dirichlet Boundary)

Figs. 2.6 and **2.7** correspond to results obtained with the StA- and DHM-based inversions of the LT space solutions, respectively, and show the evolution of the pressure distribution along the x-direction at $z = 0$ and $y = 0$ in response to production at a constant bottomhole pressure p_{wf} at $x = 0$ (a Dirichlet-type boundary, see **Table 2.1**). As in Case 1, the TD-1D, TD-0D and the FTSim solutions coincide, and also coincide with AS results and the HS solutions (not shown in the figure). **Figs. 2.8** and **2.9** correspond to results obtained with the StA- and DHM-based inversions of the LT space solutions, respectively, and show the time-variable production rate q determined from the TD-1D and FTSim solutions in response to the pressure p_{wf} at the hydraulic fracture. The coincidence of these solutions confirms the validity and accuracy of the TDM. The results in **Figs. 2.6** and **2.8** are identical to those on **Figs. 2.7** and **2.9**, indicating no obvious advantage of the much more complex DHM inversion method of the LT space solution over the mush simpler StA. Finally, identical results were obtained when the solutions discussed above were obtained using the TD-1D approach when the stencil domain subdivided in two equally-sized segments. In Case 2, for both the StA and the DHM inversions, the average deviation between the FTSim and the TD-0D results was 0.53%, and between FTSim and the TD-1D results was 0.22%.

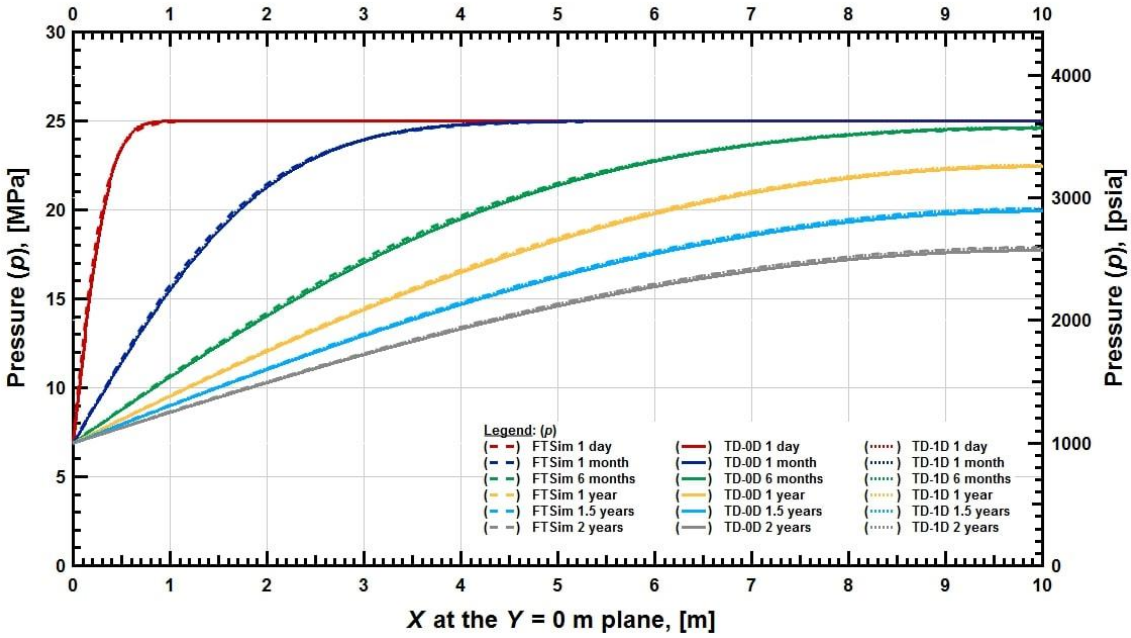

Figure 2.6 — Case 2: Evolution of pressure distribution over time in the x-direction at $z = 0$ and $y = 0$ for constant-pressure production: comparison of the FTSim to the TD-1D and TD-0D solutions obtained with the StA inversion ($N_s = 8$).

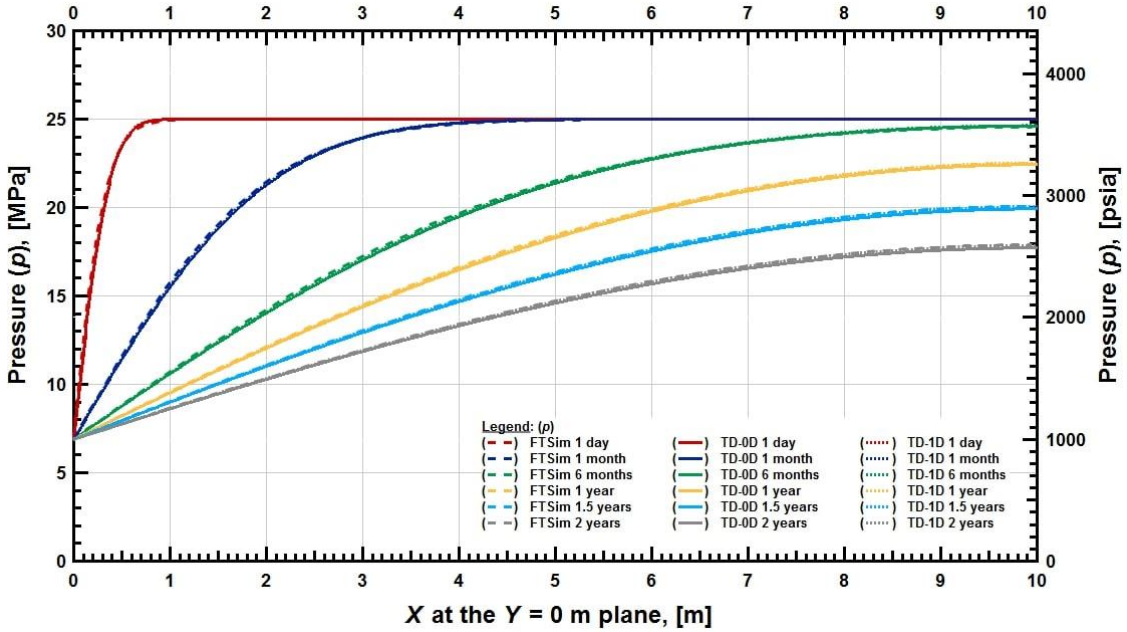

Figure 2.7 — Case 2: Evolution of pressure distribution over time in the x-direction at $z = 0$ and $y = 0$ for constant-pressure production: comparison of the FTSim to the TD-1D and TD-0D solutions obtained with the DHM inversion ($M_H = 10$).

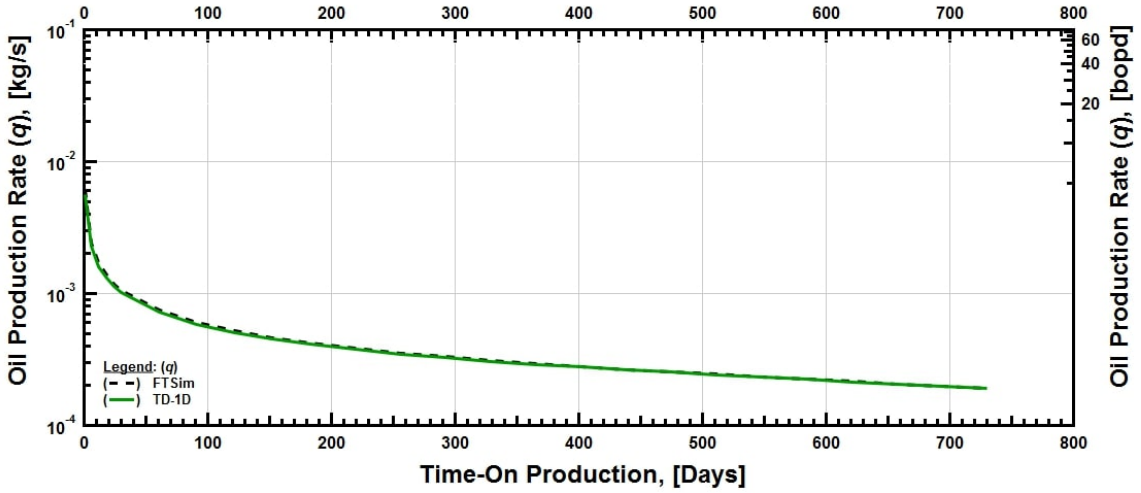

Figure 2.8 — Case 2: Evolution of the production rate q over time at the HF at $x = 0$ for constant-pressure production: comparison of the FTSim to the TD-1D solution obtained with the StA inversion ($N_s = 8$).

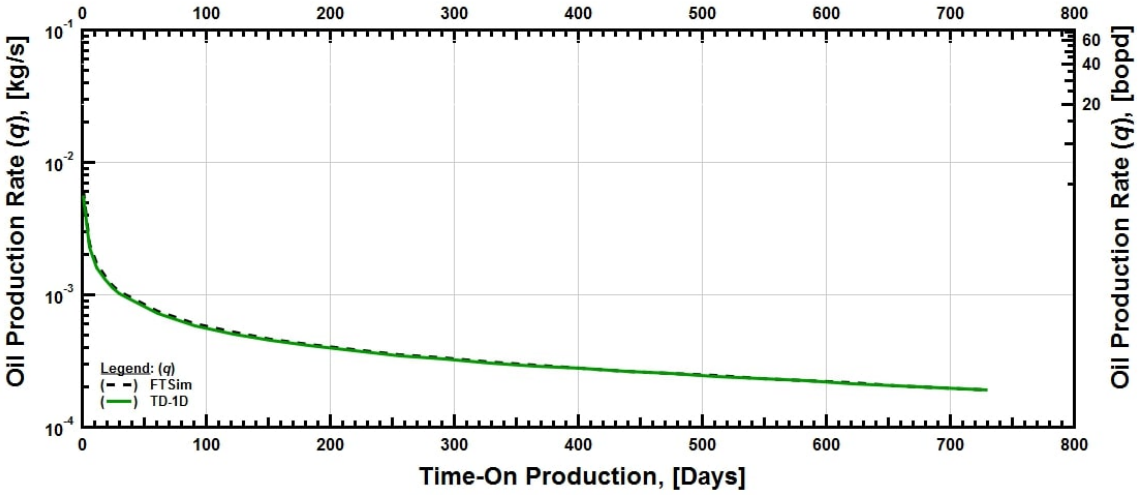

Figure 2.9 — Case 2: Evolution of the production rate q over time at the HF at $x = 0$ for constant-pressure production: comparison of the FTSim to the TD-1D solution obtained with the DHM inversion ($M_H = 10$). The results are identical to those in **Fig. 2.8**.

2.4.2 Additional Application Cases

2.4.2.1 Case 3: Linearly-Declining Production Rate q at $x = 0$ (Neuman Boundary)

This case is entirely analogous to that in Case 1, from which it differs in that the production rate $q_{x=0}$ is time-dependent, declining linearly from the original level of 3×10^{-4} (= 90 BOPD) to 2×10^{-4} (= 60 BOPD) over the 2-year production period. The results in **Figs. 2.10** and **2.11** show the evolution over time of the pressure distribution, and **Figs. 2.12** and **2.13** show the time-dependent flowing bottomhole pressure, all at the same locations as those discussed in Case 1. **Figs. 2.10** to **2.13** do not include FTSim results because the declining boundary rate can produce results of accuracy comparable to that obtained by the TD-1D and TD-0D solutions only by significantly reducing the timestep size (to avoid obtaining 'jagged' curves) and, consequently, significantly increasing the already very long execution times for the solution of the equations of flow for the 356,000-element numerical grid.

As expected, p_{wf} in Case 3 begins to diverge relatively early from, and exceeds consistently, that for Case 1. Their divergence increases as time advances because of the declining $q_{x=0}$ (**Fig. 2.12**). Additionally, the TDM solutions in **Figs. 2.10** and **2.12**, which were obtained using the StA approach for the LT inversion, coincide (a) with the analytical solution that is available for this problem, (b) with the TD-1D solution from a subdivided stencil domain, and (c) with the DHM-based solutions (**Figs. 2.11** and **2.13**) of the same variables. The results in Case 3 provide further evidence of the power, accuracy and

reliability of the TDM in the analysis of flow though, and production from, multi-fracture shale reservoirs serviced by horizontal wells.

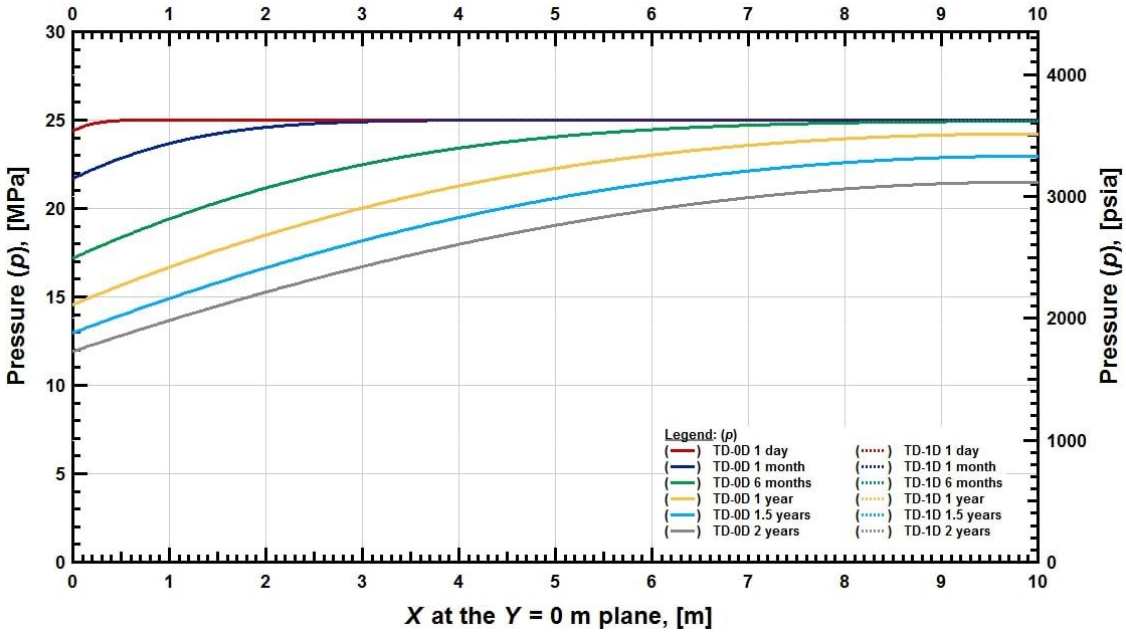

Figure 2.10— Case 3: Evolution of pressure distribution over time in the x-direction at $z = 0$ and $y = 0$ for a linearly declining production rate: comparison of the TD-1D and TD-0D solutions obtained with the StA inversion (N_s = 8).

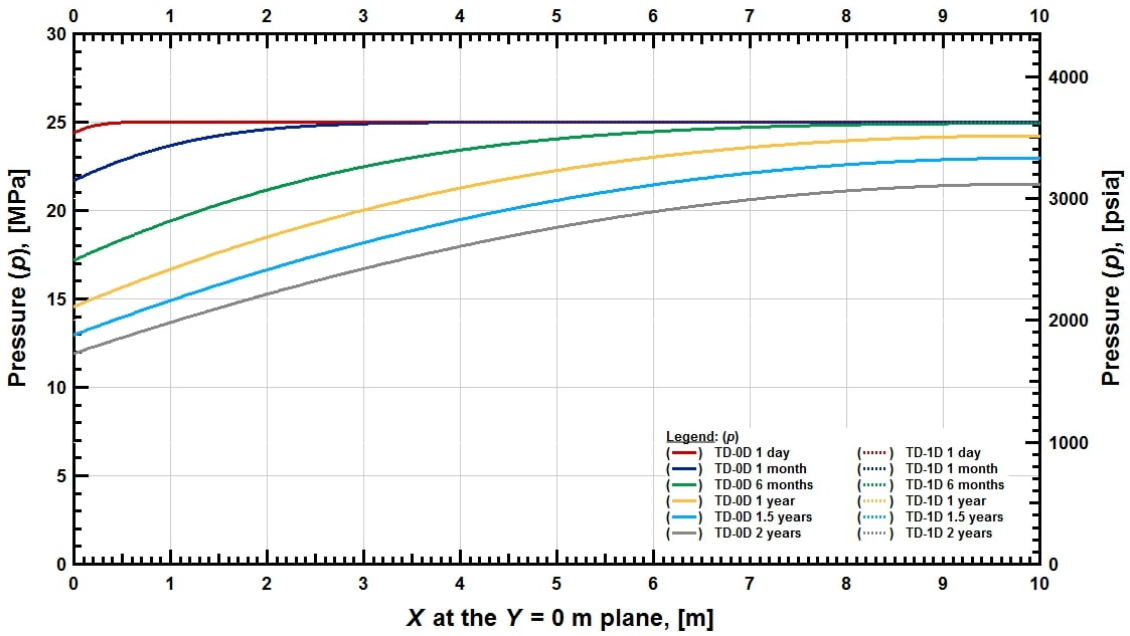

Figure 2.11— Case 3: Evolution of pressure distribution over time in the x-direction at $z = 0$ and $y = 0$ for a linearly declining production rate: comparison of the TD-1D and TD-0D solutions obtained with the DHM inversion ($M_H = 10$).

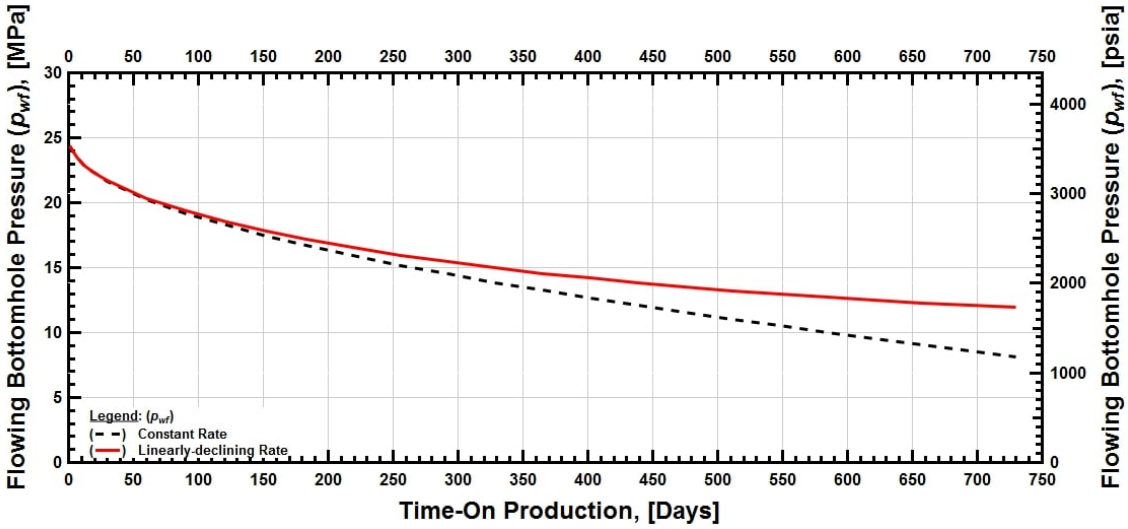

Figure 2.12— Case 3: Evolution of the flowing bottomhole pressure p_{wf} over time at x = 0 for a linearly declining production rate, obtained using the TD-1D method with the StA inversion (N_s = 8). The analogous results from Case 1 are included for comparison.

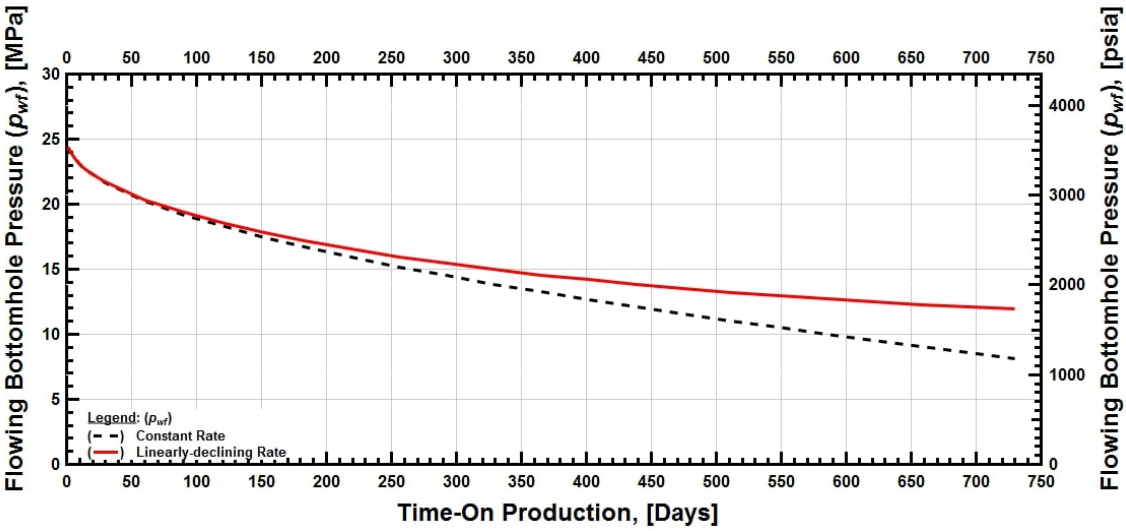

Figure 2.13 — Case 3: Evolution of the flowing bottomhole pressure p_{wf} over time at x = 0 for a linearly declining production rate, obtained using the TD-1D method with the DHM inversion (M_H = 10). The analogous results from Case 1 are included for comparison.

2.4.2.2 Case 4: Linearly-Declining Bottomhole Pressure p_{wf} at $x = 0$ (Dirichlet Boundary)

This case is entirely analogous to that in Case 2, from which it differs in that the bottomhole pressure p_{wf} is time-dependent, declining linearly from the original level of 1,000 psi to 500 psi over the 2-year production period. The results in **Figs. 2.14** and **2.15** show the evolution over time of the pressure distribution, and **Figs. 2.16** and **2.17** show the time-variable production rate, all at the same locations as those discussed in Case 2. Note that a TD-0D solution is not possible because the formulation of the FCT of the 2nd kind requires a constant boundary pressure; TD-1D has no such limitations. For the reason explained in Case 3, **Figs. 2.14** to **2.17** do not include FTSim results.

As expected, the production rate q in Case 4 is consistently higher than that in Case 2 (from which it begins to diverge early) because of the declining bottomhole pressure, which increases the pressure gradient at the HF. The TDM solution in **Figs. 2.14** and **2.16**, which were obtained using the StA approach for the LT inversion, coincide (a) with the TD-1D solution from a subdivided stencil domain, and (b) with the DHM-based solutions (**Figs. 2.15** and **2.17**) of the same variables. The results in Case 4 show the power and flexibility of the TDM in the study of production from shale oil reservoirs.

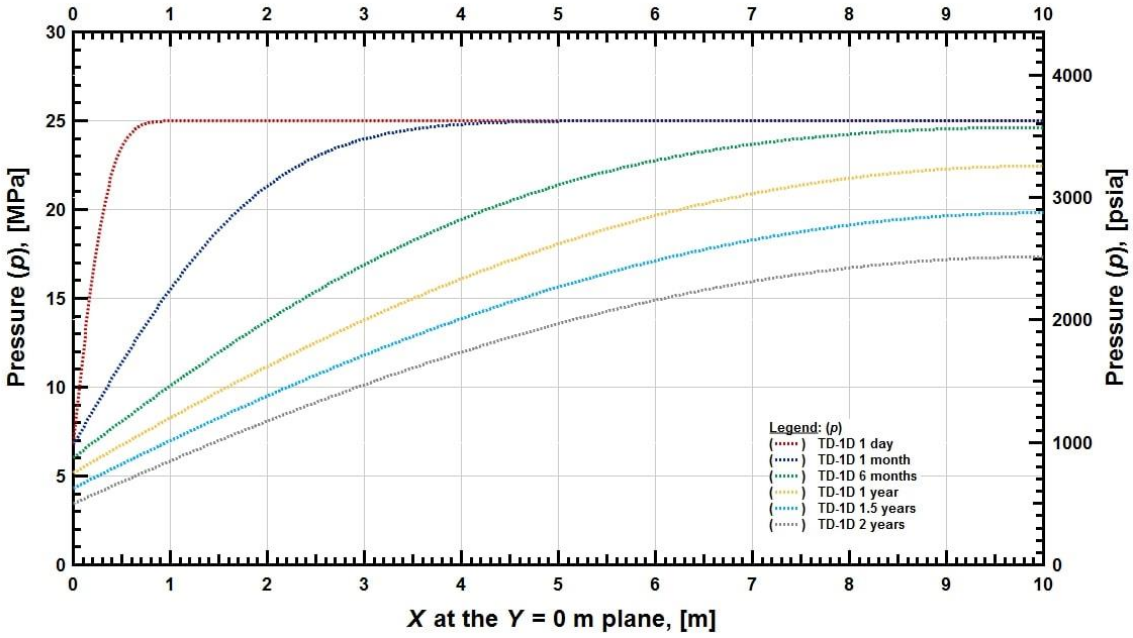

Figure 2.14— Case 4: Evolution of pressure distribution over time in the x-direction at $z = 0$ and $y = 0$ for a linearly declining bottomhole pressure p_{wf}. The TD-1D results were obtained using the StA inversion ($N_s = 8$) of the LT-space solutions

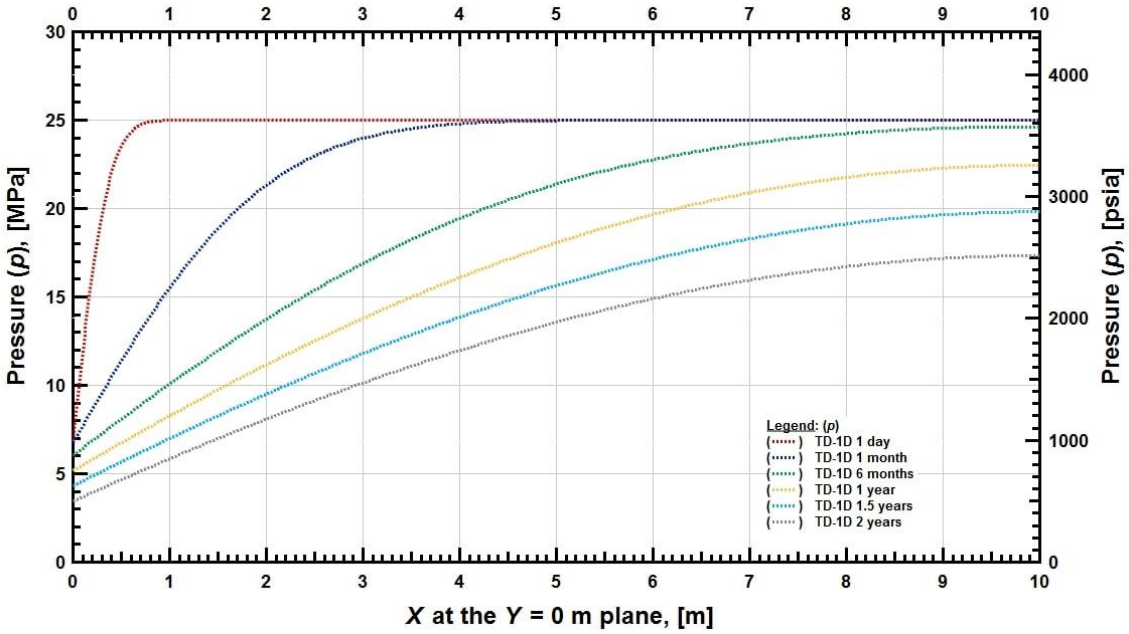

Figure 2.15— Case 4: Evolution of pressure distribution over time in the x-direction at $z = 0$ and $y = 0$ for a linearly declining bottomhole pressure p_{wf}. The TD-1D results were obtained using the DHM inversion ($M_H = 10$) of the LT-space solutions.

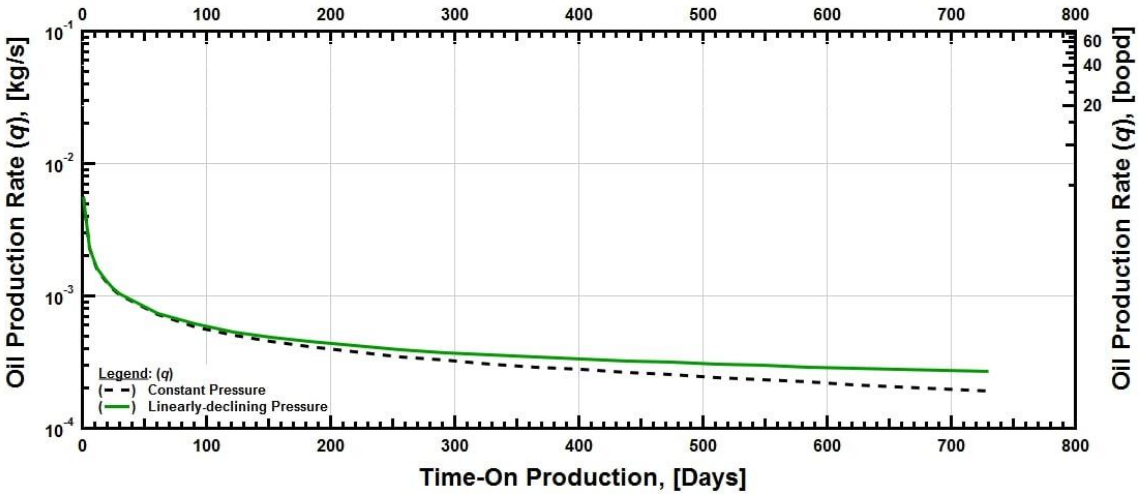

Figure 2.16— Case 4: Evolution of the production rate q over time at the HF at $x = 0$ for a linearly declining bottomhole pressure pwf obtained using the TD-1D method with the StA inversion ($N_s = 8$). The analogous results from Case 2 are included for comparison.

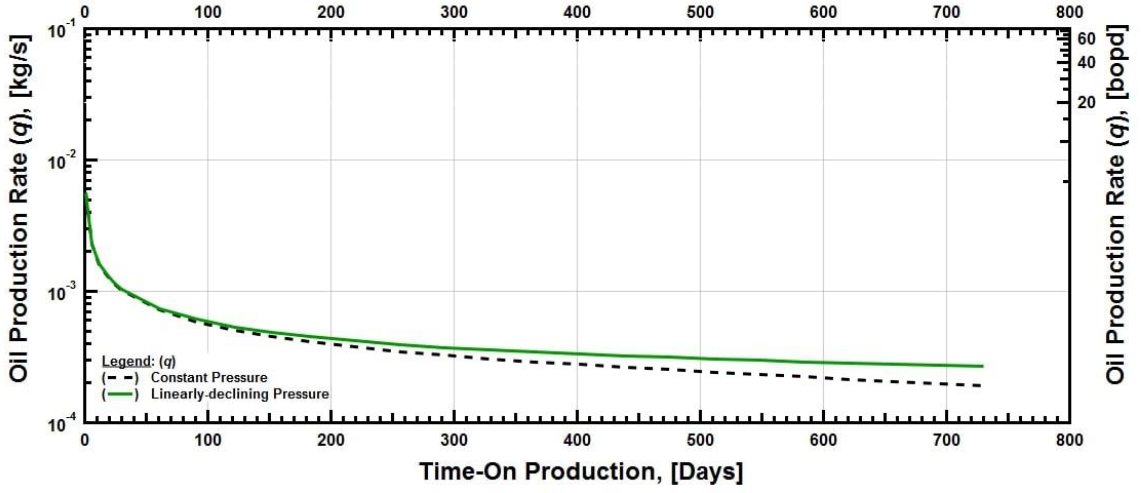

Figure 2.17— Case 4: Evolution of the production rate q over time at the HF at $x = 0$ for a linearly-declining bottomhole pressure p_{wf} obtained using the TD-1D method with the DHM inversion ($M_H = 10$). The analogous results from Case 2 are included for comparison.

2.4.2.3 Case 5: Constant Bottomhole Pressure p_{wf} at $x = 0$, heterogeneous domain with SRV (Dirichlet Boundary)

This case is entirely analogous to that in Case 2, from which it differs in that the domain is no longer homogeneous but involves 2 subdomains with different properties; a Stimulated Reservoir Volume (SRV) subdomain from $x = 0$ to $x = 5$ m, and the undisturbed matrix from $x = 5$ m to $x = L_x = 10$ m. The properties of the two subdomains are listed in **Table 2.1**. The FTSim and the TD-1D results in **Fig. 2.18** show the evolution over time of the pressure distribution at the same locations discussed in Case 2. The boundary between the two subdomains is clearly identified by the sharp change in the slope of p at this location. The agreement between the numerical and the TDM solutions is excellent. The small deviations exhibited early are caused by the discrete-volume nature of the space discretization in FTSim; although it is possible to obtain a very accurate solution, this would require very fine discretization near the SRV boundary and would greatly increase the size of the grid beyond the already very high number of 356,000. Thus, the TDM provides inherently more accurate solutions in the vicinity of interfaces of heterogeneous subdomains with different properties. Note that a TD-0D solution is not possible because it cannot handle this type of heterogeneity.

Fig. 2.19 shows the evolution over time of the time-variable production rate. Again, there is an excellent agreement of the FTSim and the TD-1D predictions. The small deviations occur when the pressure front reaches the boundary early in the production period and are caused by the imperfect FTSim discretization at this location. The TDM solution in **Figs.**

2.18 and **2.19**, which were obtained using the StA approach for the inversion of the LT-space solutions, coincide with the DHM-based solutions of the same variables. For both the StA and the DHM inversions, the average deviation between the FTSim and the TD-1D results was 0.57%. The power and flexibility of the TDM, and its superiority over the numerical solution in this case, are evident from the results. As in all the cases discussed thus far, the significant complexity of applying the DHM inversion cannot be justified by any superiority in the predictions, which coincide with those from the much simpler StA approach.

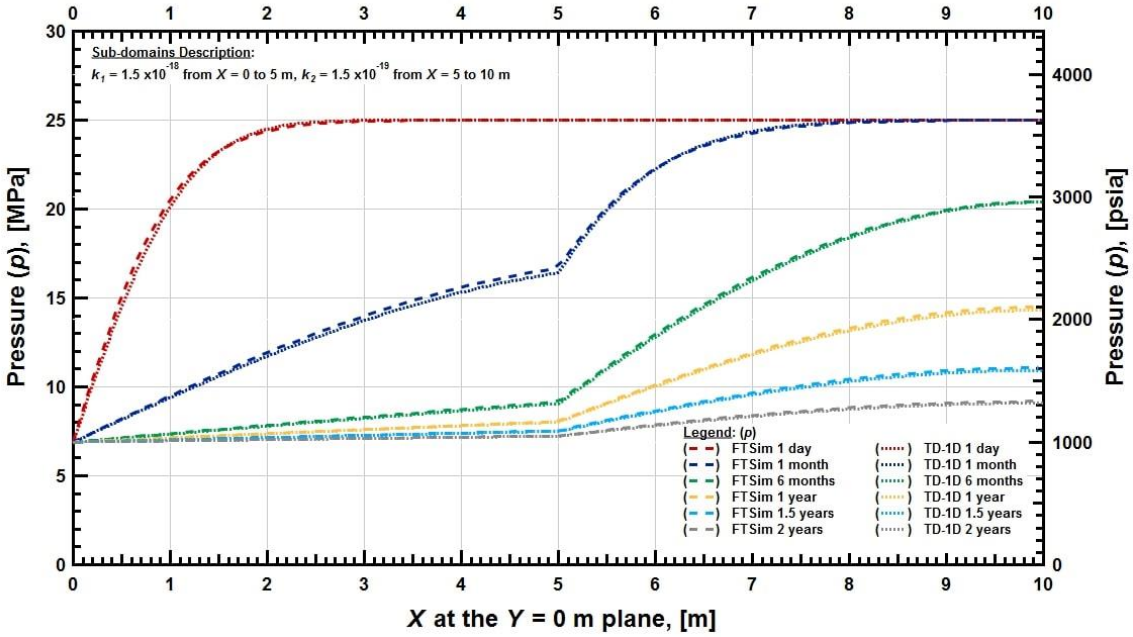

Figure 2.18— Case 5: Evolution of pressure distribution over time in the x-direction at $z = 0$ and $y = 0$ for a constant bottomhole pressure p_{wf} in a stencil with an SRV subdomain. The TD-1D predictions are based on a StA inversion ($N_s = 8$) and coincide with the corresponding DHM-based solutions.

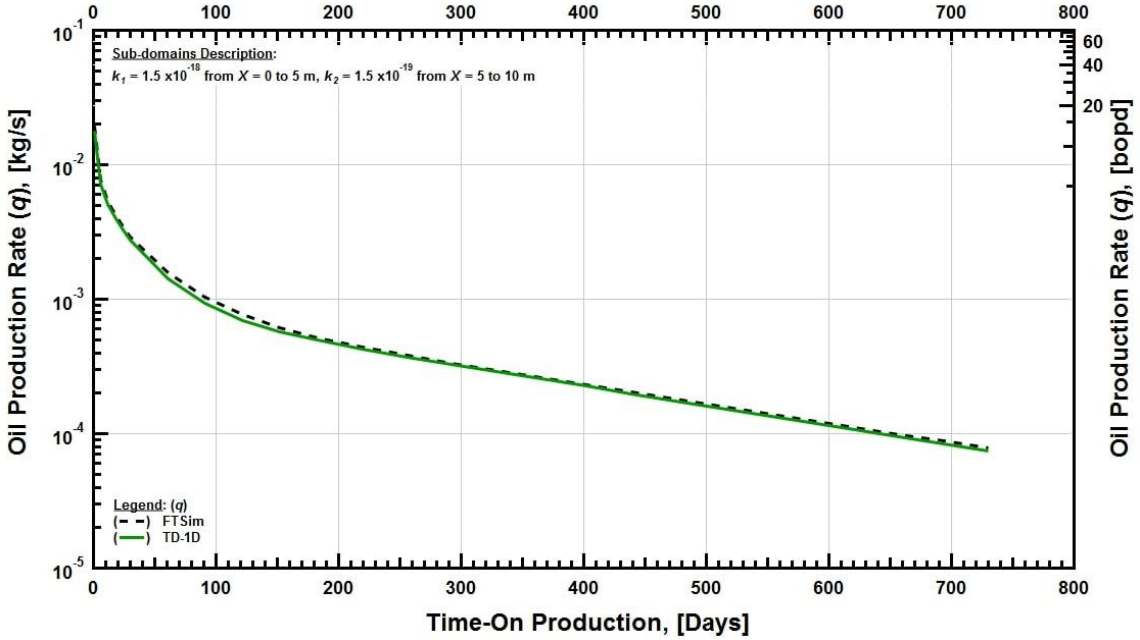

Figure 2.19— Case 5: Evolution of the production rate q over time at the HF at x = 0 for a constant bottomhole pressure pwf in a stencil with an SRV subdomain. The TD-1D predictions are based on a StA inversion (N_s = 8) and coincide with the corresponding DHM-based solutions.

2.4.2.4 Case 6: Linearly-Declining Production Rate q at $x = 0$, Partially-Penetrating HF

The dimensions of the partially-penetrating hydraulic fracture in Case 6 are shown in **Table 2.1**. As in Case 3, the production rate $q_{x=0}$ declines linearly from the original level of 3×10^{-4} (= 90 BOPD) to 2×10^{-4} (= 60 BOPD) over the 2-year production period. The evolution of the pressure spatial distribution in the 3D system is shown in the panels of **Fig. 2.20**. The results depicted here were obtained from TD-1D solution with the StA inversion, and fully coincide with the FTSim results. The pressure depletion at the middle of the HF (*i.e.*, at the base of the stencil, at $x = 0$, $z = 0$ and $0 \leq y \leq Y_F$) is more severe than in the case of full HF penetration, and conforms to expectations as it concentrates the same fluid removal rate through a smaller surface. **Fig. 2.20** shows the curvature of the 3D pressure system (which implicitly describe the 3D flow lines) and shows the unique capabilities of TDM in the analysis of 3D subsystems of shale oil reservoirs with partially penetrating HFs.

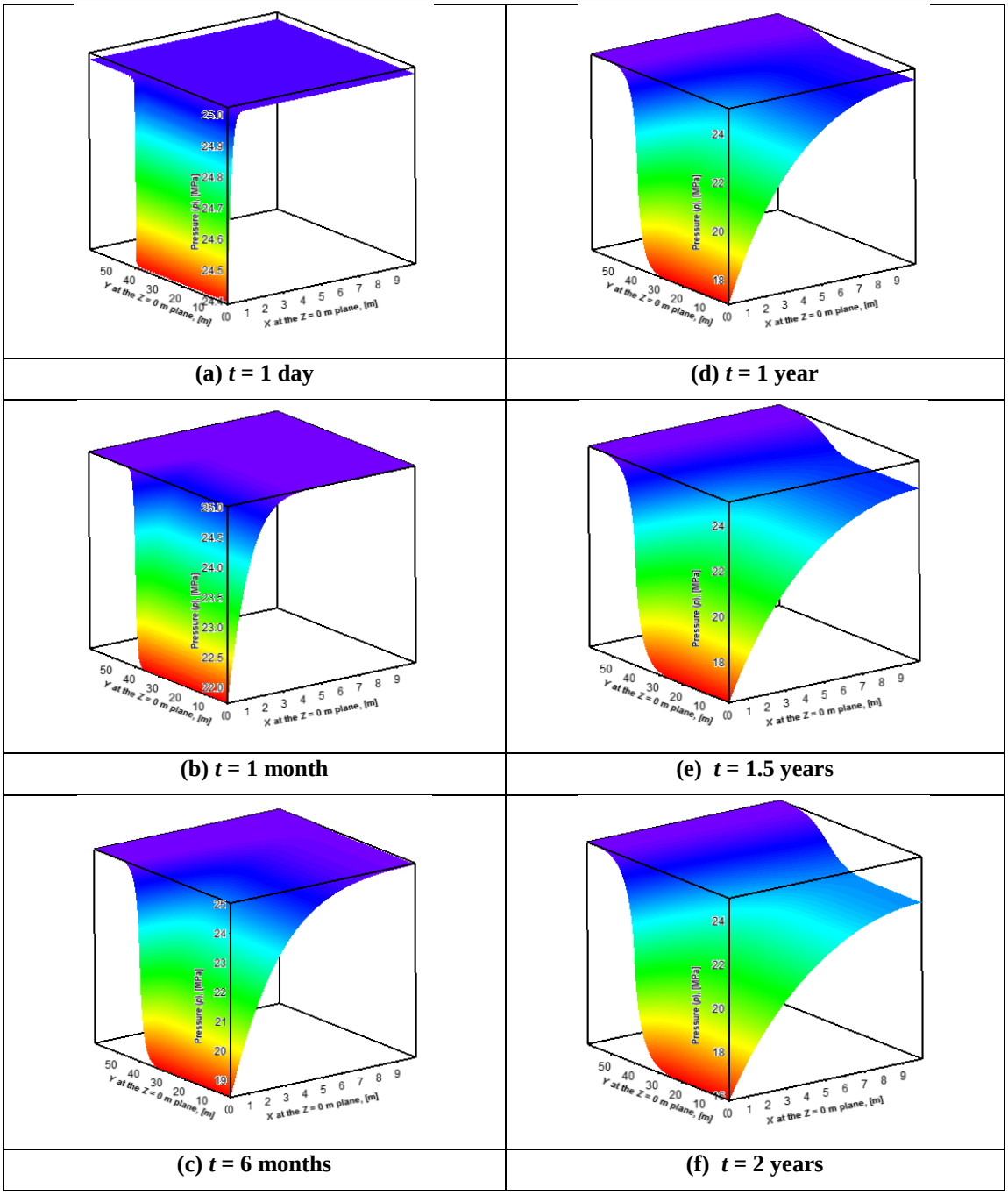

(a) t = 1 day | **(d) t = 1 year**

(b) t = 1 month | **(e) t = 1.5 years**

(c) t = 6 months | **(f) t = 2 years**

Figure 2.20— Case 6: Evolution of pressure distribution over time in the 3D domain of the stencil for a linearly-declining production rate, obtained from the application of the TD-1D method with the StA inversion (N_s = 8).

2.4.2.5 Case 7: Stepwise-Constant Production Rate q at $x = 0$ (Neuman Boundary)

This case is related to Cases 1 and 3, from which it differs in that the production rate $q_{x=0}$ is time-dependent in the stepwise-constant manner described by **Fig. 2.21**. This test was designed to demonstrate the unique power of the LT-component of the TDM solutions, which can yield accurate predictions at any point in the continuous time domain despite (and regardless of) any time variability in $q_{x=0}$. The FTSim and TD-0D results in **Fig. 2.22**, and the FTSim and TD-1D results in **Fig. 2.23**, show the evolution over time of the pressure distribution at the same locations discussed in Cases 1 and 3; they also provide a comparison of the effectiveness of the StA vs. the DHM inversions. In order to accurately capture the effect of $q_{x=0}$ variations with time, the FTSim simulations required very fine discretization in the vicinity of the step changes. The near-coincidence of the FTSim pressure results in **Figs. 2.22** and **2.23** with those obtained with the both inversion options in this demanding problem provides additional evidence and confirmation of the power, accuracy and flexibility of the TDM.

The better performance of the DHM-based results in **Figs. 2.22** and **2.23** is due to the superior ability of the method in the inversion of very sharp fronts, including step functions such as those imposed by the conditions depicted in **Fig. 2.21**. The StA-based inversions of the LT-space solutions tends to attenuate such sharp fronts. This can be seen in **Fig. 2.24**, which shows the evolution over time of the flowing bottomhole pressure p_{wf} obtained from the TD-1D method with both the StA and DHM inversions, as well as the corresponding FTSim solution. The FTSim results perfectly match the solutions obtained

from TD-1D with DHM inversions, but the StA-based TD-1D results show smoothing in the vicinity of the times when step changes occur. For the DHM inversion, the average deviation between the FTSim and both the TD-0D and the TD-1D results was 0.07%; for the StA inversion, the deviation was 0.09%. Nevertheless, both TD-1D solutions are more than satisfactory, further enhancing the confidence in the TDM approach.

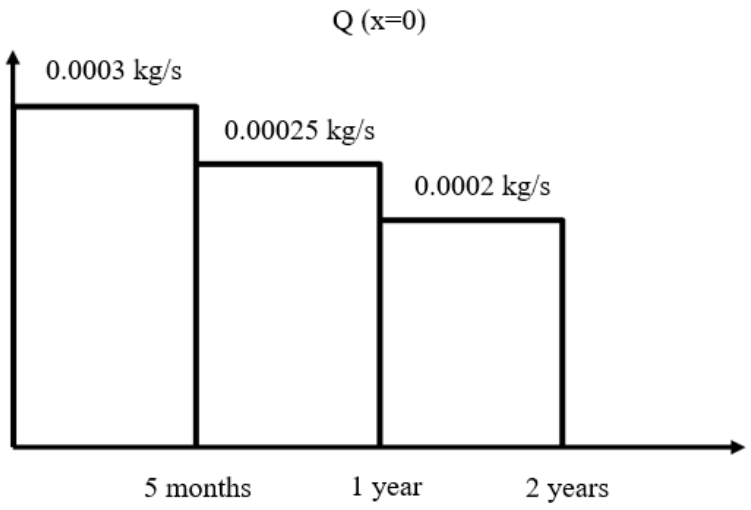

Figure 2.21— Case 7: The step-wise variations of $q_{x=0}$ with time in Case 7.

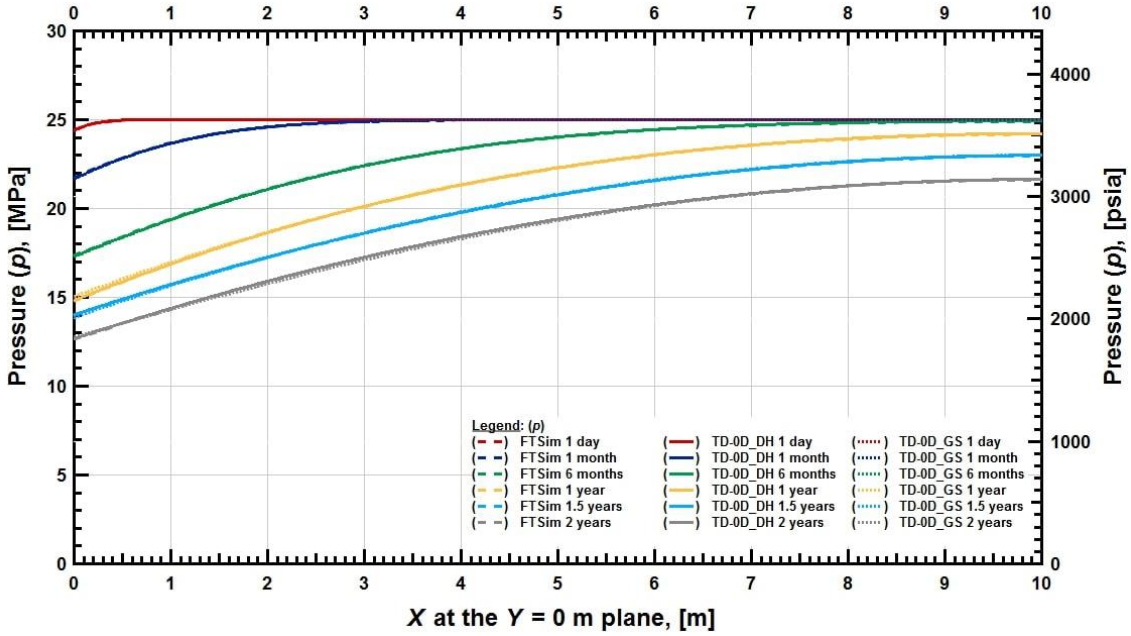

Figure 2.22— Case 7: Evolution of pressure distribution over time in the x-direction at $z = 0$ and $y = 0$ for the step-wise production rate q shown in **Fig. 2.21**: comparison of the FTSim solution to the TD-0D solutions with the StA ($N_s = 8$) and DHM ($M_H = 10$) inversions.

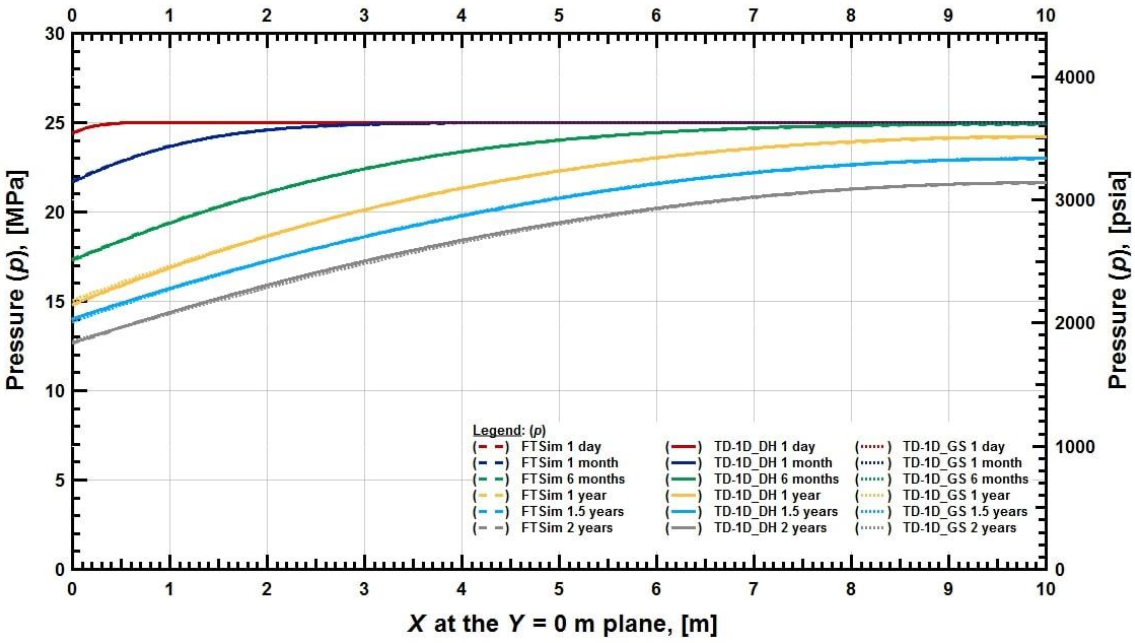

Figure 2.23— Case 7: Evolution of pressure distribution over time in the x-direction at $z = 0$ and $y = 0$ for the step-wise production rate q shown in **Fig. 2.21**: comparison of the FTSim solution to the TD-1D solutions with the StA ($N_s = 8$) and DHM ($M_H = 10$) inversions.

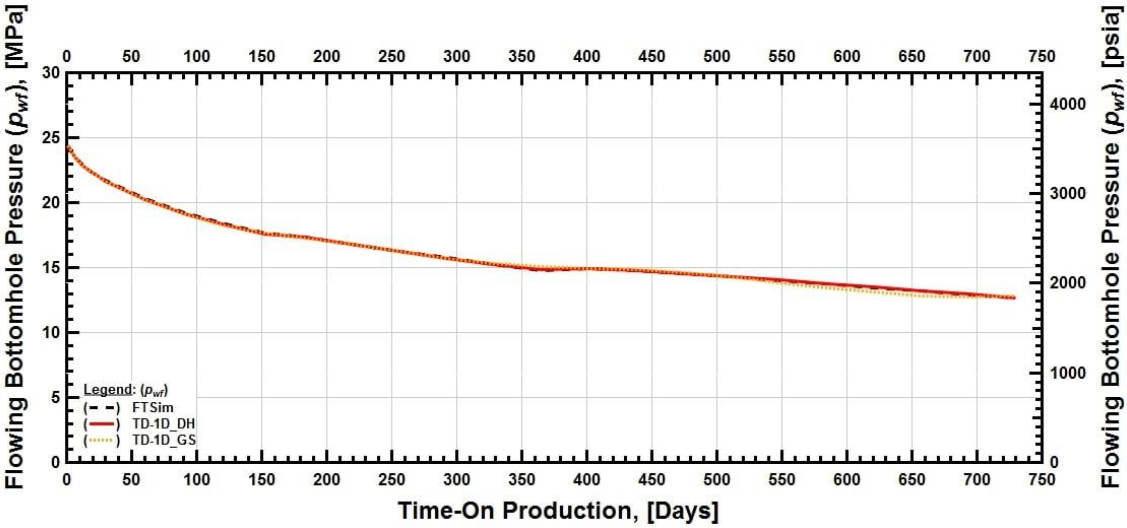

Figure 2.24— Case 7: Evolution of the flowing bottomhole pressure p_{wf} over time at $x = 0$ for the step-wise production rate q shown in **Fig. 2.21**: comparison of the FTSim solution to the TD-1D results with both the StA ($N_s = 8$) and the DHM ($M_H = 10$) inversions. Note the smoothing effect of the StA approach at the times of step changes in $q_{x=0}$.

2.4.2.6 Case 8: Stepwise-Constant Bottomhole Pressure p_{wf} at $x = 0$ (Dirichlet boundary)

This case differs from Cases 2 and 4 in that p_{wf} is time-dependent in the stepwise-constant manner described by **Fig. 2.25**. As in case 7, this test was designed to demonstrate the unique ability of the LT-based TDM solutions to yield accurate predictions at any point in the continuous time domain regardless of sharp changes in p_{wf}. The FTSim and TD-1D results in **Fig. 2.26** show the evolution over time of p at the same locations discussed in Cases 2 and 4, in addition to providing a comparison of the effectiveness of the StA vs. DHM inversions. To accurately capture the effect of the sharp p_{wf} variations, the FTSim simulations required very fine discretization in the vicinity of the step changes. There is a

practical coincidence of the FTSim results with the TD-1D solutions obtained with the DHM inversion, and an excellent agreement with the TD-1D solutions based on the StA inversion. The TD-1D method with either the StA or the DHM inversion provide very accurate pressure predictions. For the DHM inversion, the average deviation between the FTSim and the TD-1D pressure results was 0.28%; for the StA option, the average deviation was 0.42%.

The superiority of the DHM-based LT inversion is evident in **Fig. 2.27**, which shows the evolution of the production rate q calculated from (a) FTSim and (b) from TD-1D with the two LT inversion options. The very fine temporal discretization about the time of the stepwise change in p_{wf} allows FTSim to capture accurately the production 'spikes' that are caused by the augmented pressure drop, and these are effortlessly matched by the TD-1D solution with the DHM inversion when the number of the M_H terms is raised to 14 (see **Table 2.1**). The inability of the StA inversion to accurately capture sharp fronts results in the 'smearing' (smoothing) of the spikes in the q curve. Thus, the Stehfest (1970a;b) method is not recommended for TD-1D if the study aims to determine the q associated with this type of p_{wf} scenario. The TD-1D solution with the DHM inversion has a superior performance, providing accurate and reliable predictions of the flow and production behavior in multi-fractured shale oil reservoirs. Actually, the ability of the method to accurately incorporate sharp temporal changes into its solutions without attenuation or smoothing sharp effects and events makes it a superior choice over numerical simulators,

which often do not invest the necessary effort for the careful implementation of a very fine time discretization in order to accurately capture such sharp changes.

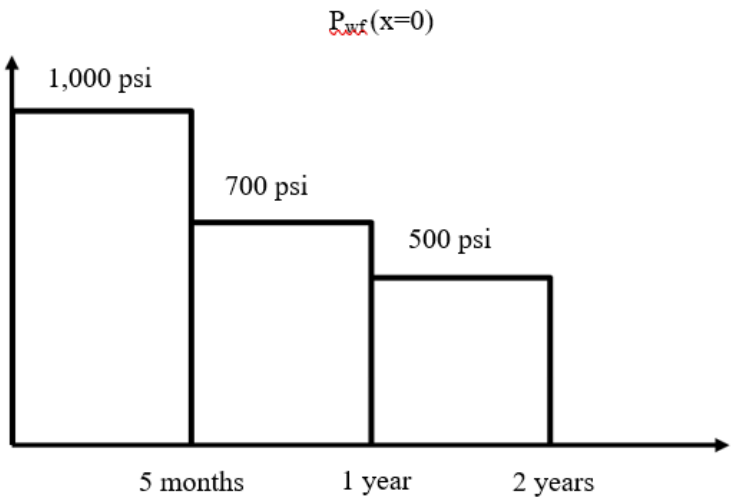

Figure 2.25— Case 8: The step-wise variations of p_{wf} with time in Case 8.

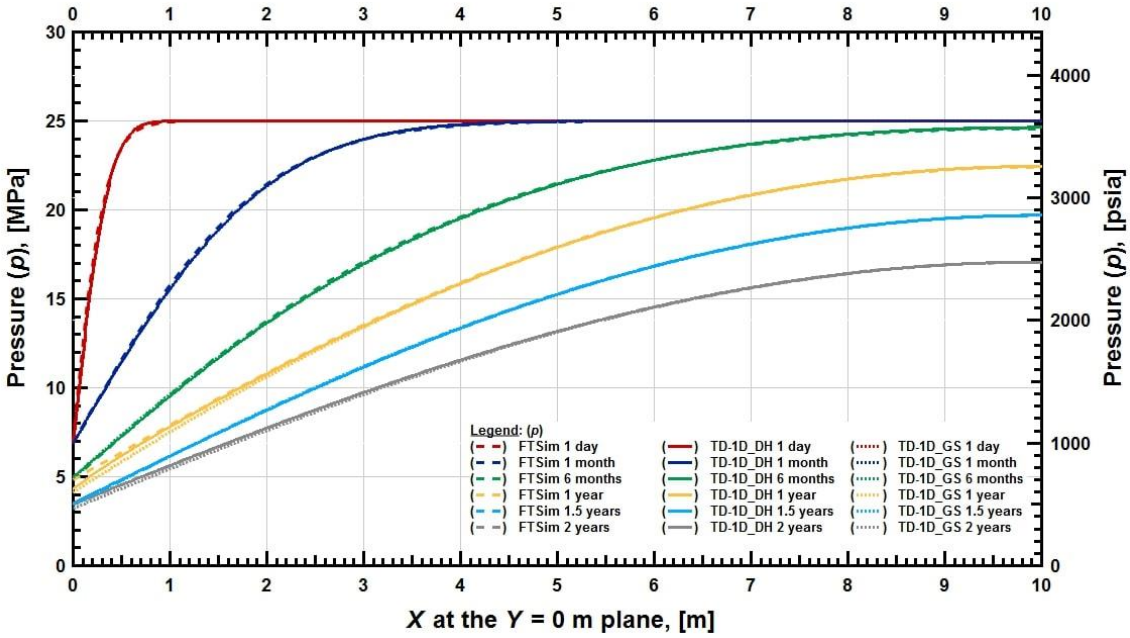

Figure 2.26— Case 8: Evolution of pressure distribution over time in the x-direction at $z = 0$ and $y = 0$ for the step-wise boundary pressure p_{wf} shown in **Fig. 2.25**: comparison of the FTSim solution to the TD-1D solutions with the StA ($N_s = 8$) and DHM ($M_H = 14$) inversions.

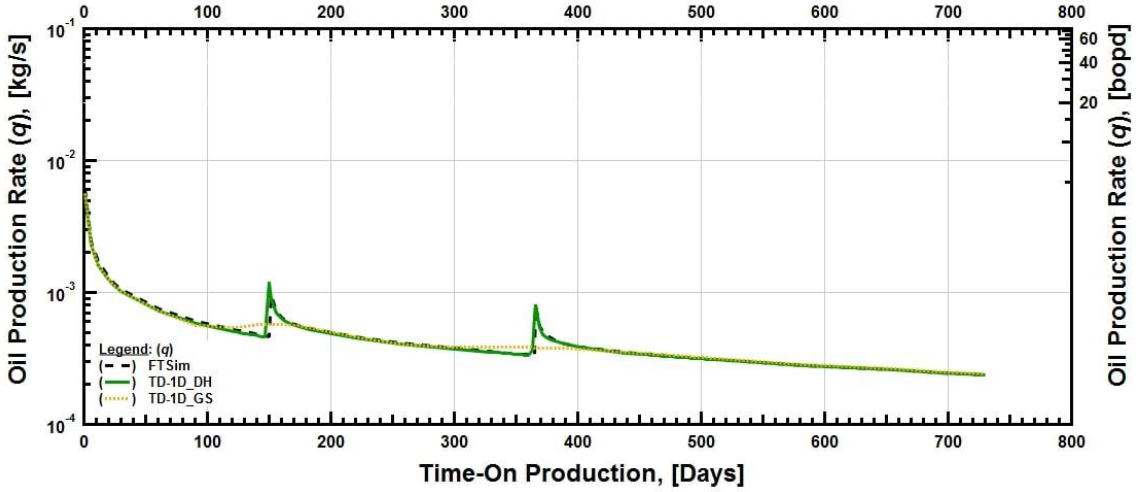

Figure 2.27— Case 8: Evolution of the production rate q over time at $x = 0$ for the step-wise boundary pressure p_{wf} shown in **Fig. 2.25**: comparison of the FTSim solution to the TD-1D results for both the StA ($N_s = 8$) and DHM ($M_H = 14$) inversions. Note the smoothing effect of the StA approach about the times of step change in p_{wf}.

2.5 TDM Execution Times

The execution times for TDM at 1001 locations in the domain, and for the FTSim solutions for the same problems were recorded and compared in order to provide an additional criterion for the evaluation of the power and efficiency of TDM.

Regarding computer storage, there can be no scalable comparison between a numerical simulator and TDM. The FTSim grid for the numerical simulations in this study exceeded 115 MB in size, and multiples of that were needed for storage of the variables describing the attributes of each element and for storage of the coefficients of the matrix equation.

The elimination of spatial discretization in TDM reduces the memory requirements for the method to practically negligible levels.

We investigate the computational efficiency of TDM, as quantified by the execution time on a specific computational platform, against that for the FTSim numerical simulator. This was not an easy task because of the necessity to use different computational platforms because of the very large requirements of FTSim that necessitated the use of a cluster, leading to comparisons of unequal quantities. However, the information gleaned from this comparison was sufficient to demonstrate the advantages of TDM. The FTSim simulations were conducted on the LR4 cluster of Lawrencium at the Lawrence Berkeley National Laboratory (LBNL, 2019). Each FTSim run involved 384 cores, and the runs required a minimum of one and up to two 12-hour cycles (depending on the type of the problem) to cover the 2-year production period. Dirichlet-type boundaries required longer execution times because of the drastic pressure gradient at the HF boundary at $t = 0$, which created very steep solution surfaces posed numerical challenges and required short timesteps. The number of cores and the length of the execution times provide a measure of the computational effort for the FTSim solutions.

We also compared the relative performance (in terms of execution speed) of the PTD-1D and PTD-0D options for the same LT inversion method, and the relative performance of the StA and DHM inversions for the same TDM option. The basis for the comparisons was the execution speed for the computation of the pressures at 1001 at the end of 2 years

of production, *i.e.*, at a time when the domain pressure is substantially depleted. The execution time is insensitive to the time at which solutions are desired because there is no time discretization in TDM; it takes about the same computational effort (and execution time) to compute solutions at any time with the StA inversion. The situation is different for the DHM because its properties allow that solutions at any time t $\left(0.2T \le t \le T\right)$ can be obtained almost instantaneously once the solution for T is computed, *i.e.*, just one set of computations suffices for the estimation of solutions at any time within an entire order of magnitude of T.

TD-0D cannot handle subdomain heterogeneity, and is suitable for pressure predictions at any location (x,y,z) in homogeneous domains only. Systems with subdomain heterogeneity can be easily handled by PTD-1D. In their application, neither TD-0D nor TD-1D requires spatial discretization.

Table 2.2 shows the execution times for both TDM options in all cases (1 to 8) when the LT inversions are carried out by the StA. The corresponding execution times for DHM-based inversions in the most interesting cases are listed in **Table 2.3**. All serial computations were performed using the Microsoft Visual Studio Community 2017 (Version 15.9.15) and a platform with Intel R CoreTM i7-7700HQ@2.80 GHz processors (8CPUs) running serially on Windows 10 Home 64-bit (10.0, Build 18362). The parallel (Open MP-based) computations in Case 6 (denoted by an asterisk in **Table 2.2**) were carried out on a MacPro running MacOS version 10.12.26 with 12 Intel Xeon E5 cores.

The much longer execution time for Case 6 is caused by the need to compute a large number of cross products when a partially-penetrating fracture is involved.

The results in **Tables 2.2** and **2.3** provide clear evidence of the superiority of the TD-1D over the TD-0D option in terms of computational efficiency, as the execution times for the latter are orders of magnitude larger than those for the former. This observation holds true for StA inversions (**Table 2.2**) and for the slower DHM inversions (**Table 2.3**). Considering its other advantages, *i.e.*, its superior accuracy and applicability to heterogeneous domains, TD-1D appears to have an overwhelming advantage over TD-0D. As expected, DHM-based solutions (**Table 2.3**) are slower than those obtained from StA inversions (**Table 2.2**), but by margins that are practically trivial in TD-1D applications.

Caution needs to be exercised in the interpretation of the data in **Table 2.3**, as these results can easily misinterpreted and the longer execution times may be misleading; these immediate observations need to be tempered by the realization that a single DHM-based solution can provide results at any time within the same order of magnitude of time, thus significantly reducing the actual execution time for the DHM-based solution if results at different times are desired– in other words, the DHM-based solution may be faster that what **Table 2.3** suggests in realistic applications. Finally, consideration of the computational effort required for the FTSim solutions leads to the realization that even the

serial TDM solutions can be multiple orders or magnitude faster than a corresponding numerical 3D solution, thus further enhancing the attractiveness of the method.

Table 2.2 — Execution Times for TDM with Stehfest algorithm Inversion.

Execution time (sec) of 1001 locations		**TD-0D**	**TD-1D**
Case 1	Constant rate	44.218	0.668
Case 3	Linearly-declining rate	43.730	0.661
Case 7	Step-declining rate	43.052	0.637
Case 2	Constant pressure	54.873	0.636
Case 4	Linearly-declining pressure	54.389	0.621
Case 8	Step-declining pressure	55.977	0.661
Case 5	Constant pressure with sub-domains	N/A	0.717
Case 6	Linearly-declining rate with partially penetrating fracture (serial)	N/A	43723.32
Case 6	Linearly-declining rate with partially penetrating fracture (parallel, OpenMP)*	N/A	3842

Table 2.3 — Execution Times for TDM with DeHoog method Inversion.

Execution time (sec) of 1001 locations		**TD-0D**	**TD-1D**
Case 1	Constant rate	352.398	0.836
Case 3	Linearly-declining rate	345.959	0.845
Case 7	Step-declining rate	346.403	0.928
Case 2	Constant pressure	191.563	0.968
Case 4	Linearly-declining pressure	188.241	0.965
Case 8	Step-declining pressure	191.436	1.039

2.6 TDM Summary

The Transformational Decomposition Method (TDM) is a fast analytical and/or semi-analytical method for the analysis of the oil flow, pressure interference and production from multi-fractured ultra-low permeability (ULP) reservoirs such (as shale oil reservoirs) serviced by parallel horizontal wells. The method begins by recasting the 3D diffusivity PDE of oil flow through porous and fractured media in terms of a primary variable that completely linearizes the PDE without any loss of generality. Time is then eliminated from the resulting linearized 3D PDE by means of Laplace transforms. The subsequent 'Decomposition Stage' involves the application of successive Finite Cosine Transforms (FCTs) to eliminate either (a) all three dimensions, yielding a simple algebraic equation or (b) two dimensions, yielding an ODE in time only.

In the final 'Reconstruction Stage', the solutions of the multi-transformed space equations are inverted in a reverse order than that followed in the Decomposition Stage, *i.e.*, the first coordinate to be restored is the last direction to be eliminated by FCTs during the Decomposition Stage, and the last inversion is that of the Laplace Transformed primary variable. The TDM process yields solutions that are analytical in all three spatial coordinates and semi-analytical in time because of the need for numerical inversion of the Laplace space solution. This is dictated by the inability to obtain closed-from relationships of the time dependence of the primary variable by inverting analytically the complex 1D or 0D solutions resulting from the elimination of space.

TDM is applicable to problems of single-phase oil flow, *i.e.,* above the bubble point and/or when aqueous and the gas phases are either not present or immobile. Using 3D stencils (the minimum repeatable elements in the horizontal well and hydraulically-fractured system) as the basis of our study, we developed the theoretical basis and obtained solutions over extended production times in cases involving (a) a range of isotropic and anisotropic matrix and fracture properties, (b) constant and time-variable production regimes (rates or bottomhole pressures), and (c) combinations of SRV and non-SRV subdomains. Work is in progress to address areas in which the current form of TDM is not currently applicable, *i.e.,* in multiply heterogeneous domains involving several subdomains (including HFs with measurable pressure losses), prescribed (constant or time-variable) pressure conditions at partially-penetrating HFs, more realistic geometries and location of boundaries, etc.

Compared to conventional numerical simulators, TDM offers some significant advantages. It eliminates space discretization and results in a simple 1D ODE or an algebraic equation in multi-transformed spaces, both of which have simple analytical, closed form solutions. It also eliminates time discretization, yielding solutions continuous in time. The avoidance of space and time discretization allows predictions only at the desired points in space and time, without the wasteful need of numerical simulators to obtain results at times and locations of no interest. TDM reduces drastically (easily by orders of magnitude) some of the key requirements of (and challenges facing) conventional simulators, input and output data volumes and processing; computer memory

for the storage of the elements of the discretized domain and their attributes, as well as for the storage for the very large matrix equations arising from the space and time discretization; the execution times to process these data, but mainly to solve the large matrix equations. The limited input data requirements make the application of TDM easy to use and reduces the need for highly trained personnel to conduct the simulations. The elimination of the need for spatial discretization not only reduces the execution times but also eliminates the time and the specialized-personnel effort that are required to create a grid system (a tedious and complicated process that demands significant expertise and a large number of inputs).

Both TDM versions (TD-1D and TD-0D) provide accurate solutions that deviate from the numerical solutions of the same problems by minuscule amounts (and there are reasons to expect TDM solutions to be the more accurate ones). Of the two versions, TD-1D appears to be by far the superior option; it can be multiple orders of magnitude faster than a standard numerical solution and routinely more accurate in the vicinity of subdomain boundaries because it does not suffer from discretization errors; it is 1-2 orders of magnitude faster than TD-0D, and can resolve accurately any number of heterogeneous subdomains (such as SRVs). Conversely, the accurate but much slower TD-0D method (which can still be orders of magnitude faster than a standard numerical solution involving discretized space and time) is conceptually inapplicable to systems with heterogeneous subdomains. In the presence of the more powerful TD-1D method, the usefulness of TD-0D is limited. The reason for the slow behavior of TD-0D is the significant expansion of

the computations when the 3rd dimension is eliminated by the last FCT (a process that yields triple summations in the equations to invert), and the emergence of a large number of cross products (when the third dimension is eliminated) that converge slowly upon inversion.

In this study we considered two methods for the numerical inversion of the Laplace space solutions; the Stehfest algorithm (StA - 1970a;b) and the method of DeHoog et al. (DHM - 1982). The StA-approach is easy to implement, requires only real values for the computation of the Laplace space parameter and provides faster TD-1D and TD-0D solutions, and resolve very accurately most problems. Its performance may deteriorate in the analysis of production regimes with sharp changes in the production rate or bottomhole pressure, in which cases it may have the tendency to smoothen performance spikes. The second inversion method can easily handle sharp fronts and very dynamic changes in the production schedules but requires complex values for the computation of the Laplace space parameter and is much more complex to implement. It may or may not be slower that StA, depending on the number of desired observations within each order of magnitude of the production period.

Because of its simplicity, ease of application and speed, TDM is particularly useful for the evaluation of 'what-if' scenarios and identification of the factors, conditions and properties that dominate the production behavior of shale oil reservoirs, and to provide indications of their production potential before the onset, or at the early stages, of full production

operations (when limited data are available on the reservoir and its properties). Thus, TDM can provide a large number of production estimates (a task much more difficult, if not impossible, for large conventional simulators involving very large numbers of elements) to define the envelope of the possible system performance, and offers the additional benefit of being able to describe processes and phenomena that can only be captured at spatial scales (as low as at the mm-level) that are beyond the capabilities of most numerical simulators, and which may have a significant impact on production. Because of the ability of stencils to accurately predict production by a simple summation of the stencil-based results, reliable estimates of the expected production from horizontal wells can be obtained after properly accounting for the contribution of boundary stencils.

TDM is thus a very useful tool for the analysis of pressure interference in multi-fractured ultra-low permeability reservoirs serviced by parallel horizontal wells. Another very significant potential application of TDM is in history matching and reservoir parameter identification, which is a difficult, cumbersome and lengthy process in full 3D studies of numerical simulators involving large numbers of elements and covering long production periods. The large number of computations needed for this process can be conducted very effectively using the fast TDM solutions to provide estimates of the reservoir properties which, if there is a need for further refinement, can be used as starting points in conventional, numerical-based history matching analyses. Note that the TDM, with its large number of mutually independent summations in the computation of the inverse FCTs and LTs, lends itself to parallel processing for even faster and more efficient performance.

CHAPTER III

DEVELOPMENT AND APPLICATION OF THE PARTIALTRANSFORMATIONAL DECOMPOSITION METHOD (PTDM) TO THE PROBLEM OF THE 3D GAS FLOW THROUGH FRACTURED MEDIA

This chapter discusses in-detail the development of PTDM-based for the solution of the problem of gas flow through, and production from, a multi-fractured shale gas reservoir. PTDM an adaptation of the TDM (Moridis, 1995) —originally developed a slightly compressible fluid flow—to highly compressible gas flow. In the following sections, we present the development of the mathematical basis of PTDM, we provide validation examples and demonstrate the application of the method to the solution of complex 3D problems of gas flow through matrix and fracture systems.

3.1 Objectives and General Description of the Partial Transformational Decomposition Method (PTDM)

The objective of this effort is to develop and introduce the Partial Transformational Decomposition Method (PTDM) for the solution of the flow equation of highly compressible fluids such as gases in multi-fractured ULP reservoirs. The reason for the "partial" moniker is because of the strong non-linearity in the compressibility and viscosity of gases (caused by their strong dependence on pressure) precludes the use of Laplace transforms over the entire time domain, forcing discretization of time either using a simple

backward FD approximation of the time derivative or applying a localized LT within each time subdomain (timestep).

The problem of intense non-linearity in the gas flow equation is partially addressed by the use of a primary variable based on the concept of pseudo-pressure (Al-Hussainy, 1966). This approach enables the removal of all non-linear terms associated with the spatial derivatives in the PDE of flow and concentration of all non-linearities in variables that are associated only with the time derivative. The elimination of non-linearities in the spatial derivates allows the application of successive Finite Cosine Transforms (FCTs) to the pseudo-pressure-based 3D diffusivity equation of gas flow, leading to the elimination of the corresponding dimensions. For production at a defined rate q, 3 levels of FCTs yield a 1st-order ODE in time only. For production in response to a defined boundary pressure p_{wf}, 2 levels of FCTs lead to a 1D 2nd-order PDE in space and time. Thus, PTDM is a hybrid numerical-analytical method. The implicit numerical solutions to the FCT-based equations in the multi-transformed spaces are inverted, providing solutions that are analytical in 2 or 3 space dimensions, numerical in time, and account for the non-linearity of gas flow.

PTDM offers some significant advantages over conventional numerical simulators. It minimizes grid discretization, limiting it to a single dimension (instead of 3 dimensions) or to no dimension at all (in which case solution at any point is possible, as no discretization is required). This can drastically reduce input data requirements, computer

memory requirements and execution times, often by orders of magnitude. The minimization or elimination of the grid discretization requirement not only reduces the execution times, but also saves the time and effort that would be expended in the creation of a grid system. Because of the limited input data requirements, it is easy to use and to train personnel in its use. It can be particularly useful during planning and the initial evaluation of the production potential of the reservoir, as well as during the early stages of production — *i.e.*, at times when not much information is available on the reservoir and its properties.

The speed of the PTDM execution allows the execution of many "what-if" scenarios of reservoir properties, thus making possible the definition of the envelope of possible solutions of production performance. Additionally, the speed of PTDM is particularly useful in the analysis of early (as will be seen in a subsequent section) production data, as it can lead to very fast and efficient history matching and parameter identification. This process can be difficult, cumbersome and lengthy if history matching is based on a full 3D model numerical model using 100,000s of elements and covering a long production period.

3.2 PTDM Approach and Implementation

3.2.1 Underlying Assumptions

Application of the PTDM involves several assumptions. These include single-phase gas flow (if there is an aqueous phase, it needs to be immobile and the permeability in the matrix is the effective permeability); the hydraulic fracture (HF) has a very high permeability, with flow exhibiting negligible pressure loss along and across it (a modification of the PTDM to eliminate this assumption is in progress); gas flow is isothermal; the flow properties are homogeneous within regularly-shaped subdivisions of the TDM, although the domain may be heterogeneous as a whole; the size of the horizontal well is very small compared to the dimensions of the domain (a reasonable assumption); and gravitational effects are negligible (a valid assumption, given the high pressure of the system, the limited thickness of the reservoir and the relatively low density of the gas).

3.2.2 The PTDM Simulator and the Code Validation Approach

The PTDM solutions were coded in FORTRAN90. The PTDM results were compared to the results obtained from the FTSim numerical simulator with a gas property module. FTSim is a simplified version of the TOUGH+ simulator (Moridis and Pruess, 2016) with the RealGasBrine V1.0 option (Moridis and Freeman, 2016—referred to as RGB), which has been validated through comparisons to a wide range of analytical and numerical solutions (Moridis and Freeman, 2014; 2016; Reagan et al., 2015). As is the case of TOUGH+, FTSim is a family of codes that provides a general-purpose simulation

framework (based on the Integral Finite Difference (IFD) method for space discretization) for the solution of a variety of problems of non-isothermal fluid flow through porous and fractured media.

3.2.3 The PTDM Simulation Domain

The domain of the system used in the PTDM solutions is the stencil of a multi-fractured shale gas system produced by means of horizontal wells, and is the same (in terms of general characteristics) as the stencil used in the TDM simulations (see Section 2.2) and depicted in **Fig. 2.1**. The reasons for the use of the stencil and its adequacy in describing the performance of the entire system of a multi-fractured horizontal well in shale gas reservoirs have been fully explained in the discussion of the domain used in the TDM studies, and will not be repeated here. Note that the spatial discretization of the Cartesian stencil for the FTSim simulations that are used for comparison to, and validation of, the PTDM solutions resulted in over 220,000 cells (with spatial discretization beginning at the mm-level next to the HF) and the same number of equations because of the assumption of isothermal flow. The very fine discretization in the vicinity of the HF is necessitated by the very steep gas pressure fronts caused by the ultra-low permeability of the matrix of shale gas reservoirs.

3.2.4 Properties, Initial and Boundary Conditions

The gas composition in this study was 100% methane. The reservoir properties and the initial pressure P_i and temperature T are listed in **Table 3.1**. The boundary conditions are no-flow (Neuman) boundaries at $x = L_x$, $y = 0$, $y = L_y$, $z = 0$ and $z = L_z$ because of symmetry; at the $x = 0$ location and outside the face (footprint) of the HF, there is also a no-flow boundary; at the *same* location and on the face of the HF, there may exist either a constant- or time-variable pressure boundary (Dirichlet conditions) or a constant- or time-variable rate boundary (described by a Neuman condition).

3.2.5 Overall PTDM Approach and the Treatment of the Nonlinearities

The original pressure-based equation of gas flow is first transformed using a pseudo-pressure primary variable that removes all non-linearities from the space derivatives and transfers them to a factor preceding the time derivative. The new form of the gas diffusivity equation is then transformed through series of FCTs. The first and second FCTs are performed along coordinates with known no-flow (Neuman-type) boundaries. In the stencil of **Fig. 2.1**, these are the *z* and *y* coordinates, and result in an 1D PDE in space and time that can be solved numerically using a FD approximation in space and time, thus drastically reducing the size of the problem compared to a full 3D numerical solution. There is also the option of further transforming the 1D PDE by applying an additional FCT to the *x*-coordinate, yielding an ODE in time in which space no longer exists and which can be solved either numerically or semi-analytically.

The strong non-linearities associated with the time derivative of the PDE of gas flow prohibit analytical solutions that cover the entire time domain, and the only options are either numerical FD solutions or piece-wise analytical solutions. This requires the use of time steps that are sufficiently short to ensure that the non-linear terms remain practically constant during them, and is achieved by limiting the maximum pressure change ΔP between successive timesteps to < 2.5% of the initial P_0 (**Fig. 3.1**). Once the solution in space and time is obtained, it is possible to keep the values of the non-linear terms constant at their level at the beginning of the time-step, or to continuously update them through an iterative process that is expected to converge fast.

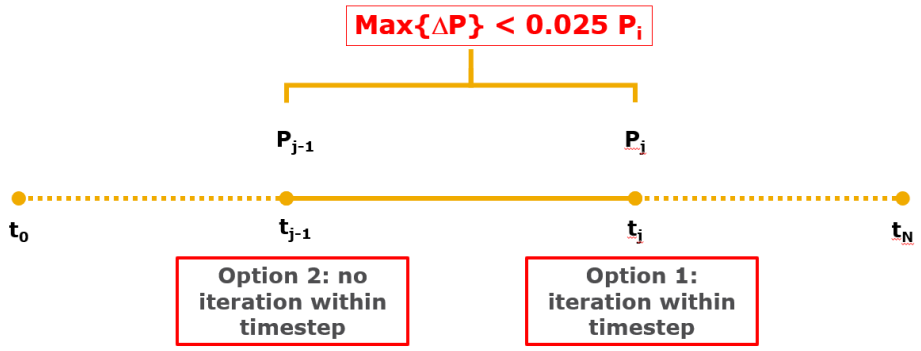

Figure 3.1 — PTDM non-linearity assumption options: the value of the non-linear terms can be constant and equal to those at the beginning of the time-step, or they can be continuously updated during the time-step.

The solutions in the multi-FCT-transformed-space (either the 1D PDE or the 0D ODE) at each time step are then inverted to yield solutions of the value of the primary (pseudo-

pressure-based) variable in space and time. In the next step, using appropriate correlations, the actual pressures at the desired locations in space are extracted from the primary variables at that timestep.

3.3 PTDM Development

3.3.1 The General Equation of Flow

Following Al-Hussainy et al. (1966) and ignoring gravitational effects, the general equation of gas flow in a porous medium is described as

$$\sum_{d^\circ=x,y,z} k_{d^\circ} \frac{\partial^2 \psi}{\partial d^{\circ 2}} = \phi \mu c_t \frac{\partial \psi}{\partial t} \quad \text{..... (3.1)}$$

where

$$\psi = \frac{\xi - \xi_r}{\xi_0}, \xi = u_0 \int_{P_i}^{P_{actual}} \frac{P}{\mu Z} \, dP \quad \text{..... (3.2)}$$

$$\rho = \frac{PM}{ZR_{gas}T}, \quad \phi = \phi_0 e^{c_m(P-P_0)}, \quad c_t = \frac{1}{P} - \frac{1}{Z}\frac{dZ}{dP} + c_m \quad \text{..... (3.3)}$$

and

c_m = the pore compressibility, Pa^{-1}

c_t = the total compressibility of the system, Pa^{-1}

M = the gas Molecular weight, kg/mol

μ = the gas viscosity, Pa-s

P = the pressure, Pa

ϕ = the porosity, fraction

ξ = the pseudo-pressure

ψ = the primary variable as defined by Eq. 3.2

R_{gas} = the real gas constant, Pa-m^3/mol/K

ρ = gas density, kg/m^3

T = temperature, K

u_0 = pseudo-pressure factor, Pa^{-1}s^{-1}

Z = the gas compressibility

r = an appropriate reference state

0 = the initial reservoir conditions

Note that the pseudo-pressure-based formulation completely removes non-linearities from the LHS of Eq. 3.1, concentrating these in the μc_t term on the right-hand side.

The non-linearities caused by the strong dependence of the gas compressibility and viscosity on pressure require the availability of reliable equations relating (a) pressure to pseudo-pressure and (b) pseudo-pressure to the combined term μc_t in Eq. 3.1. Typical examples of these relationships are shown in **Figs. 3.2** and **3.3**. Note that the needs of PTDM require the ability to obtain very accurate values in both the forward and inverse application of these equations.

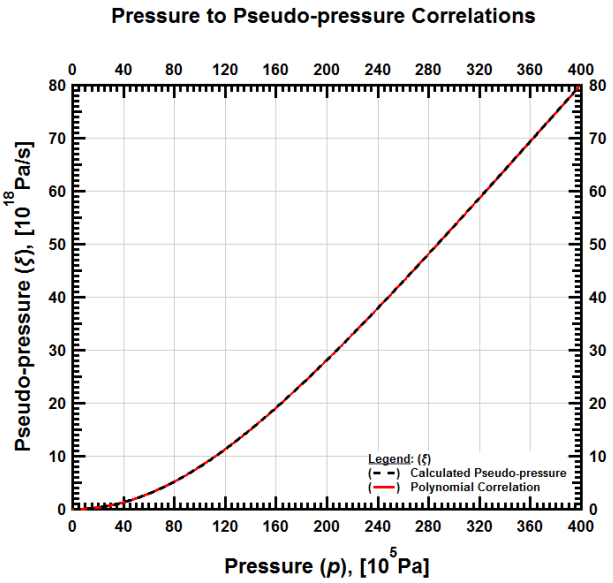

Figure 3.2 — The pressure to pseudo-pressure relationship can be correlated with a polynomial function.

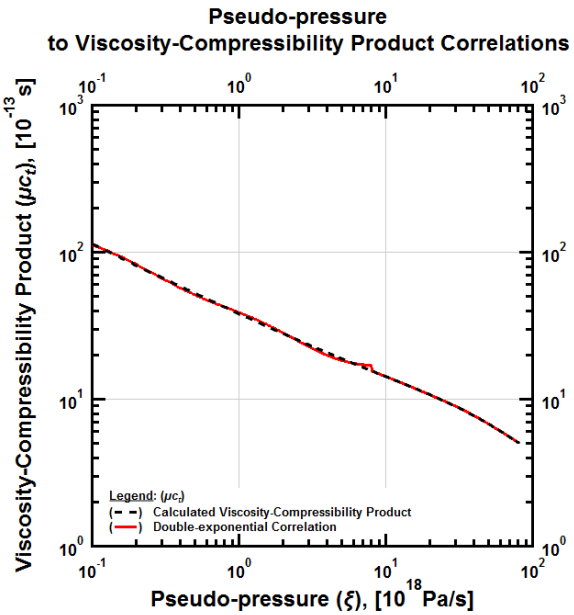

Figure 3.3 — The pseudo-pressure to the combined term μc_t relationship can be correlated with a double-exponential function.

This means that, beginning with a certain pressure and obtaining the corresponding pseudo-pressure through a forward equation, we need to be able to retrieve the initial pressure through the inverse relationship accurately to at least 14 decimal places. This is achieved by applying the secant root finding method to the forward relationships to obtain the inverse relationships.

For constant-rate q (= A_F Q) production, *i.e.*, Neuman boundary conditions, the reference state is that of the initial reservoir conditions; for constant-bottomhole pressure production (Dirichlet boundary), the reference state is that of the bottom-hole pressure p_{wf}. The standard value of term $u_0 = 2$, although the value $u_0 = \frac{\mu_0 Z_0}{P_0}$ has been used (Al-Hussainy, 1966).

For Neuman boundary conditions, the constant or time-variable flux Q is described as

$$Q_{x=0} = Q_{x=0}(t) = \frac{k_x \rho}{\mu} \frac{\partial P}{\partial x}\bigg|_{x=0} = k_x \frac{M}{R_{gas} T u_0} \frac{\partial \xi}{\partial x}\bigg|_{x=0} = k_x \frac{M \xi_0}{R_{gas} T u_0} \frac{\partial \psi}{\partial x}\bigg|_{x=0} \quad \text{..... (3.4)}$$

3.3.2 Decomposition Stage: Neuman Inner-Boundary Conditions

3.3.2.1 Step D1: The First Finite Cosine Transform of the Gas Flow Equation in the z-Direction

The FCT-1 of the z-coordinate in Eq. 3.1, and considering $Q_{z=0} = Q_{z=L_z} = 0$, yields the following PDE in the (x+y+l+t) space:

$$\sum_{d^\circ = x,y} k_d \frac{\partial^2 \omega}{\partial d^{\circ 2}} - \left[k_z \left(\frac{l\pi}{L_z} \right)^2 \right] \omega = \phi \mu c_t \frac{\partial \omega}{\partial t} \quad \text{..... (3.5)}$$

where $\omega = \mathcal{F}_{c1}\{\psi\}$ and *l* is the integer parameter of the FCT-1 space corresponding to the z-coordinate. At this step we also obtain $\left.\frac{\partial \omega}{\partial x}\right|_{x=0} = \mathcal{F}_{c1}\left\{\left.\frac{\partial \psi}{\partial x}\right|_{x=0}\right\}$ using Eq. 3.4.

3.3.2.2 Step D2: The Second FCT of the Gas Flow Equation in the y-Direction

Taking the FCT-1 of the *y*-coordinate in Eq. 3.5, and considering $Q_{y=0} = Q_{y=L_y} = 0$, we obtain the following PDE in the (*x*+*n*+*l*+*t*) space:

$$k_x \frac{\partial^2 \varphi}{\partial x^2} - \left[k_y \left(\frac{n\pi}{L_y} \right)^2 + k_z \left(\frac{l\pi}{L_z} \right)^2 \right] \varphi = \phi \mu c_t \frac{\partial \varphi}{\partial t} \quad \text{..... (3.6)}$$

where $\varphi = \mathcal{F}_{c1}\{\omega\}$ and *n* is the integer parameter of the FCT space corresponding to the *y*-coordinate.

At this point, the original 3D PDE in space and time has been reduced to an 1D PDE. The PTDM process at this stage also requires estimating $\left.\frac{\partial \varphi}{\partial x}\right|_{x=0} = \mathcal{F}_{c1}\left\{\left.\frac{\partial \omega}{\partial x}\right|_{x=0}\right\}$.

As for the next step in PTDM, there are two possibilities; the first is to solve Eq. 3.6 to obtain φ using a standard Finite Difference (FD) method. The second alternative is to proceed to Step D3 (discussed below).

3.3.2.3 Step D3: The Third FCT of the Gas Flow Equation in the x-Direction (Optional)

Applying the FCT-1 to the 2nd derivative in the *x*-coordinate in Eq. 3.6, and considering $Q_{x=L_x}=0$ and $Q_{x=0}=k_x\dfrac{M\xi_0}{R_{gas}Tu_0}\dfrac{\partial P}{\partial x}\bigg|_{x=0}$ (and its previous transformations), we obtain the following ODE (in time only) in the (m+n+l+t) multi-transformed space:

$$-\left[k_x\left(\frac{m\pi}{L_x}\right)^2+k_y\left(\frac{n\pi}{L_y}\right)^2+k_z\left(\frac{l\pi}{L_z}\right)^2\right]\Omega_1-k_x\frac{\partial\varphi}{\partial x}\bigg|_{x=0}=\phi\mu c_t\frac{\partial\Omega_1}{\partial t} \quad \text{..... (3.7)}$$

where $\Omega_1=\mathcal{F}_{c1}\{\varphi\}$ and m is the integer parameter of the FCT-1 space corresponding to the *x*-coordinate.

Thus, the original 3D PDE in space and time has been decomposed into a simple ODE in time only, in which space is no longer involved. Rearranging Eq. 3.7 yields the following non-homogeneous ODE.

$$\frac{\partial\Omega_1}{\partial t}=E_\Phi\Omega_1-F_\Phi \quad \text{..... (3.8)}$$

where

$$E_\Phi=-\left[k_x\left(\frac{m\pi}{L_x}\right)^2+k_y\left(\frac{n\pi}{L_y}\right)^2+k_z\left(\frac{l\pi}{L_z}\right)^2\right]/\left(\phi\mu c_t\right) \quad \text{..... (3.9)}$$

$$F_\Phi=\frac{\partial\varphi}{\partial x}\bigg|_{x=0}/\left(\phi\mu c_t\right) \quad \text{..... (3.10)}$$

If we take time-steps that are sufficiently small to ensure that ΔP (= the maximum pressure difference at any point in the domain) does not exceed a small value, *e.g.*, < 2.5% of P_0, then the quantity μc_t can be considered invariant during this time-step. This allows taking the Laplace transform of Eq. 3.8, which, upon inversion, yields

$$\Omega_{1,t} = e^{E_\Phi \Delta t}\left(\Omega_{1,t-1} - \frac{F_\Phi}{E_\Phi}\right) + \frac{F_\Phi}{E_\Phi} \quad \text{..... (3.11)}$$

Note that t in Eq. 3.11 denotes local time (with $t = 0$ at the beginning of each time step, and $t = \Delta t$ at its end) and Ω_{t-1} denotes the value of Ω at the end of the previous timestep (= the beginning of the new one).

3.3.3 Reconstruction Stage: Neuman Inner-Boundary Conditions

If the PTDM decomposition process stops at the 1D PDE attained after Step D2, then the reconstruction process begins by applying the FD method to obtain the solutions $\varphi(x,n,l,t)$ to Eq. 3.6 at every timestep and at the subdomain in which the x-coordinate is subdivided in the (x+n+l+t) multi-transformed space. Once the $\varphi(x,n,l,t)$ solutions are obtained, the two steps in the reconstruction stage are the following.

$$\omega(x,y,l,t) = \mathcal{F}_{c1}^{-1}\{\varphi\} = \frac{1}{L_y}\left[\varphi(x,0,l,t) + 2\sum_{n=1}^{\infty}\varphi(x,n,l,t)\cos\left(\frac{n\pi y}{L_y}\right)\right] \quad \text{..... (3.12)}$$

$$\psi(x,y,z,t) = \mathcal{F}_{c1}^{-1}\{\omega\} = \frac{1}{L_z}\left[\omega(x,y,0,t) + 2\sum_{l=1}^{\infty}\omega(x,y,l,t)\cos\left(\frac{l\pi z}{L_z}\right)\right] \quad \text{..... (3.13)}$$

Thus, Eq. 3.12 represents the inverse FCT of the 1st kind and restores the *y*-coordinate, Eq. 3.13 restores the *z*-coordinate, and at the end of the reconstruction stage we have solutions at any desirable location in space and time. These solutions are numerical in time and in the *x*-coordinate, and analytical in the *y*- and *z*-coordinates. The solution obtained through this process is referred to as the *PTD-1D solution* because it originates from the solution of the 1D PDE of Eq. 3.6.

If the PTDM decomposition process stops at Step D3, then the reconstruction stage involves three steps. The first is described by

$$\varphi(x,n,l,t)=\mathcal{F}_{c1}^{-1}\{\Omega_1\}=\frac{1}{L_x}\left[\Omega_1(0,n,l,t)+2\sum_{m=1}^{\infty}\Omega_1(m,n,l,t)\cos\left(\frac{m\pi x}{L_x}\right)\right] \quad \text{..... (3.14)}$$

which represents the inverse FCT-1 applied to Eq. 3.11 and restores the *x*-coordinate. The next two steps in the reconstruction process involve the sequential applications of the inverse FCT transforms $\omega(x,y,l,t)=\mathcal{F}_{c1}^{-1}\{\varphi\}$ and $\psi(x,y,z,t)=\mathcal{F}_{c1}^{-1}\{\omega\}$ that are the same as those described by Eqs. 3.12 and 3.13, and restore the *y*- and *z*-coordinates, respectively. The final solution $\psi(x,y,z,t)$ is numerical in time and analytical in the *x*-, *y*- and *z*-coordinates, and the actual pressure *P* corresponding to it can be retrieved from a ψ vs. *P* relationship such as the one in **Fig. 3.2**. It is referred to as the *PTD-0D solution* because it originates from the inversion of the zero-dimensional Eq. 3.11.

3.3.4 Decomposition Stage: Dirichlet Inner-Boundary Conditions

For Dirichlet conditions (constant or time-variable pressure) at $x = 0$, the process up to Step D2 of the Decomposition Stage that has already been described remains the same. However, the FCT-1 cannot be used because it applies to cases when both boundaries are of the Neuman type. Instead, because of the presence of one Dirichlet boundary at $x = 0$, the FCT of the 2nd kind (FCT-2) needs to be involved (see **Appendix A**).

3.3.4.1 Step D3: Second Option - The Third FCT of the Gas Flow Equation in the x-Direction

Taking the FCT-2 of Eq. 3.6 along the *x*-axis (see **Appendix A**), and considering $Q_{x=0} = 0$ and applying $\xi_{x=L_x} = \xi_r$, we obtain the following ODE:

$$-\left[k_x\left(\frac{(2m-1)\pi}{2L_x}\right)^2 + k_y\left(\frac{n\pi}{L_y}\right)^2 + k_z\left(\frac{l\pi}{L_z}\right)^2\right]\Omega_2 = \phi\mu c_t \frac{\partial \Omega_2}{\partial t} \quad \text{..... (3.15)}$$

where $\Omega_2 = \mathcal{F}_{c2}\{\varphi\}$ and m is the integer parameter of the FCT-2 space corresponding to the *x*-coordinate.

Rearranging Eq. 3.15 yields the following non-homogeneous ODE:

$$\frac{\partial \Omega_2}{\partial t} = E_\Phi \Omega_2 \quad \text{..... (3.16)}$$

where

$$E_\Phi = -\left[k_x\left(\frac{(2m-1)\pi}{2\,L_x}\right)^2 + k_y\left(\frac{n\pi}{L_y}\right)^2 + k_z\left(\frac{l\pi}{L_z}\right)^2\right] / \left(\phi\mu c_t\right) \quad \text{..... (3.17)}$$

Eq. 3.16 can be solved by the FD method in time, or by using Laplace transforms within each Δt (as has already been discussed previously). The Laplace transform of Eq. 3.16 leads to the simple algebraic equation

$$s\bar{\Omega}_2 - \Omega_2\left(t=0\right) = E_\Phi \bar{\Omega}_2 \quad \text{..... (3.18)}$$

where $\bar{\Omega}_2 = \mathcal{L}\left\{\Omega_2\right\}$, and $\mathcal{L}\{\}$ represents the Laplace transform of the quantity within the brackets. Because the timestep is small, $\phi\mu c_t$ can be assumed to be constant as long as the pressure changes during it are very small ($\Delta P < 2.5\% P_0$). Then, within this timestep, inversion of $\bar{\Omega}_2$ yields the following solution:

$$\Omega_{2,t_j} = \Omega_{2,t_{j-1}} e^{E_\Phi \Delta t} \quad \text{..... (3.19)}$$

where *j* and *j-1* denote the current and previous the timestep.

3.3.5 Reconstruction Stage: Dirichlet Inner-Boundary Conditions

If Step D3 in the Decomposition Stage is as described by Eq. 3.15, then application of the inverse FCT-2 (see **Appendix A**) in the first step of the Reconstruction Stage restores the *x*-coordinate and results in the following solution in the (x+n+l+t) multi-transformed space:

$$\varphi\left(x,n,l,t\right) = \mathcal{F}_{c2}^{-1}\left\{\Omega_2\right\} = \frac{2}{L_x}\sum_{m=1}^{\infty}\Omega_2\left(m,n,l,t\right)\cos\left(\frac{\left(2m-1\right)\pi x}{2L_x}\right) \quad \text{..... (3.20)}$$

The next two steps in the reconstruction process involve the sequential applications of the inverse FCT-1 transforms $\omega\left(x,y,l,t\right) = \mathcal{F}_{c1}^{-1}\left\{\varphi\right\}$ and $\psi\left(x,y,z,t\right) = \mathcal{F}_{c1}^{-1}\left\{\omega\right\}$. These are the same as those described by Eqs. 3.12 and 3.13, and restore the *y*- and *z*-coordinates,

respectively. For the same reasons discussed earlier, this ψ solution of the pseudo-pressure is referred to also as the *PTD-0D solution*, and provides the corresponding *P* solution.

3.3.5.1 Application to "Boundary" Stencils

These are stencils associated either with the end HFs of horizontal wells (*i.e.*, the first and last HFs along a horizontal well, in which case $L_x \to \infty$) or with the outermost horizontal wells in a system of parallel horizontal wells (in which case $L_y \to \infty$). The solutions presented thus far apply unchanged if the PTDM code (which is a very short and efficient code, given the need for limited inputs) is written in a general manner that allows the user the option of using double or quad precision variables. Selecting the option of quad precision variables (which in FORTRAN95 provides 32 decimal place accuracy and a maximum value of $\pm 1.1897 \times 10^{4932}$), in addition to (a) a very large value for L_y and/or (b) a very large value for L_x (for use in the PTD-0D equations, or to be discretized in the PTD-1D option) enables the use of the equations described earlier without any modification.

3.4 PTDM Validation and Application

In most of the problems considered, the PTDM results are compared to the FTSim results in an effort to validate the PTDM method and gain confidence in its power and abilities. Comparisons include pressure distributions within the body of the domain, as well as flow rates at the fracture surface at $x = 0$ (for Dirichlet boundaries) or pressures at the same

location for Neuman boundaries. The problems we investigated include (1) fully-penetrating fracture (*i.e.*, covering the entire surface of the domain boundary at $x = 0$) with constant production rate, (2) fully-penetrating fracture with constant pressure at the HF face, (3) fully-penetrating fracture with linearly-declining production rate, (4) fully-penetrating fracture with linearly-declining fracture pressure, and (5) fully-penetrating fracture with constant fracture pressure and heterogeneous matrix properties. In order to evaluate the computational efficiency of the PTDM, the execution times of the computation of the solutions at a certain number of points in the domain have been recorded and analyzed.

In this section, we provide the results from several verification/validation studies, as well as in some application studies. Both the PTD-1D and the PTD-0D results are presented, and in the verification studies they are compared to those obtained from the FTSim simulations using 3D domains (stencils) subdivided in 220,000 elements. The dimensions of the simulated stencil, as well as all the system relevant properties and conditions, are provided in **Table 3.1** and show the limited data inputs needed for application of the PTDM. Note that results are presented for a system involving 50 HFs, i.e. $50 \times 8 = 400$ stencils.

Table 3.1 — Inputs in the PTDM and the FTSim simulations*.

Parameter	Value
Initial reservoir pressure P_i	3×10^7 Pa ≈ 4,351 psi
Fracture pressure p_{wf}	6.894757×10^6 Pa ≈ 1,000 psi
Production rate q_c	0.001 kg/s per stencil ≈ 1.8 MMscfd from 400 stencils
Initial reservoir temperature T	65°C = 338.15 K
Gas Composition	100% Methane
Matrix porosity ϕ	0.3
Matrix compressibility c_m	1×10^{-9} Pa^{-1}
Matrix permeability (undisturbed) $k_x = k_y = k_z$	1.5×10^{-19} ≈ 0.15 μD
Half of fracture interval L_x	10 m
Half of fracture length L_y	60 m
Half of fracture height L_z	5 m

* The gas properties are described by the Peng and Robinson (1976) cubic equation of state (EOS)

3.4.1 Validation Cases

3.4.1.1 Case 1: Constant Production Rate q at $x = 0$ (Neuman Boundary)

Fig. 3.4 shows that the PTD-1D results are in very good agreement with the FTSim results, matching perfectly at early times. There is a small deviation near the $x = 0$ boundary that increases at time advances and the pressure in the reservoir becomes more depleted, thus increasing the non-linearity of the μc_t term in Eq. 3.1. A possible reason for this deviation is the fact that discretization in the PTD-1D solution was not sufficiently fine in the vicinity of this location. The average deviation between the PTD-1D and the numerical solutions is 0.58% over the 2-year simulation period, indicating a reliable solution method.

On the other hand, PTD-0D provides solutions that compare well with the FTSim ones only at early times ($t \leq 6$ months), but then the deviations increase rapidly and become unacceptably high. The reason for this behavior is not only the increasing non-linearity as time advances, but also the strong dependence of the μc_t term in Eq. 3.1 not only on pressure but also on the location along the x-coordinate. This dependence on the location cannot be captured by the FCT, hence the unsatisfactory performance. In other words, the initial pressure-based equation that includes P-dependent terms associated with the spatial derivatives cannot be set in the form of Eq. 3.1 if multiple FCTs are to be used without any discretization in a key direction because this inappropriately removes the location dependence of these terms.

The average deviation between the PTD-0D and FTSim is only 0.18% during the first five months of production, and thus this is a perfectly adequate solution not only for estimation of the system behavior during early production but also for history matching and parameter estimation if there is an execution time advantage over the PTD-1D solutions (which is not the case, as will be shown later). Obviously, the use of the PTD-0D solution is not advisable for long-term studies of production from shale gas reservoirs.

The well-flowing pressure from the PTD-1D solution shows a very good agreement with that from FTSim (**Fig. 3.5**) for a long time and begins to exhibit deviations (increasing over time) only at late times when the pressure drop is over 2/3rds of the original pressure. However, these deviations remained small and within an acceptable range for the entire

2-yr production period, and are consistent with the observations in the estimates of the pressure distributions of **Fig. 3.4**. As discussed earlier, it is expected that even better results can be obtained for a finer discretization of the *x*-axis. The increasing deviations at later times occur because the nonlinearity in the μc_t term becomes much more pronounced (increasing rapidly) as pressure decreases.

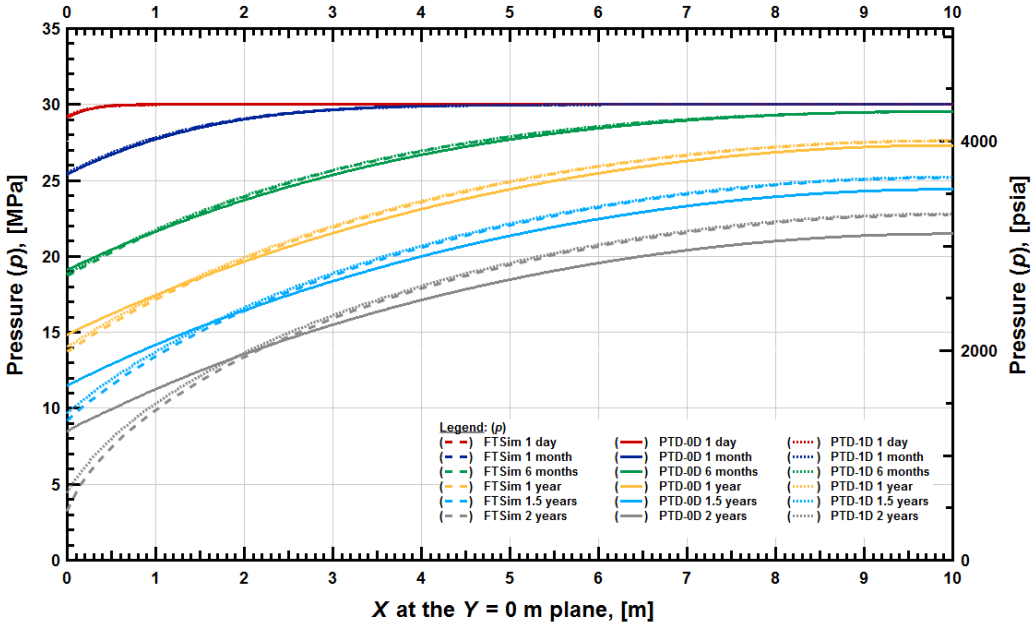

Figure 3.4 — Case 1: Evolution of the pressure distribution over time in the x-direction for constant-rate production: comparison of the FTSim, PTD-1D and PTD-0D solutions.

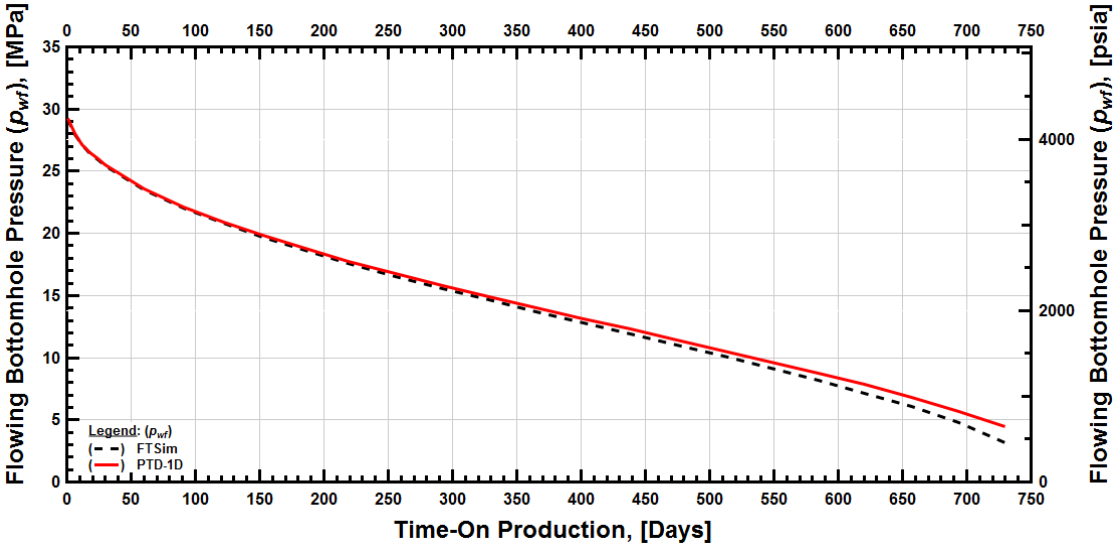

Figure 3.5 — Case 1: Evolution of flowing bottomhole pressure p_{wf} over time for constant-rate production: comparison of the FTSim and PTD-1D solutions.

3.4.1.2 Case 2: Constant Bottomhole Pressure p_{wf} at $x = 0$ (Dirichlet Boundary)

In this case, the PTD-1D results match almost perfectly the FTSim results (**Fig. 3.6**), with their predictions differing by only 0.09% on average. On the other hand, the PTD-0D results are in good agreement with the PTD-1D and the FTSim solutions for $t < 6$ months. For $t > 6$ months, the deviations of the FTSim and PTD-0D predictions increase as time advances for the reasons already explained (*i.e.*, the spatial variation of the μc_t term in Eq. 3.1, which is not considered in the successive FCT transforms), making PTD-0D over-predict the pressure near the fracture ($x = 0$) and under-predict it near the outer boundary ($x = L_x$).

A comparison of the time-variable production rates in Case 2 in **Fig. 3.7** shows an excellent agreement of the FTSim and the PTD-1D predictions. The superiority of the PTD-1D in this and in Case 1 over the PTD-0D approach is due to the spatial discretization along the *x*-direction, which accurately captures the variability of the μc_t term along this crucial coordinate. As expected, the production rate shows a pattern of exponential decline with time, which is typical for constant-pressure production.

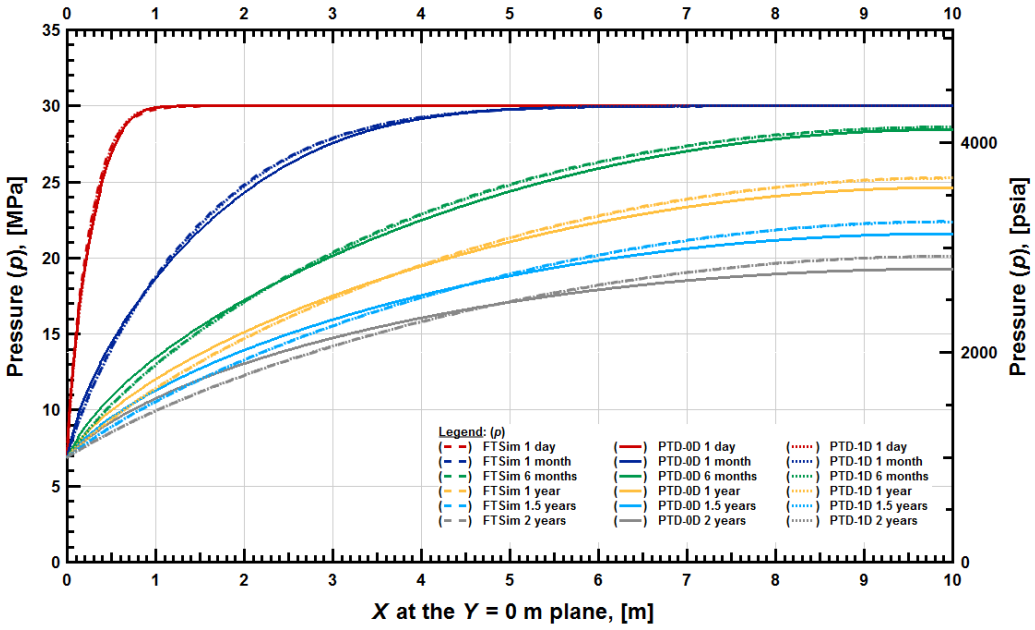

Figure 3.6 — Case 2: Evolution of pressure distribution over time in the x-direction for constant-pressure production: comparison of the FTSim, PTD-1D and PTD-0D solutions.

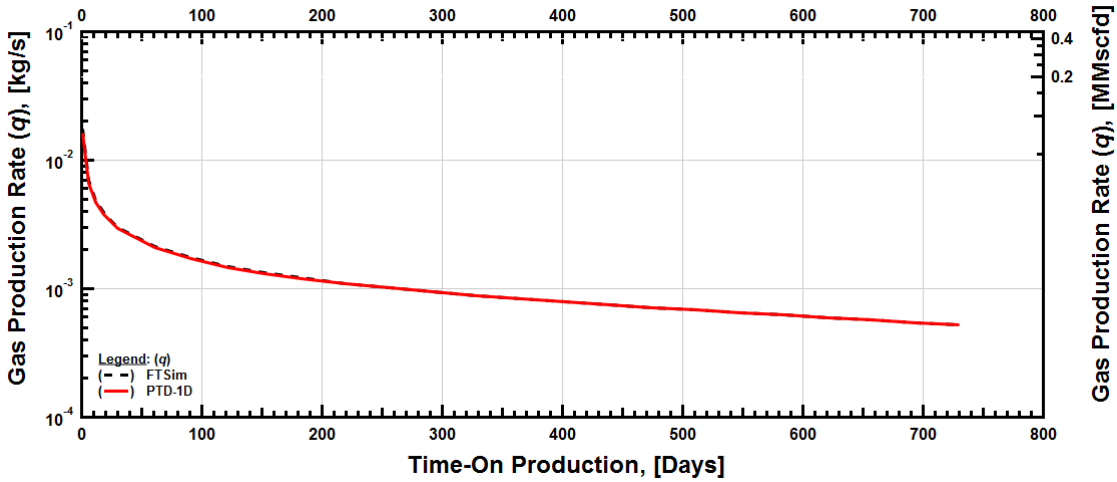

Figure 3.7 — Case 2: Evolution of the gas production rate q over time for constant-pressure production: comparison of the FTSim and PTD-1D solutions.

In both Cases 1 and 2, the PTD-1D results match very well the FTSim ones. This is mainly because both PTD-1D and FTSim considered the spatial discretization in x and the gas properties were calculated separately in each element as functions of the pressure there. Conversely, the application of an FCT in the x-direction in PTD-0D leads to a solution that depends on the μc_t value only at the end of the previous time step, without accounting for spatial variability along x. This assumption may hold true early in the production period when the pressure remains high, but becomes progressively weaker as μc_t increases rapidly with a declining pressure.

The average deviations between the FTSim and the PTD-1D and PTD-0D solutions for 5 months and 2 years of production are shown in **Tables 3.2** and **3.3**, respectively.

Table 3.2 — Average deviations between the FTSim and the PTD-1D and PTD-0D solutions over 5 months of production.

Inner Boundary Condition	PTDM	Avg Percent Deviation from FTSim Result
Neuman (Constant rate)	0D	0.18%
	1D	0.09%
Dirichlet (Constant pressure)	0D	0.97%
	1D	0.10%

Table 3.3 — Average deviations between the FTSim and the PTD-1D and PTD-0D solutions over 2 years of production.

Inner Boundary Condition	PTDM	Avg Percent Deviation from FTSim Result
Neuman (Constant rate)	0D	2.49%
	1D	0.58%
Dirichlet (Constant pressure)	0D	1.92%
	1D	0.09%

3.4.2 Additional Application Cases

In the following cases, we investigate the performance of the PTDM method during gas production with (a) linearly-declining production rate and (b) linearly-declining fracture (boundary) pressure, as well as (c) in heterogeneous domains.

3.4.2.1 Case 3: Linearly-Declining Production Rate q at $x = 0$ (Neuman Boundary)

With a linearly-declining production rate (from q = 0.001 kg/s at t = 0 to q = 0.0005 kg/s at t = 2 years), it is obvious that the pressure depletion in Case 3 is slower than that in Case 1 with a constant q. This becomes evident from the comparison of the spatial distribution of pressures in Case 3 (**Fig. 3.8)** to the results from Case 1 (**Fig. 3.4**). Note that the FTSim simulation results match perfectly the PTD-1D predictions and are not included in **Fig.**

3.8. For reasons already explained, the PTD-0D solutions are accurate for $t < 6$ months, but increasingly deviate from the FTSim and PTD-1D solutions at later times. At early times, p_{wf} in Case 3 is still close to that in Case 1 because the production rate has not declined sufficiently to begin affecting p_{wf} (**Fig. 3.9**). This changes with time and the divergence of p_{wf} in Case 3 and the declining rate leads to higher p_{wf}. The p_{wf} predicted from the FTSim simulation coincides with the PTD-1D solution and is not included in **Fig. 3.9.**

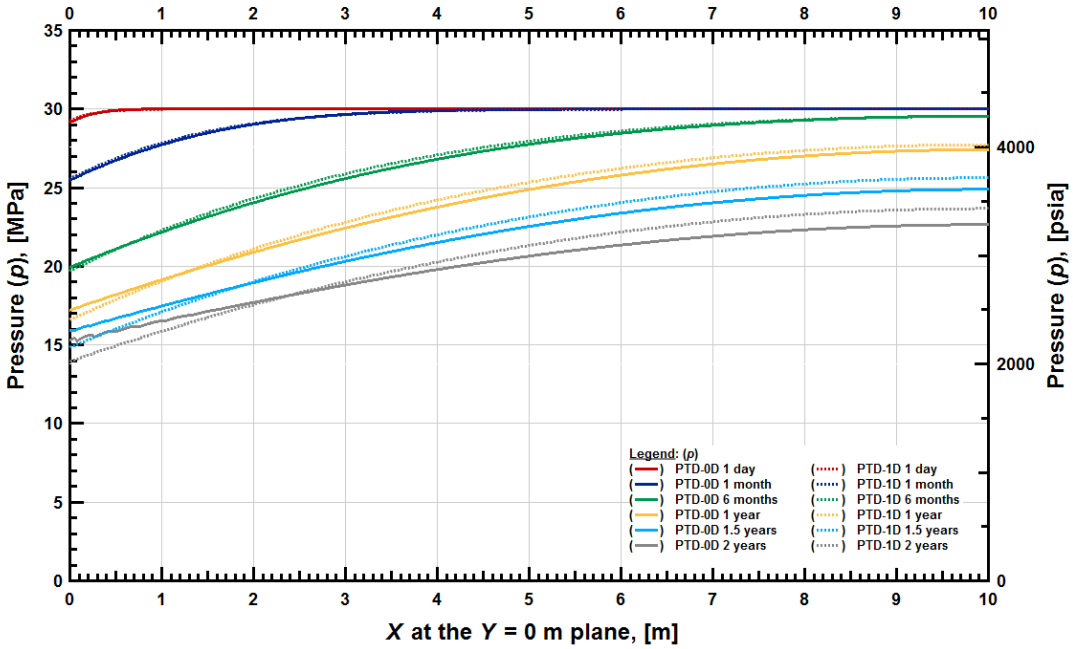

Figure 3.8 — Case 3: Evolution of pressure distribution over time in the x-direction for a linearly declining production rate: comparison of the PTD-1D and PTD-0D solutions.

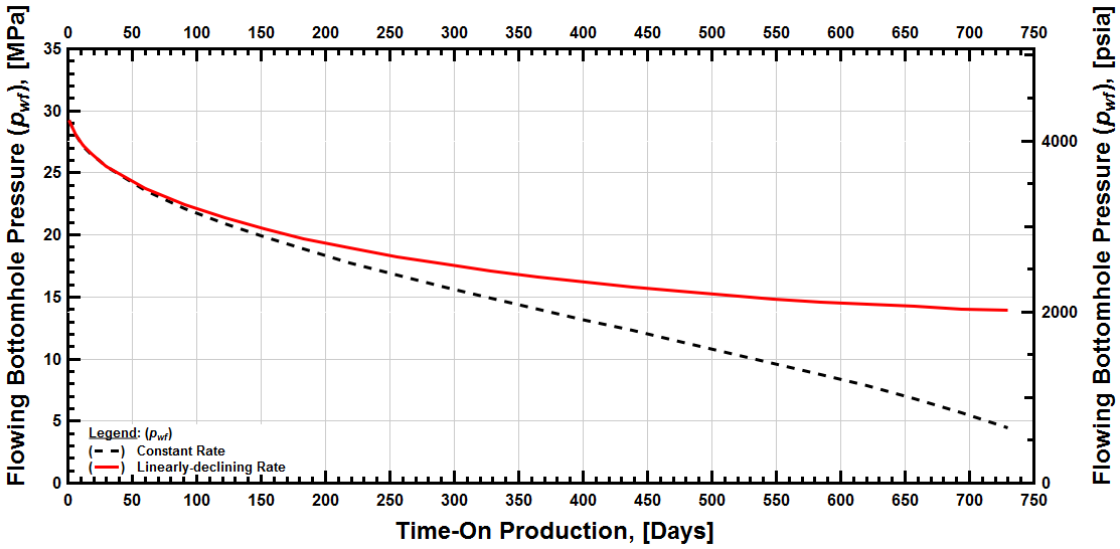

Figure 3.9 — Case 3: Evolution of flowing bottomhole pressure p_{wf} over time for a linearly declining production rate. The flowing bottomhole pressure for a constant rate (= initial) is also shown for comparison.

3.4.2.2 Case 4: Linearly-Declining Bottomhole Pressure p_{wf} at $x = 0$ (Dirichlet Boundary)

In this case, the boundary pressure p_{wf} declines linearly from 1000 psi at $t = 0$ to 500 psi at $t = 2$ years. The corresponding evolutions of the spatial distribution of pressure on the $y = 0$ plane are shown in **Fig. 3.10**, which clearly indicates the declining boundary pressure at the HF as time advances. The PTD-1D results coincide with the FTSim results (which are not included in **Fig. 3.10**). Correct application of the PTD-0D approach requires the use of the primary variable ξ_r in Eq. 3.1 and the application of an FCT of the 2nd kind. The PTD-0D results in **Fig. 3.10** have been obtained with a constant ξ_r, which explains the larger than usual deviations even at relatively earlier times.

Because of the continuously declining pressure at the HF (x = 0) boundary, the gas production rate is expected to be higher than that for the constant p_{wf} of Case 2. **Fig. 3.11** confirms this expectation, with production being practically the same with that for a constant p_{wf} initially (when insufficient time has passed for a significant pressure decline) but increasing continuously as time advances. Note that the logarithmic scale of the gas production rate on the y-axis of **Fig. 3.11** makes it somewhat difficult to easily observe the significant larger production in Case 4.

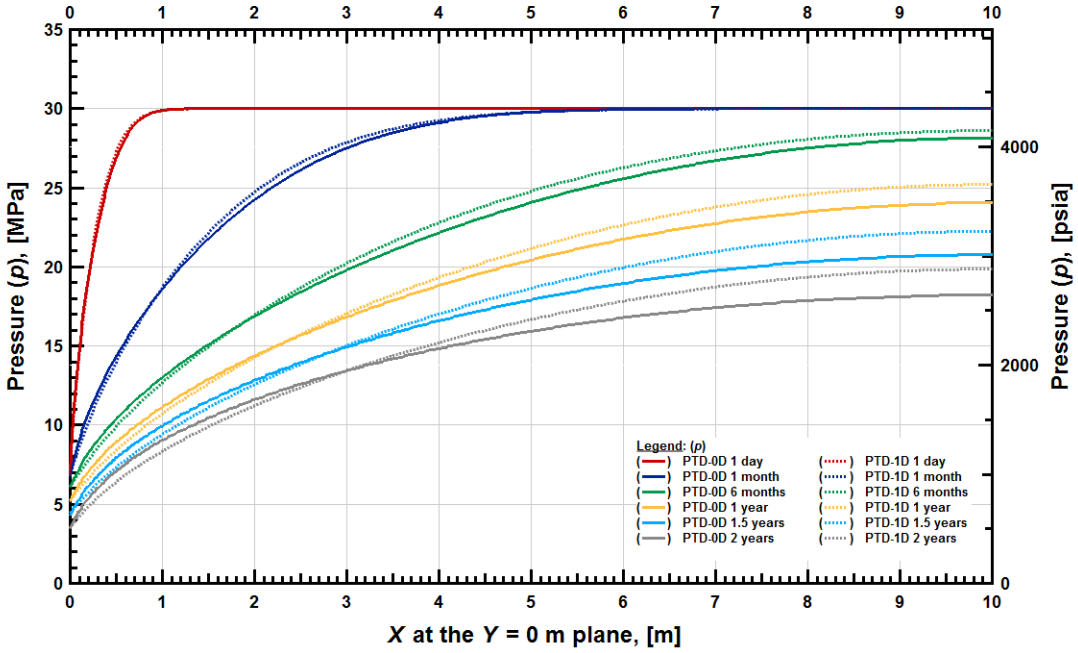

Figure 3.10— Case 4: Evolution of pressure distribution over time in the x-direction for a linearly declining boundary pressure: comparison of the PTD-1D and PTD-0D solutions (the FTSim solutions coincide with the PTD-1D solutions and are not included in this figure).

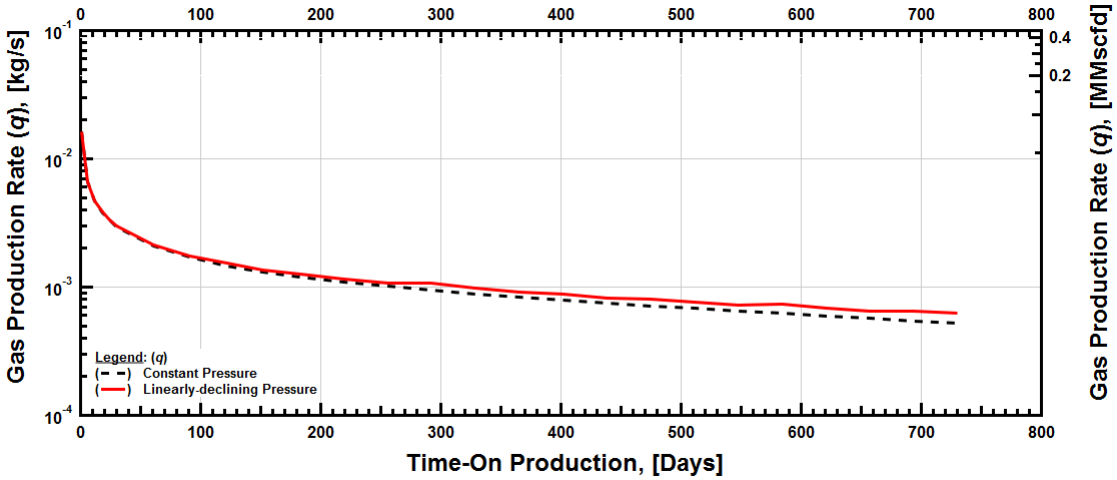

Figure 3.11— Case 4: Evolution of the gas production rate q over time for a linearly-declining boundary pressure production: comparison of the PTD-1D solution with that from Case 2 (the FTSim solution coincides with the PTD-1D solution and is not included in this figure).

3.4.2.3 Case 5: Constant Bottomhole Pressure p_{wf} at x = 0, heterogeneous domain with SRV (Dirichlet Boundary)

In addition to the superiority of performance already identified, the PTD-1D formulation has a major advantage over PTD-0D when subdomain heterogeneity is involved, *e.g.*, in the case of a system involving a stimulated reservoir volume (SRV) subdomain in addition to undisturbed rock matrix. The spatial discretization in the x-dimension allows PTD-1D to easily describe the subdomain heterogeneity, *i.e.*, in the same manner as in the FTSim and any other numerical simulator that involves spatial discretization. The higher permeability and porosity in the SRV subdomain of **Fig. 3.12** are associated with faster pressure depletion than in the adjacent subdomain of undisturbed rock. The results in Case 5 shows that the PTD-1D solution matches almost perfectly the FTSim one over the entire

2-yr-long production period, with the average deviation between the two being 0.46%. The predictions of the production rates from the two methods also coincide, as **Fig. 3.13** clearly shows.

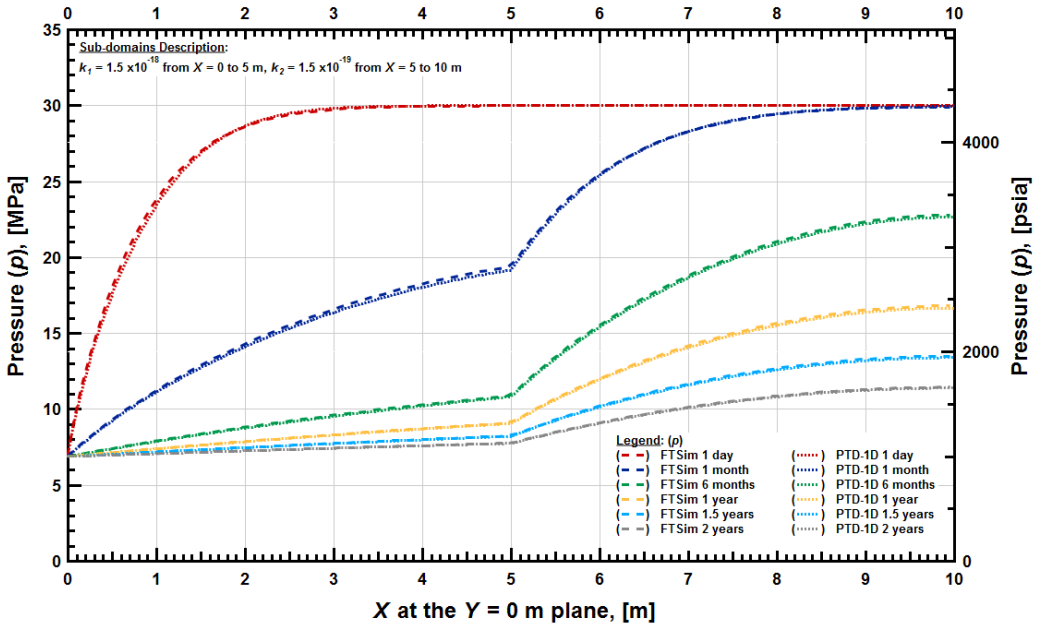

Figure 3.12— Case 5: Evolution of pressure distribution over time in the x-direction in the heterogeneous system with constant-pressure production: comparison of the PTD-1D and FTSim solutions.

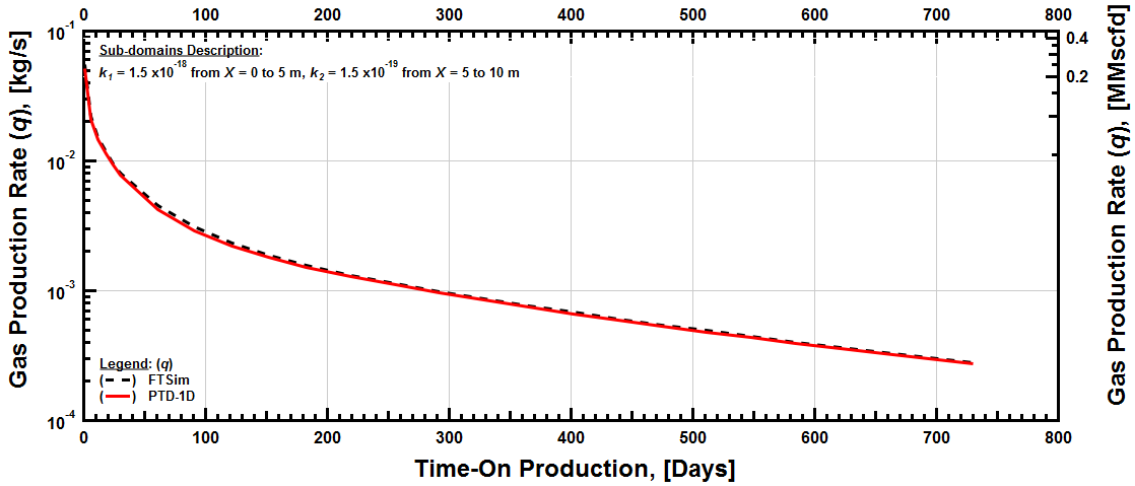

Figure 3.13— Case 5: Evolution of the gas production rate q over time in the x-direction in the heterogeneous system with constant-pressure production: comparison of the PTD-1D and FTSim solutions.

3.5 PTDM Execution Times

In order to investigate the computational efficiency of the PTDM (compared to that of the standard numerical simulation of FTSim) and the relative performance of the PTD-1D and PTD-0D options, we recorded the execution times needed to obtain the pressures at 1,001 locations in the domain after t = 2 years of production, *i.e.*, at a time when the domain pressure is substantially depleted. Remember that PTDM does require time discretization to reach the time t at which results are desired, and the time-step is such that the maximum pressure change ΔP is maintained consistently at a level $\Delta P < 2.5\ P_0$. Thus, the later the time at which an output is required, the longer the execution time.

PTD-0D involves no spatial discretization, allowing pressure predictions at any location (x, y, z) in a homogeneous domain (stencil). We have already discussed its limitations

when subdomain heterogeneity is involved. On the other hand, PTD-1D requires discretization in the *x*-dimension and the corresponding solution needs to be calculated as an array at all individual 1,001 *x*-locations.

Tables 3.4 and **3.5** show the execution times for the PTD-1D and PTD-0D solutions for cases 1 to 5. All computations were performed using the Microsoft Visual Studio Community 2017 (Version 15.9.15) and a platform with Intel® Core™ i7-7700HQ @ 2.80 GHz processors (8CPUs) running serially on Windows 10 Home 64-bit (10.0, Build 18362). **Table 3.4** shows execution times without updating the $\phi\mu c_t$ term in Eq. 3.1 during a timestep (which remains constant at its initial value during the PTDM computations). **Table 3.5** shows the execution times when the term $\phi\mu c_t$ is continuously updated at each timestep by iterating until convergence to a desired level is reached.

The results in **Tables 3.4** and **3.5** confirm the superiority of the PTD-1D over the PTD-0D option in terms of computational efficiency, in addition to the other advantages already discussed (superior accuracy and applicability to heterogeneous domains). PTD-0D requires 1 to 2 orders of magnitude longer execution times the PTD-1D because the additional computations of the inverse FCTs can be quite time consuming. The iterations to update the $\phi\mu c_t$ significantly increase (at least double) the execution times, but, remarkably, without improving perceptibly the accuracy of the solutions (as the iterated and non-iterated solutions differ by less than 0.2 %).

For reference, in Case 2 the computations to obtain the FTSim numerical solutions of the 220,000-element model after 20 timesteps required a computation time of 1,998 sec when running the simulator in a parallel (Open MP) mode using 20 processors on a cluster of 9,632 cores running on a Linux (CentOS 7) system. At the end of the 20 timesteps (beginning with a Δt = 1 sec), a production period of less than 2 sec was covered in this case because the drastic pressure differential at the HF boundary at t = 0 create very steep solution surfaces that are difficult to resolve and require very short timesteps, forcing Δt cutbacks. When Case 1 was solved on the cluster with the same number of processors, 2,133 sec were required and covered a production period of 12.1 days because this is a much easier (numerically) problem. Neither of these two solutions was anywhere close to the 2-year mark of the PTDM solutions. The obvious conclusions from these results are that (a) the PTD-1D can be orders or magnitude faster than a corresponding numerical 3D solution for the same problem (even its serial solution is at least 2-3 orders of magnitude faster than a parallel solution on a cluster), (b) PTD-1D is at least 1-2 orders faster than PTD-0D, and the latter run serially is still at least an order of magnitude faster than a parallel FTSim solution and (c) there is no benefit in attempting to iterate on the nonlinear terms in the PTDM solutions.

Table 3.4 — Execution Times for PTDM over 2 years of production (no iteration within each timestep).

Execution time (sec) of 1001 locations		PTD-0D	PTD-1D
Case 1	Constant rate	158.295	1.978
Case 3	Linearly-declining rate	132.117	1.539
Case 2	Constant pressure	13.558	3.523
Case 4	Linearly-declining pressure	51.694	29.794
Case 5	Constant pressure with sub-domains	N/A	4.190

Table 3.5 — Execution Times for PTDM over 2 years of production (iterations to convergence within each timestep).

Execution time (sec) of 1001 locations		PTD-0D	PTD-1D
Case 1	Constant rate	860.262	3.929
Case 3	Linearly-declining rate	583.224	2.471
Case 2	Constant pressure	21.624	8.552
Case 4	Linearly-declining pressure	93.673	80.500
Case 5	Constant pressure with sub-domains	N/A	8.825

3.6 PTDM Summary

The Partial Transformational Decomposition Method (PTDM) is a hybrid approach that provides solutions to the non-linear problem of gas production in fractured shale gas reservoirs that are numerical in space and analytical (or a combination of analytical and numerical) in space. The method begins by formulating the diffusivity PDE of gas flow in terms of a pseudo-pressure based primary variable, which removes the non-linearity associated with the spatial derivatives and transfers all non-linearities (caused by the high

compressibility of gases) to the time derivative. Successive Finite Cosine Transforms (FCTs) are then applied to the reformulated PDE in the 3D domain of the stencil of these simulations, leading to the elimination of the corresponding dimensions.

If two levels of FCTs are applied, the initial 3D PDE in space and time is transformed into a 1D PDE in the x-direction and time that is solved by means of a Finite Difference method in the multi-transformed space. This is the basis of the PTD-1D option of PTDM. If three levels of FCTs are applied, the initial 3D PDE is transformed into a simple ODE in time only, which is the basis for the PTD-0D option and is solved by means of Laplace transforms. Both PTD-1D and PTD-0D require time discretization, and the use of Laplace transforms are limited to local time subdivisions, *i.e.*, each timestep. The PTD-1D and PTD-0D solutions at each timestep in their respective multi-transformed spaces are then inverted through inverse FCTs to yield solutions at any point in time and the 3D space. These solutions are either fully analytical in space (in the case of PTD-0D) or analytical in 2D and numerical in the x-coordinate (in the case of PTD-1D).

In the case of PTD-1D, the 3D discretization required by numerical models is replaced by discretization along a single coordinate, yielding only a limited number of equations that are orders of magnitude fewer than those in a standard 3D numerical simulation. The inverse FCTs in both the PTD-1D and PTD-0D involve considerable computational effort, but this is still dwarfed (again, by orders of magnitude) compared to the work required for

the solution of the matrices in the high-definition 3D numerical simulations needed to accurately describe the behavior of these ultra-low permeability shale gas reservoirs.

Thus, PTDM offers significant advantages over conventional 3D simulators. It requires either minimal discretization (along a single coordinate) or no discretization at all, and provides fast solutions at any point in the 3D space and time. This approach requires limited input data and has computer memory storage requirements that are minuscule compared to those required for 3D numerical solutions using conventional simulators, with execution speeds that are orders of magnitude faster. The elimination of spatial discretization also saves time and effort that is required to create a 3D grid system (a tedious complicate process that involve a lot of inputs and personal expertise). Note that the computational process for the inverse FCTs is particularly well suited for parallel computing if so desired, although this is not generally needed because serial computing can provide predictions at thousands of locations in a 3D domain in as little as fractions of a second.

Of the two PTDM versions, PTD-1D appears to be by far the superior option; it is 1-2 orders of magnitude faster than PTD-0D (and the latter is still orders of magnitude faster than a standard numerical solution), it offers superior accuracy because it provides spatial dependence of the non-linear terms in the flow equation over long production periods, and allows the consideration of heterogeneous subdomains (such as SRVs). Thus, in the presence of the more powerful PTD-1D, the applicability of the PTD-0D solution is

expected to be limited to cases where the early behavior of a multi-fractured shale gas system is investigated and there is no desire for space discretization.

The speed and efficiency of the PTDM method makes it particularly appealing for early investigations of the production potential of shale gas resources before the development of the reservoir, for the analysis of pressure interference in multi-fractured parallel horizontal wells, and for the parameter identification in such systems by means of history matching using (preferably early, especially in the case of PTD-0D) production data. Note that significant effort is in progress to enhance the theoretical basis of PTDM and expand its applicability to 3D systems with complex domains with significant heterogeneities.

CHAPTER IV

SUMMARY, CONCLUSIONS, AND RECOMMENDATIONS FOR FUTURE WORK

4.1 Summary

We developed an advanced TDM-based solution to the problem of three-dimensional oil flow through, and production from, a multi-fractured shale oil reservoir based on the TDM of Moridis (1995). The method includes two stages. In the decomposition stage, TDM eliminates time and space by using LT and multiple FCTs, respectively, leading to either a simple 1D analytical solution or a trivial algebraic solution in the multi-transformed space. In the reconstruction stage, successive inversions of the TDM solutions yield fast solutions applicable to any point in space and time. These solutions are analytical in space and semi-analytical in time, as they involve numerical inversions of the Laplace-space solutions. A set of TDM solutions was derived, reflecting different boundary conditions and the number of dimensions eliminated by the FCTs: the TD-0D involved elimination of all three dimensions, and TD-1D elimination of only two. The TDM solutions were coded in FORTRAN95 and were validated against results from the FTSim numerical simulator. Both the TD-0D and the TD-1D solutions were shown to be in excellent agreement with the FTSim results regardless of the choice of the method (StA or DHM) for the numerical inversion of the LT-space solutions. However, the DHM was shown to be superior to StA in problems involving steep solution fronts, *e.g.*, in the case of step-wise boundary pressure changes over time (see **Appendix C**).

We also developed the PTDM-based solution to the problem of three-dimensional gas flow through, and production from, a multi-fractured shale gas reservoir. PTDM is a hybrid numerical-analytical method that retains time-discretization (as dictated by the strongly non-linear behavior of the gas) but reduces or eliminates spatial discretization. Like TDM, PTDM involves two stages. In the decomposition stage, application of multiple FCTs leads to either a simple ODE in time or a 1D PDE in space and time in multi-transformed spaces. The reconstruction stage involves successive applications of inverse FCTs to restore the dimensionality of the system, and either standard FD time discretization or application of localized Laplace transforms to yield analytical solutions within each time step. The time steps are sufficiently short to ensure that the non-linear terms remain practically constant during each time step, and this is achieved by limiting the maximum pressure change ΔP between successive timesteps to < 2.5% of the initial P_0. The PTDM solutions are analytical or numerical in space, and semi-analytical or numerical in time. A set of PTDM solutions was derived, reflecting different boundary conditions and the number of dimensions eliminated by the FCTs: the PTD-0D involved elimination of all three dimensions, and PTD-1D elimination of only two. In essence, the advantage of PTD-1D is that it reduces the 3D PDE of gas flow to an 1D PDE. The PTDM solutions were coded in FORTRAN95 and were validated against results from the FTSim numerical simulator. The PTD-1D solutions were also shown to be in very good agreement with the FTSim results (often coinciding with them), but the PTD-0D solutions were sufficiently accurate only at early times (t < 6 months).

The superiority of the TD-1D over the TD-0D method, as well as that of PTD-1D over the PTD-0D, were indicated not only by their generally higher accuracy but also by their significantly higher computational efficiency, as demonstrated by the execution times. The TD-0D and the PTD-0D methods require 1 to 2 orders of magnitude longer execution times than the TD-1D and the PTD-1D, respectively, because of the additional computations for the inversion of the FCT of the 3rd dimension was shown to converge slowly and, thus, to be quite time consuming.

4.2 Conclusions

We derived the following conclusions from this work:

1. TDM and PTDM are applicable to the problems of three-dimensional single-phase oil and a single-phase gas flow in/through the multi-fractured horizontal well system, respectively. The validation results show that both TD-1D and TD-0D yield solutions that are in excellent agreement with those from a numerical simulator. The PTD-1D results are in very good agreement (and often coincide) with the numerical simulation solutions; the PTD-0D results are also in very good agreement with the numerical predictions at early times (t < 6 months), but they begin to show progressively larger deviations for longer times.

2. Both TDM and PTDM can handle various production and system conditions such as (a) time-variable production rate or time-variable bottomhole pressure, (b) fully

penetrating fracture or partially penetrating fracture and (c) heterogeneous sub-domains.

3. In TDM, the use of the more complex and computationally DHM for the inversion of the LT-space solutions does not offer any advantages over the much simpler StA. However, the superiority of the DHM in the inversion of steep solutions makes it the preferred option when sharp changes in the time-dependence of the boundaries (such as in the case step-wise changes in bottomhole pressure or production rate) are involved.

4. The elimination or reduction of the spatial discretization in TDM and PTDM results in limited input data and very low computer memory storage requirements that are practically negligible compared to those for 3D numerical solutions from conventional simulators. The elimination or reduction of the time discretization in addition to the elimination or reduction of the spatial discretization drastically reduce the execution time requirements over those for numerical simulators, routinely by orders of magnitude. Finally, the elimination or reduction of spatial discretization drastically reduces the time and effort needed for the creation of the 3D grid system, a tedious and complicated process that involve a lot of inputs and specialized knowledge and expertise.

5. The elimination or reduction of the spatial discretization in TDM and PTDM results in limited input data and very low computer memory storage requirements that are

practically negligible compared to those for 3D numerical solutions from conventional simulators. The elimination or reduction of the time discretization in addition to the elimination or reduction of the spatial discretization drastically reduce the execution time requirements over those for numerical simulators, routinely by orders of magnitude. Finally, the elimination or reduction of spatial discretization drastically reduces the time and effort needed for the creation of the 3D grid system, a tedious and complicated process that involve a lot of inputs and specialized knowledge and expertise.

6. Because of their simplicity, ease of application, low input requirements and speed, TDM and PTDM are particularly useful for the evaluation of *what-if* scenarios and identification of the factors, conditions and properties that dominate the production behavior of shale reservoirs, and to provide indications of their production potential before the onset, or at the early stages, of full production operations (when limited data are available on the reservoir and its properties). Thus, TDM can provide a large number of production estimates (a task much more difficult, if not impossible, for large conventional simulators involving very large numbers of elements) to define the envelope of possible system performance, and offers the additional benefit of being able to describe processes and phenomena that can only be captured at spatial scales (as low as at the mm-level) that are beyond the capabilities of most numerical simulators, and which may have a significant impact on production.

7. TDM and PTDM are very useful tools for the analysis of pressure interference in multi-fractured ultra-low permeability reservoirs serviced by parallel horizontal wells. Another very significant potential application of TDM and PTDM is in history matching and reservoir parameter identification, which is a difficult, cumbersome and lengthy process in full 3D studies of numerical simulators involving large numbers of elements and covering long production periods. The large number of computations needed for this process can be conducted very effectively using the fast TDM and PTDM solutions to provide estimates of the reservoir properties which, if there is a need for further refinement, can be used as starting points in conventional, numerical-based history matching analyses.

4.3 Recommendations for Future Work

The following recommendations for future work are proposed:

1. The current versions of TDM and the PTDM have a limitation in the type of boundary conditions they can handle if multiple diverse conditions exist along a given direction. Thus, in the case of a partially-penetrating fracture, TDM and PTDM can only be applied if the inner-boundary condition involves a time-variable production rate because dP/dx is well defined on the entire surface of the $x = 0$ plane. If a constant or time variable bottomhole pressure is applied to the HF, then it is not possible to obtain a solution with TDM or PTDM because their current stage of development cannot handle the different boundary conditions at $x = 0$: a known P at the partially-

penetrating HF and a known *dP/dt* elsewhere on the $x = 0$ plane. Work is in progress to resolve this issue.

2. The TDM and the PTDM were coded in a computer program written in FORTRAN 95. The code was written in a general way, allowing the use of either double or quad-precision arithmetic through the value of a single input. For problems involving full HF penetration, the very fast execution time does not provide an impetus for improvements in the computational efficiency and reduction of the execution times. The situation is significantly different in the case of partially penetrating HFs because the corresponding computations involve cross products that converge slowly. To address such a challenge, parallelization of the TDM and PTDM codes is the recommended approach because the computational processes for the inverse FCTs and LTs are particularly well suited for parallel computing.

NOMENCLATURE

Variables:

A_F	=	surface area of flow, m^2
c_m	=	pore compressibility, Pa^{-1}
c_o	=	oil compressibility, Pa^{-1}
c_t	=	total compressibility, Pa^{-1}
C_T	=	as defined by Eq. 2.6
$d°$	=	direction (x,y,z)
$\mathcal{F}_{ci}\{\}$	=	denotes the Finite Cosine Transform of the i-th kind (i=1,2) of the quantity within the brackets
$\mathcal{F}_{ci}^{-1}\{\}$	=	denotes the inverse Finite Cosine Transform of the i-th kind (i=1,2) of the quantity within the brackets
g	=	gravitational acceleration, (= 9.806) m/s^2
j	=	timestep index
k	=	intrinsic permeability, m^2
$L_{d°}$	=	total stencil's length in the $d°$-direction, m
l	=	integer FCT parameter associated with the z-coordinate
$\mathcal{L}\{\}$	=	denotes the Laplace transform of the quantity within the brackets

$\mathcal{L}^{-1}\{\}$ = denotes the inverse Laplace transform of the quantity within the brackets

M = gas molecular weight, kg/mol

M_H = number of terms for DeHoog Laplace inversion

m = integer FCT parameter associated with the x-coordinate

N_{HF} = number of hydraulic-fractures

N_s = number of terms for Stehfest Laplace inversion

n = integer FCT parameter associated with the y-coordinate

P,p = pressure, Pa

ΔP = maximum pressure changes in a single timestep Δt, Pa

p_{wf} = bottomhole pressure at HF, Pa

q = production rate, kg/s

Q = production flux, kg/s/m^2

$\mathcal{Q}$ = $\mathcal{L}\{Q\}$

$\dot{\mathcal{Q}}$ = $\mathcal{F}_{c1}\{\mathcal{Q}\}$

$\ddot{\mathcal{Q}}$ = $\mathcal{F}_{c1}\{\dot{\mathcal{Q}}\}$

R = the expansion term of the oil density equation as defined by Eq. 2.2

R_{gas} = gas constant, Pa-m^3/mol/K

s = Laplace space parameter

T = temperature, K or °C

t = time, sec

Δt = timestep, sec

U = Heavyside step function

u_0 = pseudo-pressure factor (= 2, see Eq. 3.2)

x = Cartesian coordinates, m

y = Cartesian coordinates, m

Z = gas compressibility or z-factor

z = Cartesian coordinates, m

Greek Symbols:

β = inversion of oil formation volume factor, STB/RB

λ = as defined by Eq. 2.1

μ = fluid viscosity, Pa-s

ρ = fluid density, kg/m^3

ϕ = porosity, fraction

δ = a deviation from the unity of the expansion term of the oil density equation as defined by Eq. 2.2

Ψ = $\mathcal{L}\{\delta\}$

Θ = $\mathcal{F}_{c1}\{\Psi\}$

Φ = $\mathcal{F}_{c1}\{\Theta\}$

Υ_i = $\mathcal{F}_{ci}\{\Phi\}$ $(i=1,2)$

ξ = pseudo-pressure (as defined by Eq. 3.2)

ψ = dimensionless primary variable based gas pseudo-pressure (as defined by Eq. 3.2)

ω = $\mathcal{F}_{c1}\{\psi\}$

φ = $\mathcal{F}_{c1}\{\omega\}$

Ω_i = $\mathcal{F}_{ci}\{\varphi\}$ $(i=1,2)$

$\overline{\Omega}_i$ = $\mathcal{L}\{\Omega_i\}$ $(i=1,2)$

Subscripts and Superscripts:

-1 = inverse transform

0 = initial conditions

d° = coordinate (= *x*, *y*, or *z)*

F = hydraulic-fracture

r = reference state

STC = standard conditions

wf = flowing well or HF surface

Acronyms and Abbreviations:

AS = Analytical Solution

A/SA = Analytical/Semi-Analytical Solution

DHM = DeHoog Method (DeHoog et al., 1982) for LT inversion

EOS = Equations of State

FCT = Finite Cosine Transformation

FD = Finite Difference

HF = Hydraulic Fracture

HS = Homogeneous Subdomains

IFD = Integral Finite Difference

LHS = Left Hand Side

LIB = Left Infinite Boundary

LT = Laplace Transform

ODE = Ordinary Differential Equation

PDE = Partial Differential Equation

PTDM = Partial Transformational Decomposition Method

RIB = Right Infinite Boundary

SRV = Stimulated Reservoir Volume

StA = Stehfest Algorithm (Stehfest, 1970a;b) for LT inversion

TDM = Transformational Decomposition Method

ULP = Ultra-Low Permeability

REFERENCES

Al-Hussainy, R., Jr., H. R. and Crawford, P. 1966. The Flow of Real Gases Through Porous Media. *J Pet Technol* **18** (05): 624 - 636. SPE-1243-A-PA. https://doi.org/10.2118/1243-A-PA.

Anderson, D.M., M. Nobakht and S. Moghadam, Analysis of Production Data from Fractured Shale Gas Wells. Paper SPE 131787, 2010 SPE Unconventional Gas Conference, Pittsburgh, Pennsylvania, USA. https://doi.org/10.2118/131787-MS.

Bello, R.O. and R.A.Wattenbarger, Rate Transient Analysis in Naturally Fractured Shale Gas Reservoirs. Paper SPE 114591, CIPC/SPE Gas Technology Symposium 2008 Joint Conference, Calgary, Alberta, Canada. https://doi.org/10.2118/114591-MS.

Anantraksakul, N., Moridis, G.J., and T.A. Blasingame, The Partial Transformational Decomposition Method (PTDM) For The Solution Of The Gas Flow Problem In A Hydraulically Fractured Ultra-Low Permeability Reservoir, SPE Paper 199015-MS, Proceedings, paper presented at the SPE Latin American and Caribbean Petroleum Engineering Conference, Bogota, Colombia, 28-30 July 2020.

Blasingame, T. and Jr., B. P. 1993. Semianalytic Solutions for a Well With a Single Finite-Conductivity Vertical Fracture. Presented at the SPE Annual Technical Conference and Exhibition, Houston, Texas, 3-6 October. SPE-26424-MS. https://doi.org/10.2118/26424-MS.

Brown, M., Ozkan, E., Raghavan, R. et al. 2011. Practical Solutions for Pressure-Transient Responses of Fractured Horizontal Wells in Unconventional Shale Reservoirs. *SPE Res Eval & Eng* **14** (06): 663 - 676. SPE-125043-PA. https://doi.org/10.2118/125043-PA.

Cipolla, C.L., E. Lolon, J. Erdle et al., Modeling Well Performance in Shale-Gas Reservoirs. Paper SPE 125532, 2009 SPE/EAGE Reservoir Characterization and Simulation Conference, Abu Dhabi, UAE. https://doi.org/10.2118/125532-MS.

Crump, K. S. 1976. Numerical Inversion of Laplace Transforms Using a Fourier Series Approximation. J. ACM 23, 1 (January 1976), 89–96. https://doi.org/10.1145/321921.321931.

DeHoog, F. R., J. H. Knight, and A.N. Stokes, An improved method for numerical inversion of Laplace transforms, SIAM J. Sci. Stat. Comput., 3(3), 357-366, 1982.

Freeman, C.M., Study of flow regimes in multiply-fractured horizontal wells in tight gas and shale gas reservoir systems, M.Sc. Thesis, Petroleum Engineering Department, Texas A&M University, 2010.

Freeman, C.M., G.J. Moridis, D. Ilk and T. Blasingame, A numerical study of performance for tight gas and shale gas reservoir systems, Paper SPE 124961, 2009 SPE Annual Technical Conference and Exhibition, New Orleans, Louisiana, October 4-7, 2009.

Freeman, C., Moridis, G., Ilk, D. et al. 2013. A numerical study of performance for tight gas and shale gas reservoir systems. *Journal of Petroleum Science and Engineering*. **108**: 22-39. http://dx.doi.org/10.1016/j.petrol.2013.05.007.

Goode, P. A. and Thambynayagam, R. K. 1987. Pressure Drawdown and Buildup Analysis of Horizontal Wells in Anisotropic Media. *SPE Form Eval* **2** (04): 683 - 697. SPE-14250-PA. https://doi.org/10.2118/14250-PA.

Gringarten, A.C., Unsteady-State Pressure Distributions Created by a Well with a Single Horizontal Fracture, Partial Penetration, or Restricted Entry. Ph.D. Dissertation, Stanford University, Stanford, California, USA, 1971.

Gringarten, A. C., Jr., H. J. and Raghavan, R. 1974. Unsteady-State Pressure Distributions Created by a Well With a Single Infinite-Conductivity Vertical Fracture. *Society of Petroleum Engineers Journal* **14** (04): 347 - 360. SPE-4051-PA. https://doi.org/10.2118/4051-PA.

Mattar, L. 2008. Production Analysis and Forecasting of Shale Gas Reservoirs: Case History-Based Approach. Presented at the SPE Shale Gas Production Conference, Fort Worth, Texas, USA, 16-18 November. SPE-119897-MS. https://doi.org/10.2118/119897-MS.

Medeiros, F., Ozkan, E. and Kazemi, H. 2006. A Semianalytical, Pressure-Transient Model for Horizontal and Multilateral Wells in Composite, Layered, and Compartmentalized Reservoirs. Presented at the SPE Annual Technical Conference and Exhibition, San Antonio, Texas, USA, 24-27 September. SPE-102834-MS. https://doi.org/10.2118/102834-MS.

Miller, M.A., Jenkins, C.D., and Rai, R.R. 2010. Applying Innovative Production Modeling Techniques to Quantify Fracture Characteristics, Reservoir Properties, and Well Performance in Shale Gas Reservoirs. Paper SPE 139097 presented at the SPE Eastern Regional Meeting, Morgantown, West Virginia, USA. https://doi.org/10.2118/139097-MS.

Moridis, G. J., Alternative formulations of the Laplace Transform Boundary Element (LTBE) numerical method for the solution of diffusion-type equations, in Boundary Element Technology VII, pp. 815-833, Computational Mechanics Publications, Boston, and Elsevier Applied Science, New York, 1992. https://doi.org/10.1007/978-94-011-2872-8_55.

Moridis, G.J., The Transformational Decomposition (TD) Method for Compressible Fluid Flow Simulations, SPE Advanced Technology Series, 3(1), 101-110, March 1995 (LBL Report No. 33149).

Moridis, G. J. 2017. High Resolution Investigations of Flow and Thermal Processes During Production from Hydraulically Fractured Ultra-Low Permeability Media. Presented at the SPE Latin America and Caribbean Petroleum Engineering Conference, Buenos Aires, Argentina, 17-19 May. SPE-185512-MS. https://doi.org/10.2118/185512-MS.

Moridis, G.J., N. Anantraksakul and T.A. Blasingame, TDM-based semi-analytical solutions of the 3D problem of oil production from shale reservoirs, SPE Paper 199083-MS, Proceedings, paper presented at the SPE Latin American and Caribbean Petroleum Engineering Conference, Bogota, Colombia, 28-30 July 2020.

Moridis, G. and Freeman, C. 2014. The RealGas and RealGasH2O options of the TOUGH+ code for the simulation of coupled fluid and heat flow in tight/shale gas systems. *Computers & Geosciences*. **65**: 56-71. http://dx.doi.org/10.1016/j.cageo.2013.09.010.

Moridis, G.J. and M. Freeman, User's Manual for the RealGasBrine v1.0 Option of TOUGH+ v1.5: A Code for the Simulation of System Behavior Gas-Bearing Geologic Media, Lawrence Berkeley National Laboratory report LBNL-6870E, February 2016.

Moridis, G.J., and E. J. Kansa, The method of Laplace Transform MultiQuadrics (LTMQ) for the solution of the groundwater flow equation, in Advances in Computer Methods for Partial Differential Equations VII, edited by R. Vichnevetsky, D. Knight, and G. Richter, pp. 539-545, 1992.

Moridis, G.J., and E. J. Kansa, The Laplace Transform MultiQuadrics method: A Highly Accurate Scheme for the Numerical Solution of Linear Partial Differential Equations, Journal of Applied Science & Computations, 1(2), 375-407, 1994 (LBL Report No. 35011).

Moridis, G. and McVay, D. 1995. The Transformational Decomposition (TD) Method for Compressible Fluid Flow Simulations. *SPE Advanced Technology Series* **3** (01): 163 - 172. SPE-25264-PA. https://doi.org/10.2118/25264-PA.

Moridis, G.J., D.A. McVay, and D.L. Reddell, The Laplace Transform Finite Difference (LTFD) Method for the Simulation of Compressible Liquid Flow in Reservoirs, SPE Advanced Technology Series, 2(2), 122-131, 1994 (LBL Report No. 32060).

Moridis, G.J. and K. Pruess, User's Manual of the TOUGH+ Core Code: A General Purpose Simulator of Non-Isothermal Flow and Transport Through Porous and Fractured Media, Lawrence Berkeley National Laboratory report LBNL-6871E, February 2016.

Moridis G.J. and Reagan M.T., Evaluation Of The Effectiveness Of Continuous Gas Displacement For EOR In Hydraulically Fractured Shale Reservoirs, SPE-198999-MS, Latin America and Caribbean Petroleum Engineering Conference, 28-30 July 2020, Bogota, Colombia.

Moridis, G.J., and Reddell, D.L.: 'The Laplace Transform Finite Difference Method for Simulation of Flow through Porous Media in Reservoirs", Water Resources Research, vol. 27, no. 8, pages 1873-1884 August 1991a. https://doi.org/10.1029/91WR01190.

Moridis, G.J., and Reddell, D.L., The Laplace Transform Boundary Element (LTBE) numerical method for the solution of diffusion-type equations, in Boundary Elements XIII, edited by C.A. Brebbia and G. S. Gibson, pp. 83-97, Computational Mechanics Publications and Elsevier Applied Sciences, London, 1991b. https://doi.org/10.1007/978-94-011-3696-9_7.

Moridis, G. J., Y.-S. Wu, and K. Pruess, EOS9nT: A TOUGH2 module for the simulation of flow and solute/colloid transport in the subsurface, Report LBNL-42351, Lawrence Berkeley National Laboratory, Berkeley, Calif., 1999. https://doi.org/10.2172/765127.

Olorode, O., 2011. Numerical Modeling and Analysis of Shale-Gas Reservoir Performance Using Unstructured Grids (M.Sc. thesis). Petroleum Engineering Department, Texas A&M University.

Olorode, O., Freeman, C. M., Moridis, G. et al. 2013. High-Resolution Numerical Modeling of Complex and Irregular Fracture Patterns in Shale-Gas Reservoirs and Tight Gas Reservoirs. *SPE Res Eval & Eng* **16** (04): 443 - 455. SPE-152482-PA. https://doi.org/10.2118/152482-PA.

Peng, D. and Robinson, D. B. 1976. A New Two-Constant Equation of State. *Ind. Eng. Chem. Fund.* **15** (1): 59-64. https://doi.org/10.1021/i160057a011.

Reagan, M.T., G.J. Moridis, N.D. Keen, and J.N. Johnson, Numerical Simulation of the Environmental Impact of Hydraulic Fracturing of Tight/Shale Gas Reservoirs on Near-Surface Groundwater: Background, Base Cases, Shallow Reservoirs, Short-Term Gas, and Water Transport, Water Resources Research, 51(4), 2543-2573, 2015. https://doi.org/10.1002/2014WR016086.

Reagan, M., Moridis, G., Keen, N. et al. 2019. Transport and Fate of Natural Gas and Brine Escaping from a Hydrocarbon Reservoir Through a Failed Deepwater Well in the Oceanic Subsurface of the Gulf of Mexico. *Transport in Porous Media* **127** (2): 459-480. http://dx.doi.org/10.1007/s11242-018-1207-y.

Sarkar, P., G.J. Moridis and T.A. Blasingame, Evaluation Of The Performance Of Thermal EOR Processes In Fractured Shale Oil Formations, SPE-198981-MS, Latin America and Caribbean Petroleum Engineering Conference, 28-30 July 2020, Bogota, Colombia.

Stalgorova, K. and Mattar, L. 2013. Analytical Model for Unconventional Multifractured Composite Systems. *SPE Res Eval & Eng* **16** (03): 246 - 256. SPE-162516-PA. https://doi.org/10.2118/162516-PA.

Stehfest, H., Algorithm 368, Numerical inversion of Laplace transforms, J, ACM, 13(1), 47-49, 1970a.

Stehfest, H., Algorithm 368, Remark on algorithm 368 [D5], Numerical inversion of Laplace transforms, J. ACM, 13(1), 56, 1970b.

Sudicky EA (1989) The Laplace transform Galerkin technique: a time-continuous finite element theory and application to mass transport in groundwater. Water Resources Research, vol. 25: 1833–1846

Thambynayagam, R. K. M. (2011). The Diffusion Handbook: Applied Solutions for Engineers . Chap. 2, 18-25 . China: McGraw Hill Professional

U.S. Energy Information Administration (EIA), 2019. Annual Energy Review. /http://www.eia.gov/totalenergy/data/annual/

APPENDIX A

THE TYPES OF FINITE COSINE TRANSFORM AND THEIR PROPERTIES

This appendix A introduces the Finite Cosine Transformations (FCTs) and their applications in the development of the both the Transformational Decomposition Method (TDM) and the Partial Transformational Decomposition Method (PTDM).

A.1 Definition of FCTs and Their Properties

In this study, two kinds of finite cosine transformations are considered. The FCT of the 1st kind (hereafter referred to as FCT-1) is used to handle Neuman inner-boundary conditions at both $x = 0$ and $x = L_x$, where $\partial\psi / \partial x$ is well-defined at these locations as a function of time only. FCT-1 is defined by the following equation:

$$\mathcal{F}_{c1}(\psi) = \theta(m) = \int_0^{L_x} \psi \cos\left(\frac{m\pi}{L_x}\, x\right) dx \quad \text{(A-1)}$$

where m is the FCT-1 transform variable in x-direction and ψ is defined on $[0, L_x]$

The FCT-1 of the second derivative is described by the following equation.

$$\mathcal{F}_{c1}\left(\frac{\partial^2\psi}{\partial x^2}\right) = -\left(\frac{m\pi}{L_x}\right)^2 \theta - \left.\frac{\partial\psi}{\partial x}\right|_{x=0} + (-1)^m \left.\frac{\partial\psi}{\partial x}\right|_{x=L_x} \quad \text{(A-2)}$$

With this transformation, the problem of a 1D second-order partial differential equation (PDE) is simplified to a simple algebraic equation. The solution in space (*i.e.*, at any x) is obtained by inverting the solution of Eq. A-1 using the following equation:

$$\psi = \mathcal{F}_{c1}^{-1}(\theta) = \frac{1}{L_x}\left[\theta(0) + 2\sum_{m=1}^{\infty}\theta(m)\cos\left(\frac{m\pi x_l}{L_x}\right)\right] \quad \text{(A-3)}$$

The FCT of the 2nd kind (hereafter referred to as FCT-2) is applicable to mixed Neuman/Dirichlet boundary conditions across the length of one of the dimensions of the domain. It applies to problems where $\partial\psi/\partial x$ is well-defined as a function of time only at $x = 0$ and ψ is well-defined as a function of time at $x = L_x$ (Thambynayagam, 2011). To reverse the location of the two boundaries, we define $x' = L_x - x$ and then FCT-2 is defined by the following equation:

$$\mathcal{F}_{c2}(\psi) = \theta'(m) = \int_0^{L_x}\psi\cos\left(\frac{(2m-1)\pi}{2L_x}\,x'\right)dx' \quad \text{(A-4)}$$

where m is the FCT-2 transform variable in *x*-direction and ψ is defined on $[0, L_x]$

The FCT-2 transformation of the second derivative is then

$$\mathcal{F}_{c2}\left(\frac{\partial^2\psi}{\partial x'^2}\right) = -\left(\frac{(2m-1)\pi}{2L_x}\right)^2\theta' - \left.\frac{\partial\psi}{\partial x'}\right|_{x'=0} - (-1)^m\left(\frac{(2m-1)\pi}{2L_x}\right)\psi\Big|_{x'=L_x} \quad \text{(A-5)}$$

With this transformation, the problem with second-order partial differential equation (PDE) is simplified to just an algebraic equation. Inversion of FCT-2 to yield ψ is obtained from the following relationship:

$$\psi = \mathcal{F}_{c2}^{-1}(\theta') = \frac{2}{L_x}\sum_{m=1}^{\infty}\theta'(m)\cos\left(\frac{(2m-1)\pi\,x_l'}{2L_x}\right) \quad \text{(A-6)}$$

More information on the subject can be found in Thambynayagam (2011). Using FCTs and their properties, TDM and PTDM can be developed to solve the problem of gas production from fractured ultra-low permeability (ULP) reservoirs. The following section shows how FCTs are applied in the PTDM development.

A.2 The FCTs of the Boundary Conditions

To deal with the partially-penetrating fracture, the stencil could have been divided into two to four sub-domains, which will result a complex system of equations. However, using the FCT properties allows the problem to be solved within a single domain.

If the fracture at $(x = 0)$ is fully-penetrating, then the production flux (Q) will be constant across the entire y-z cross section. Then, the FCT-1 of the boundary condition can be calculated from the following equations:

$$\hat{Q} = \mathcal{F}_{c1,z}(Q) = \begin{cases} L_z Q & \text{when } l = 0 \\ 0 & \text{when } l > 0 \end{cases} \quad \text{.....(A-7)}$$

$$\hat{\hat{Q}} = \mathcal{F}_{c1,y}(\hat{Q}) = \begin{cases} L_y \hat{Q} & \text{when } n = 0 \\ 0 & \text{when } n > 0 \end{cases} \quad \text{.....(A-8)}$$

If the fracture at $(x = 0)$ is partially-penetrating, extending from $y = 0$ to Y_F and from $z = 0$ to Z_F, then the production flux (Q) will be constant in the Y_F - Z_F section. The FCT-1 of the boundary condition is obtained from the following equations:

$$\hat{Q} = \mathcal{F}_{c1,z}(Q) = \begin{cases} Z_F\, Q & \text{when } l = 0 \\ \dfrac{L_z}{l\pi} Q \left[\sin \dfrac{l\pi Z_F}{L_z} \right] & \text{when } l > 0 \end{cases} \quad \text{.....(A-9)}$$

$$\hat{\hat{Q}} = \mathcal{F}_{c1,y}\left(\hat{Q}\right) = \begin{cases} Y_F\, \hat{Q} & \text{when } n = 0 \\ \dfrac{L_y}{n\pi} \hat{Q} \left[\sin \dfrac{n\pi Y_F}{L_y} \right] & \text{when } n > 0 \end{cases} \quad \text{.....(A-10)}$$

A.3 The FCTs of the Initial Conditions

The initial pressure is assumed constant in the entire system represented by a stencil. When the transformations eliminate two coordinates with uniformly Neuman boundary conditions, the FCT-1 of the initial conditions is provided by the following equation:

$$\varphi_i = \mathcal{F}_{c1,y}\left(\mathcal{F}_{c1,z}\left(\psi_i\right)\right) = \begin{cases} L_y\, L_z\, \psi_i & \text{when } n = 0 \text{ and } l = 0 \\ 0 & \text{others} \end{cases} \quad \text{.....(A-11)}$$

When the transformations eliminate three coordinates with uniformly Neuman boundary conditions, the FCT of the initial conditions is provided by the following equation:

$$\Omega_i = \mathcal{F}_{c1,x}\left(\mathcal{F}_{c1,y}\left(\mathcal{F}_{c1,z}\left(\psi_i\right)\right)\right) = \begin{cases} L_x\, L_y\, L_z\, \psi_i & \text{when } m = 0,\ n = 0 \text{ and } l = 0 \\ 0 & \text{others} \end{cases} \quad \text{.....(A-12)}$$

When the transformations eliminate three coordinates and one of the boundaries represents a Dirichlet (constant pressure) condition, the FCT of the initial conditions is given by

$$\Omega_i = \mathcal{F}_{c2,x}\left(\mathcal{F}_{c1,y}\left(\mathcal{F}_{c1,z}\left(\psi_i\right)\right)\right) = \begin{cases} \dfrac{2L_x\left(-1\right)^{m-1}}{\left(2m-1\right)\pi} L_y\, L_z\, \psi_i & \text{when } n = 0 \text{ and } l = 0 \\ 0 & \text{others} \end{cases} \quad \text{.....(A-13)}$$

A.4 FCT Inversions

When the transformations eliminate two coordinates with uniformly Neuman boundary conditions, the inversion of the FCT yields the original primary variable ψ through the application of the following equation:

$$\psi(y,z)=\frac{1}{L_yL_z}\left[\begin{array}{l}\varphi(0,0)+2\sum_{l=1}^{\infty}\varphi(0,l)\cos\left(\frac{l\pi z}{L_z}\right)+2\sum_{n=1}^{\infty}\varphi(n,0)\cos\left(\frac{n\pi y}{L_y}\right)\\+4\sum_{l=1}^{\infty}\sum_{n=1}^{\infty}\varphi(n,l)\cos\left(\frac{l\pi z}{L_z}\right)\cos\left(\frac{n\pi y}{L_y}\right)\end{array}\right] \quad \text{.....(A-14)}$$

When the transformations eliminate three coordinates with uniformly Neuman boundary conditions, the inversion of the FCTs described below yields the original primary variable ψ:

$$\psi(x,y,z)=\frac{1}{L_xL_yL_z}\left[\begin{array}{l}\Omega(0,0,0)+2\sum_{l=1}^{\infty}\Omega(0,0,l)\cos\left(\frac{l\pi z}{L_z}\right)+2\sum_{n=1}^{\infty}\Omega(0,n,0)\cos\left(\frac{n\pi y}{L_y}\right)\\+2\sum_{m=1}^{\infty}\Omega(m,0,0)\cos\left(\frac{m\pi x}{L_x}\right)+4\sum_{l=1}^{\infty}\sum_{n=1}^{\infty}\Omega(0,n,l)\cos\left(\frac{l\pi z}{L_z}\right)\cos\left(\frac{n\pi y}{L_y}\right)\\+4\sum_{l=1}^{\infty}\sum_{m=1}^{\infty}\Omega(m,0,l)\cos\left(\frac{l\pi z}{L_z}\right)\cos\left(\frac{m\pi x}{L_x}\right)\\+4\sum_{n=1}^{\infty}\sum_{m=1}^{\infty}\Omega(m,n,0)\cos\left(\frac{n\pi y}{L_y}\right)\cos\left(\frac{m\pi x}{L_x}\right)\\+8\sum_{l=1}^{\infty}\sum_{n=1}^{\infty}\sum_{m=1}^{\infty}\Omega(m,n,l)\cos\left(\frac{l\pi z}{L_z}\right)\cos\left(\frac{n\pi y}{L_y}\right)\cos\left(\frac{m\pi x}{L_x}\right)\end{array}\right]$$

..... (A-15)

When the transformations eliminate three coordinates and one of the boundaries represents a Dirichlet (constant pressure) condition, the original primary variable ψ is obtained from the inverse FCT that is described by the following equation:

$$\psi(x,y,z)=\frac{2}{L_xL_yL_z}\left[\begin{array}{l}\displaystyle\sum_{m=1}^{\infty}\Omega(m,0,0)\cos\left(\frac{(2m-1)\pi x'}{2L_x}\right)\\ \displaystyle+2\sum_{l=1}^{\infty}\sum_{m=1}^{\infty}\Omega(m,0,l)\cos\left(\frac{l\pi z}{L_z}\right)\cos\left(\frac{(2m-1)\pi x'}{2L_x}\right)\\ \displaystyle+2\sum_{n=1}^{\infty}\sum_{m=1}^{\infty}\Omega(m,n,0)\cos\left(\frac{n\pi y}{L_y}\right)\cos\left(\frac{(2m-1)\pi x'}{2L_x}\right)\\ \displaystyle+4\sum_{l=1}^{\infty}\sum_{n=1}^{\infty}\sum_{m=1}^{\infty}\Omega(m,n,l)\cos\left(\frac{l\pi z}{L_z}\right)\cos\left(\frac{n\pi y}{L_y}\right)\cos\left(\frac{(2m-1)\pi x'}{2L_x}\right)\end{array}\right]$$

..... (A-16)

Note that, for the sake of simplicity, time (through the Laplace space parameter *s*) is not included in Eq. A-14 to A-16.

A.5 Nomenclature

L_{d°	=	total stencil's length in the *d*°-direction, m
l	=	integer FCT parameter associated with the z-coordinate
m	=	integer FCT parameter associated with the x-coordinate
n	=	integer FCT parameter associated with the y-coordinate
Q	=	production flux, kg/s/m^2
$\hat{Q}$	=	$\mathcal{F}_{c1,z}\{Q\}$
$\hat{\hat{Q}}$	=	$\mathcal{F}_{c1,y}\left\{\mathcal{F}_{c1,z}\{Q\}\right\}$

x = Cartesian coordinates, m

x' = $L_x - x$, m

y = Cartesian coordinates, m

z = Cartesian coordinates, m

θ = $\mathcal{F}_{c1,x}\{\psi\}$

θ' = $\mathcal{F}_{c2,x}\{\psi\}$

φ = $\mathcal{F}_{c1,y}\left\{\mathcal{F}_{c1,z}\{\psi\}\right\}$

Ω = $\mathcal{F}_{ci,x}\left\{\mathcal{F}_{c1,y}\left\{\mathcal{F}_{c1,z}\{\psi\}\right\}\right\}$ $(i=1,2)$

APPENDIX B

TDM SOLUTIONS IN A SYSTEM WITH HETEROGENEOUS SUBDOMAINS

This appendix discussed the approach of both TDM and PTDM in dealing with a system comprising heterogeneous subdomains. In PTDM, the system with heterogeneous subdomains can be easily handled with the single-dimension discretization involved in the PTD-1D option. This allows the seamless description of the heterogeneous subdomain by using the formation properties related to each subdomain. The behavior of PTDM with heterogeneous subdomain had been demonstrated in Case 5 of Section 3.4.

On the other hand, TDM solutions eliminate all spatial discretization. In systems exhibiting heterogeneity along a single dimension, the spatial discretization of the TDM solutions is limited to the number of the subdomains. In that case, ODEs and the corresponding analytical solutions in space are developed for each individual (heterogeneous) subdomain. The following section demonstrates the development of the subdomain-specific ODE approach in the TDM Decomposition stage when dealing with a system with heterogeneous subdomains.

B.1 TDM Decomposition Stage, Step 4 – The ODE Approach in a System with Heterogeneous Subdomain

If there a subdomain with different properties (*e.g.,* an SRV subdomain) that divides the length X of the stencil into two subdomains with lengths X_1 and X_2 ($X = X_1 + X_2$),

respectively, then Eq. 2.30 in section 2.3 applies to both subdomains, with the solutions of the two subdomain 1 and 2 being

$$\Phi_1 = B_{11}\exp\left(\sqrt{A_1}\,x_1\right) + B_{12}\exp\left(-\sqrt{A_1}\,x_1\right) \quad \text{(B-1)}$$

and

$$\Phi_2 = B_{21}\exp\left(\sqrt{A_2}\,x_2\right) + B_{22}\exp\left(-\sqrt{A_2}\,x_2\right) \quad \text{(B-2)}$$

where x_1, x_2 are the local x-coordinates in subdomains 1 and 2, respectively, and B_{11}, B_{21}, B_{21} and B_{21} are parameters to be determined. The derivatives of Φ_1 and Φ_2 are:

$$\frac{d\Phi_1}{dx_1} = \sqrt{A_1}\left[B_{11}\exp\left(\sqrt{A_1}\,x_1\right) - B_{12}\exp\left(-\sqrt{A_1}\,x_1\right)\right] \quad \text{(B-3)}$$

and

$$\frac{d\Phi_2}{dx_2} = \sqrt{A_2}\left[B_{21}\exp\left(\sqrt{A_2}\,x_2\right) - B_{22}\exp\left(-\sqrt{A_2}\,x_2\right)\right] \quad \text{(B-4)}$$

The Neuman conditions at the $x_2 = X_2$ boundary (the midpoint between fractures) necessitate that

$$\Phi_2\left(x_2 = X_2\right) = B_{21}\exp\left(\sqrt{A_2}\,X_2\right) + B_{22}\exp\left(-\sqrt{A_2}\,X_2\right) = 0 \quad \text{(B-5)}$$

from which

$$B_{21} = B_{22}\exp\left(-2\sqrt{A_2}\,X_2\right) or\ \ B_{22} = B_{21}\exp\left(2\sqrt{A_2}\,X_2\right) \quad \text{(B-6)}$$

At the boundary between subdomains 1 and 2, the equality of pressures and fluxes dictate that

$$B_{11}\exp\left(\sqrt{A_1}\,X_1\right)+B_{12}\exp\left(-\sqrt{A_1}\,X_1\right)=B_{21}+B_{22} \quad \text{(B-7)}$$

and

$$B_{11}\exp\left(\sqrt{A_1}\,X_1\right)-B_{12}\exp\left(-\sqrt{A_1}\,X_1\right)=\xi\left(B_{21}-B_{22}\right) \quad \text{(B-8)}$$

where

$$\xi=\frac{k_{x2}}{k_{x1}}\sqrt{\frac{A_2}{A_1}} \quad \text{(B-9)}$$

B.1.1 Dirichlet Conditions (Prescribed $P_{x=0}$) at $\boldsymbol{x}_1=0$, Finite No-Flow Boundary at

$$\boldsymbol{x}_2=\pm\boldsymbol{X}_2$$

For an internal stencil, prescribed (constant or time-variable) Dirichlet conditions at the local $x_1 = 0$ boundary (the hydraulic fracture), Eq. B-1 impose that

$$B_{11}+B_{12}=\ \Phi_1\left(x_1=0\right)\ \Rightarrow\ B_{12}=\Phi_1\left(x_1=0\right)-B_{11} \quad \text{(B-10)}$$

Substitution of B_{12} and B_{21} or B_{22} (Eqs. B-6 and B-23) into Eqs. B-7 and B-8 yields:

$$G_1B_{11}+\mathrm{G}_{2\mathrm{A}}B_{22}=H_1 \quad \text{and} \quad G_3B_{11}+\mathrm{G}_{4\mathrm{A}}B_{22}=H_2 \quad \text{(B-11)}$$

or

$$G_1B_{11}+\mathrm{G}_{2\mathrm{B}}B_{21}=H_1 \quad \text{and} \quad G_3B_{11}+\mathrm{G}_{4\mathrm{B}}B_{21}=H_2 \quad \text{(B-12)}$$

from which

$$B_{11}=\frac{H_1\mathrm{G}_{4\mathrm{A}}-H_2\mathrm{G}_{2\mathrm{A}}}{G_1G_{4A}-G_3G_{2A}} \text{ and } \quad B_{22}=\frac{H_2\mathrm{G}_1-H_1\mathrm{G}_3}{G_1G_{4A}-G_3G_{2A}} \quad \text{(B-13)}$$

or

$$B_{11} = \frac{H_1 G_{4B} - H_2 G_{2B}}{G_1 G_{4B} - G_3 G_{2B}} \text{ and } B_{21} = \frac{H_2 G_1 - H_1 G_3}{G_1 G_{4B} - G_3 G_{2B}} \quad \text{(B-14)}$$

where

$$G_1 = \exp\left(\sqrt{A_1} X_1\right) - \exp\left(-\sqrt{A_1} X_1\right) \quad \text{(B-15)}$$

$$G_{2A} = -\left[\exp\left(-2\sqrt{A_2} X_2\right) + 1\right] \quad \text{(B-16)}$$

$$G_{2B} = -\left[1 + \exp\left(2\sqrt{A_2} X_2\right)\right] \quad \text{(B-17)}$$

$$G_3 = \exp\left(\sqrt{A_1} X_1\right) + \exp\left(-\sqrt{A_1} X_1\right) \quad \text{(B-18)}$$

$$G_{4A} = -\xi\left[\exp\left(-2\sqrt{A_2} X_2\right) - 1\right] \quad \text{(B-19)}$$

$$G_{4B} = -\xi\left[1 - \exp\left(2\sqrt{A_2} X_2\right)\right] \quad \text{(B-20)}$$

$$H_1 = -\left(\Phi_1\left(x_1 = 0\right)\right)\exp\left(-\sqrt{A_1} X_1\right) = -H_2 \quad \text{(B-21)}$$

Knowledge of the B_{ij} ($i, j = 1,2$) coefficients allows the estimation of Φ at any point x in the domain through the application of (a) Eqs. B-1 and B-2 and (b) the use of the local variables x_1 and/or x_2.

Estimation of the flux at the $x_1 = 0$ boundary (= the oil production rate) is obtained from the application of Eqs. 2.26 and 2.31 as

$$\ddot{Q}_{x_1=0} = \lambda_{x_1} \rho_0 \left(\frac{\partial \Phi_1}{\partial x_1}\right)_{x_1=0} = \left(\lambda_{x_1} \rho_0\right) \sqrt{A_1} \left(B_{11} - B_{12}\right) \quad \text{(B-22)}$$

B.1.2 Dirichlet Conditions (Prescribed $P_{x=0}$) at $\boldsymbol{x}_1 = 0$, infinite $\boldsymbol{x}_2 \to \pm\infty$ boundary

Eq. B-5 dictates that $B_{21} = 0$ for $X_2 \to \infty$, in which case $\exp\left(-2\sqrt{A_2}X_2\right) = 0$. Then, Eq. B-13 needs to be used, and applies unchanged but with $G_{2A} = -1$ and $G_{4A} = \xi$.

Conversely, when $X_2 \to -\infty$, $\exp\left(2\sqrt{A_2}X_2\right) = 0$, Eq. B-14 needs to be used, and applies unchanged but with $G_{2B} = -1$ and $G_{4B} = -\xi$. Note that in this case $0 \geq x_1 \geq X_1$ and $0 \geq x_2 \geq X_2$, *i.e.*, the x-coordinates in the two subdomains have all negative values.

B.1.3 Neuman Conditions (Prescribed Q) at $\boldsymbol{x}_1 = 0$, Finite No-Flow Boundary at

$$\boldsymbol{x}_2 = \pm \boldsymbol{X}_2$$

For an internal stencil, for prescribed (constant or time-variable) Neuman conditions at the $x = 0$ boundary, Eqs. 2.26 and 2.31 impose that

$$B_{11} - B_{12} = \frac{\ddot{\boldsymbol{Q}}_{x_1=0}}{\lambda_{x_1}\rho_0\sqrt{A_1}} = D_1 \Rightarrow B_{12} = B_{11} - D_1 \quad \text{(B-23)}$$

Substitution of B_{12} and B_{22} (Eqs. 2.36 and 2.33) into Eqs: B-7 and B-8 yields:

$$G_3 B_{11} + G_{2A} B_{22} = H_3 \quad \text{and} \quad G_1 B_{11} + G_{4A} B_{22} = H_4 \quad \text{(B-24)}$$

or

$$G_3 B_{11} + G_{2B} B_{21} = H_3 \quad \text{and} \quad G_1 B_{11} + G_{4B} B_{21} = H_4 \quad \text{(B-25)}$$

from which

$$B_{11} = \frac{H_3 G_{4A} - H_4 G_{2A}}{G_3 G_{4A} - G_1 G_{2A}} \text{ and } B_{22} = \frac{H_4 G_3 - H_3 G_1}{G_3 G_{4A} - G_1 G_{2A}} \quad \text{(B-26)}$$

or

$$B_{11} = \frac{H_3 G_{4B} - H_4 G_{2B}}{G_3 G_{4B} - G_1 G_{2B}} \text{ and } B_{21} = \frac{H_4 G_3 - H_3 G_1}{G_3 G_{4B} - G_1 G_{2B}} \quad \text{..... (B-27)}$$

where

$$H_3 = -D_1 \exp\left(-\sqrt{A_1} X_1\right) = -H_4 \quad \text{..... (B-28)}$$

and all other terms are as defined earlier.

B.1.4 Neuman Conditions (Prescribed Q) at $x_1 = 0$, $x_2 \to \pm\infty$ boundary

As discussed in Dirichlet conditions – infinite boundary, these conditions describe an edge stencil associated with the last horizontal fracture ($X_2 \to \infty$, *i.e.*, the RIB) or the first horizontal fracture ($X_2 \to -\infty$, *i.e.*, the LIB). The approach to be followed is exactly analogous to that discussed earlier. As before, Eq. B-5 dictates that $B_{21} = 0$ for $X_2 \to \infty$, in which case $exp\left(-2\sqrt{A_2} X_2\right) = 0$. Then, Eq. B-26 needs to be used, and applies unchanged but with $G_{2A} = -1$ and $G_{4A} = \xi$.

Conversely, when $X_2 \to -\infty$, $exp\left(2\sqrt{A_2} X_2\right) = 0$, Eq. B-27 needs to be used, and applies unchanged but with $G_{2B} = -1$ and $G_{4B} = -\xi$. Note that in this case $0 \geq x_1 \geq X_1$ and $0 \geq x_2 \geq X_2$, *i.e.*, the x-coordinates in the two subdomains have all negative values.

B.2 Nomenclature

X_1 = first subdomain (near fracture) total length in the *x*-direction, m

X_2 = second subdomain (away from fracture) total length in the *x*-direction, m

k_x = intrinsic permeability in the *x*-direction, m^2

l = integer FCT parameter associated with the z-coordinate

λ = as defined by Eq. 2.1

m = integer FCT parameter associated with the x-coordinate

n = integer FCT parameter associated with the y-coordinate

Q = production flux, $kg/s/m^2$

$\mathcal{Q}$ = $\mathcal{L}\{Q\}$

$\dot{\mathcal{Q}}$ = $\mathcal{F}_{c1}\{\mathcal{Q}\}$

$\ddot{\mathcal{Q}}$ = $\mathcal{F}_{c1}\{\dot{\mathcal{Q}}\}$

ρ = fluid density, kg/m^3

x = Cartesian coordinates, m

x' = $L_x - x$, m

y = Cartesian coordinates, m

z = Cartesian coordinates, m

Ω_i = $\mathcal{F}_{ci,x}\{\mathcal{F}_{c1,y}\{\mathcal{F}_{c1,z}\{\Psi\}\}\}$ $(i=1,2)$

1 = subscript for first subdomain (near fracture)

2 = subscript for second subdomain (away from fracture)

APPENDIX C

TDM RECONSTRUCTION STAGE – OPTIONS FOR THE INVERSION OF THE LAPLACE SPACE SOLUTION

Here we discuss the two different methods that can be used in the TDM Reconstruction stage in order to convert the Laplace-space solutions back to real-space solutions (Referred to Step R4 in section 2.3). The two methods that we will discuss is (1) Stehfest Method or StA (Stehfest, 1970a;b) and (2) DeHoog Method or DHM (DeHoog et al.,1982).

C.1 TDM Reconstruction Stage, Step 4 – The Inversion of the Laplace Space Solution

The inversion of any Laplace space solution $\Psi(x,y,z,s)$ from TDM Step R3 is accomplished through a numerical process that is based on one of the following two methods. The first is the Stehfest algorithm (Stehfest, 1970a;b). The Stehfest algorithm is a simple and computationally efficient method, and is widely used for inversion of Laplace space equations to yield solutions in time.

C.1.1 The Stehfest Algorithm

The Stehfest algorithm can be described as follows

$$\delta = \delta(x,y,z,t) = \mathcal{L}^{-1}\left\{\Psi(x,y,z,s)\right\} = \frac{\ln(2)}{t}\sum_{v=1}^{2N_s} W_v \Psi_v(x,y,z,s_v) \quad \text{..... (C-1)}$$

where $\mathcal{L}^{-1}\{\}$ denotes the inverse Laplace transform of the quantity within the brackets,

$$s_v = \frac{\ln(2)}{t} v \quad \text{..... (C-2)}$$

$$W_v = (-1)^{v+N_s} \sum_{\kappa=(v+1)/2}^{\min(v,N_s)} \frac{\kappa^{N_s}(2\kappa!)}{(N_s-\kappa)!\kappa!(\kappa-1)!(v-\kappa)!(2\kappa-v)!} \quad \text{..... (C-3)}$$

and $5 \leq N_S \leq 10$ (Moridis et al., 1994).

The Stehfest algorithm will work as long as the real space solution $\delta(x, y, z, t)$ is a continuous function on $t \in (0, \infty)$. The accuracy of the inversion depends on the number of terms (N_s) used for the inversion process. Using different values of N_s as an input affects the inversion results. Moridis and Reddell (1991a) reported that the method seems insensitive to N_s for $6 \leq N_s \leq 10$ in the solution of the problem of liquid flow through porous media using double-precision arithmetic. In this study, we tested a range of N_s values to arrive at the recommended value of $N_s = 8$.

As mentioned that the Stehfest algorithm works for continuous function on $t \in (0, \infty)$. The method may exhibit limitations in the accuracy of the inversion for particularly steep or complex functions (Moridis et al., 1999), as well as step-functions. When the boundary conditions are steep functions of time (*e.g.*, step-wise changes in the flow rate or the bottomhole pressure), the method of DeHoog et al. (1982) is the recommended option.

C.1.2 The DeHoog Method

DeHoog Method is a very robust Laplace inversion method that has been shown to be very effective in practically any kind of inversion problem, providing very accurate solutions in the inversion even of some of the most complex functions with steep fronts (such as step-functions). Although the process is more complicated than in the case of StA (as it requires the computation of complex numbers), the method is more accurate, more versatile and can provide solutions over a wide time period using a single set of computed parameters (as opposed to StA, which requires different computations for a solution at any time).

In DHM, *s* is a complex number given by Crump (1976) as

$$s_v = s_0 + \frac{v\pi}{T} i_c, \quad s_0 = \mu_H - \frac{\ln(E_R)}{2T}, \quad v = 1, 2, \ldots, N_H \quad \text{..... (C-4)}$$

where $2T$ is the period of the Fourier series approximating the inverse function in the interval $[0, 2T]$, $i_c = \sqrt{-1}$, and $N_H = 2M_H + 1$ is an odd number. Moridis (1992) showed that very accurate solutions were obtained when $\mu_H = 0$, $10^{-12} \le E_R \le 10^{-9}$, and $0.9t_{max} \le T \le 1.1t_{max}$, where t_{max} is the point in time or space at which a solution is required. Moridis (1992) determined that the minimum M_H for an acceptable accuracy is 5, and that an accuracy comparable to that for the StA is obtained for $M_H \ge 6$. A unique advantage of the DHG method is that it can yield solutions at any time *t* over the entire

range of [0.2T, T] from a single set of the DHM parameters (Moridis, 1992; Moridis and Kansa, 1994), *i.e.*, these do not need to be recomputed at any t (as is the case in the StA).

The inversion of the Laplace space solution obtained using the DHM is a more complicated process than that for the StA, is outside the scope of this study and will not be discussed in detail here. The interested reader is directed to the paper of DeHoog et al. (1982) for a thorough description.

C.2 Sensitivity Analysis of the Laplace Inversion's Computational Parameters

Both the StA and the DHM are numerical methods that yield solutions by computing a finite series of terms. The number of the summation terms in the series can (and will) affect the accuracy of the inversion. The discussion on StA and DHM in the previous sections already include discussions on recommendation for the number of terms (N_s and M_H for the StA and the DHM, respectively) based on earlier studies.

Thus, according to Moridis et al. (1994), the suitable range of N_s are integer between 5 to 10. In this study, after testing we used a value of $N_s = 8$ in the study of all TDM cases. Moridis et al. (1999) recommended a value of $M_H \geq 10$ in DHM inversions. In this study, we used a value of $M_H = 10$ in the solution of most TDM problems, except in the TDM Case 8 (in which p_{wf} is time-dependent in the stepwise-constant manner described by **Fig. 2.25**) where we used a $M_H = 14$.

This section presents results of a sensitivity analysis of the effect of the summation terms on the accuracy of the calculated solutions. In order to evaluate N_s, we computed the average deviation between the TD-1D and the FTSim solutions in the validation problem in Case 2 (constant pressure p_{wf} at x = 0 or a Dirichlet-type boundary). The sensitivity results in **Fig. C-1** show an excellent agreement of the two solutions for $5 \leq N_S \leq 10$, consistent with the Moridis et al. (1994) recommendation. A value of N_s = 4 gives a substantially higher deviation, and the solutions for N_s = 11 are divergent and clearly inaccurate. In conclusion, a value of N_s = 8 yields consistently good results and is used in all TDM solutions in this study.

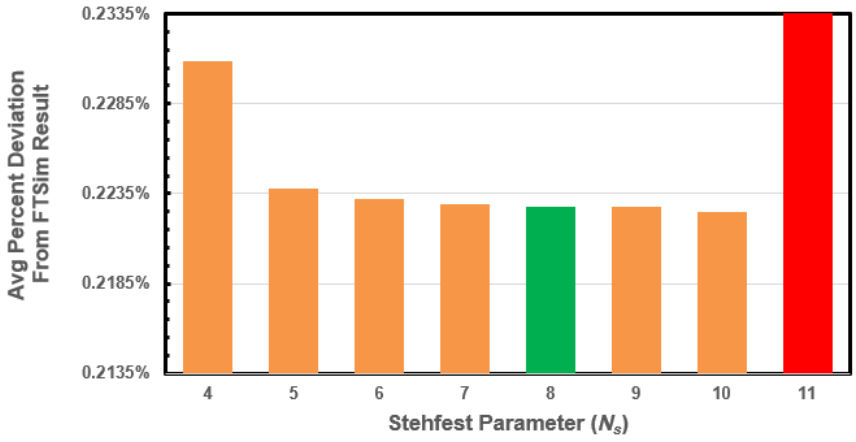

Figure C-1 — Case 2: Average Percent Deviation of the TD-1D-StA solutions from the FTSim using different Stehfest Parameter (N_s) for constant-pressure production p_{wf} (Red denotes inaccurate solutions and Green the recommended value)

We evaluated the effect of M_H on the accuracy of the inversion by computing the average deviation between the TD-1D and the FTSim solutions in Case 8 (in which p_{wf} is time-dependent in the stepwise-constant manner described by **Fig. 2.25**). The sensitivity results in **Fig. C-2** show an excellent agreement between the two solutions for a value of $M_H \geq 10$, consistent with the Moridis et al. (1999) recommendation. Significant deviations are observed for $M_H = 8$ and 9. Note that, unlike StA, the accuracy of the DHM inversions increases monotonically (albeit slowly) by increasing the number of the summation terms M_H, as Fig.C-2 confirms. Based on these results, we used a value of $M_H = 10$ in all but one (to be discussed later) of the TDM inversions in this study. A larger M_H would yield a more accurate solution, but would also require longer execution times with a marginal improvement in accuracy.

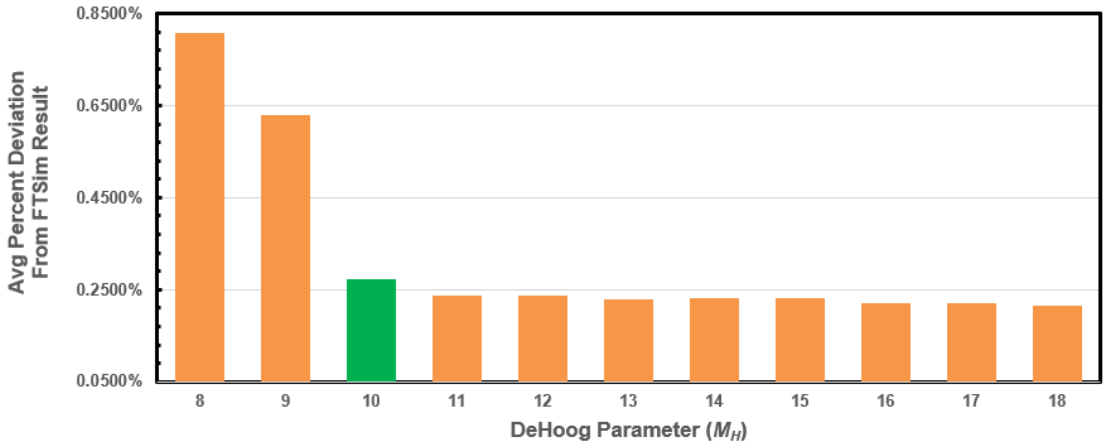

Figure C-2 — Case 8: Average Percent Deviation of the TD-1D-StA solutions from the FTSim using different DeHoog Parameter (M_H) for the step-wise boundary pressure p_{wf} (Green denotes the recommended value)

Although M_H = 10 provides sufficiently accurate results in most general cases involving smooth time-dependent boundary conditions and solution surfaces, it is inadequate in cases involving steep fronts and sharp changes in the boundary conditions. In that case, a higher M_H is recommended. For example, M_H = 14 is recommended in order to accurately capture the spikes in the production rate in Case 8 (**Fig. 2.27**), in which the time-dependent bottomhole pressure p_{wf} is described by the stepwise-constant regime described by **Fig. 2.25**. **Figs. C-3 to C-8** show the evolution of the production rate q calculated using the FTSim simulator and the TD-1D solutions obtained with the DHM Laplace inversion and M_H values ranging from 8 to 18. The results show that the FTSim results with fine temporal discretization are matched well by the TD-1D solution with the DHM inversion when $M_H \geq 14$ (and acceptably so when M_H = 12). The TD-1D results for $M_H < 12$ are demonstrably inaccurate, and the improvements in the solution for $M_H > 14$ are not discernible to the naked eye.

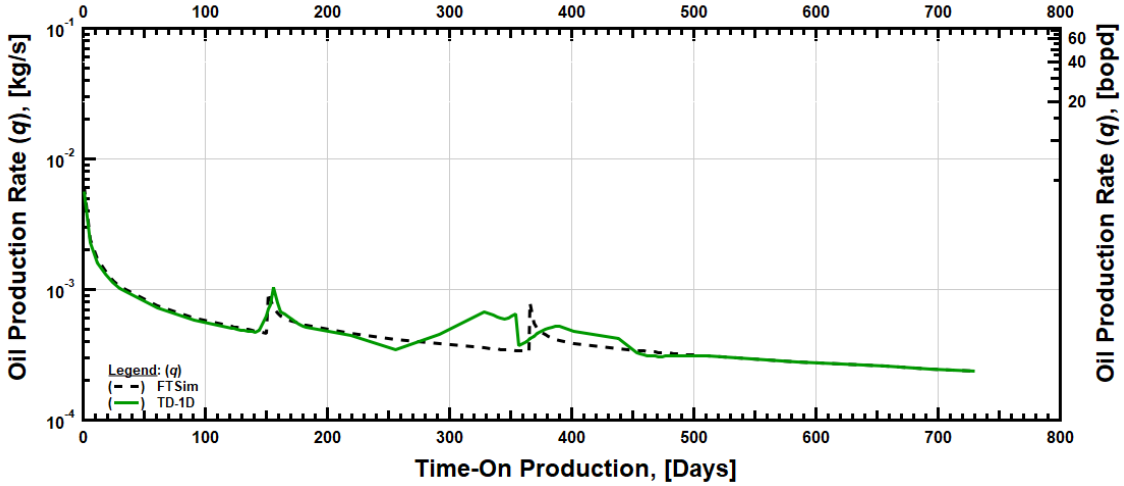

Figure C-3 — Case 8: Evolution of the production rate q over time at $x = 0$ for the step-wise boundary pressure p_{wf} : comparison of the FTSim and TD-1D-DHM with $M_H = 8$.

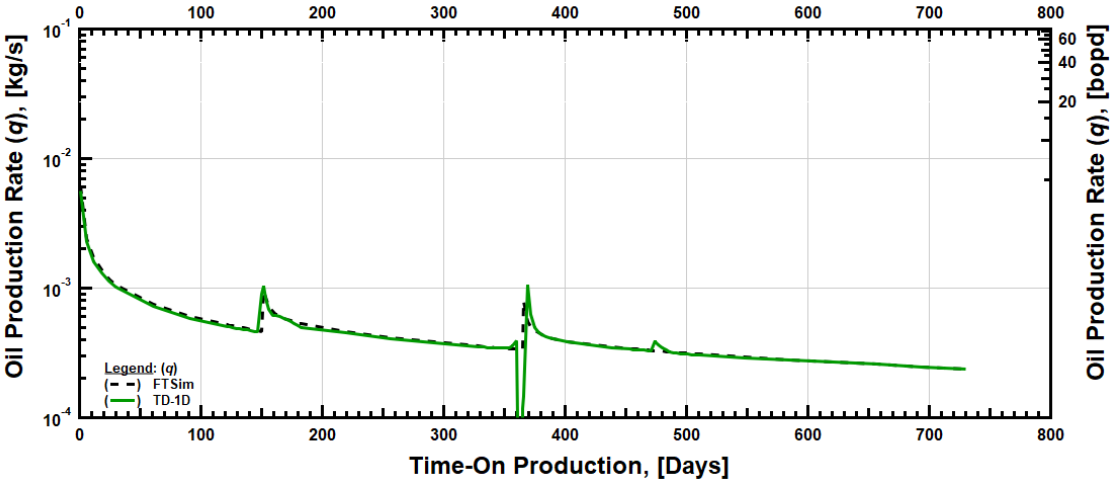

Figure C-4 — Case 8: Evolution of the production rate q over time at $x = 0$ for the step-wise boundary pressure p_{wf} : comparison of the FTSim and TD-1D-DHM with $M_H = 10$.

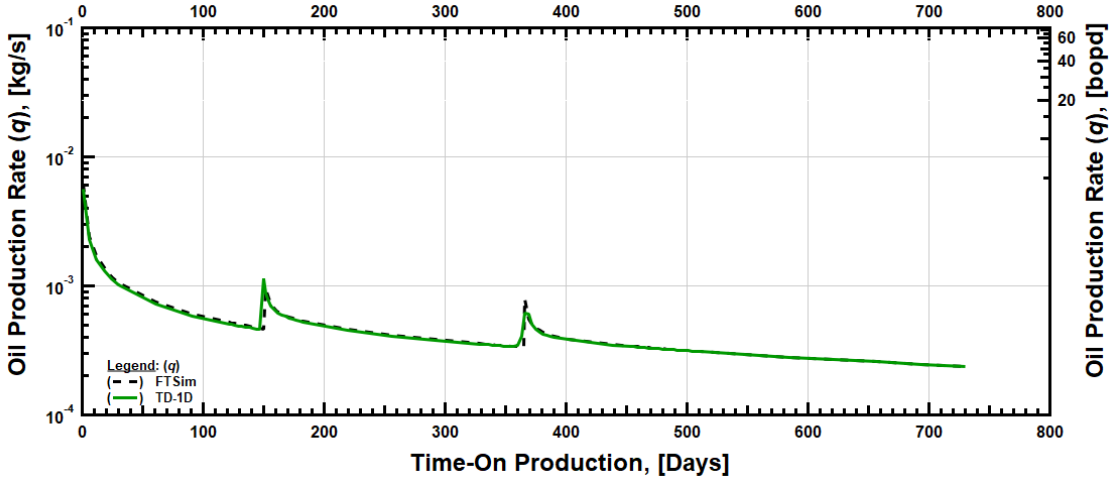

Figure C-5 — Case 8: Evolution of the production rate q over time at $x = 0$ for the step-wise boundary pressure p_{wf} : comparison of the FTSim and TD-1D-DHM with $M_H = 12$.

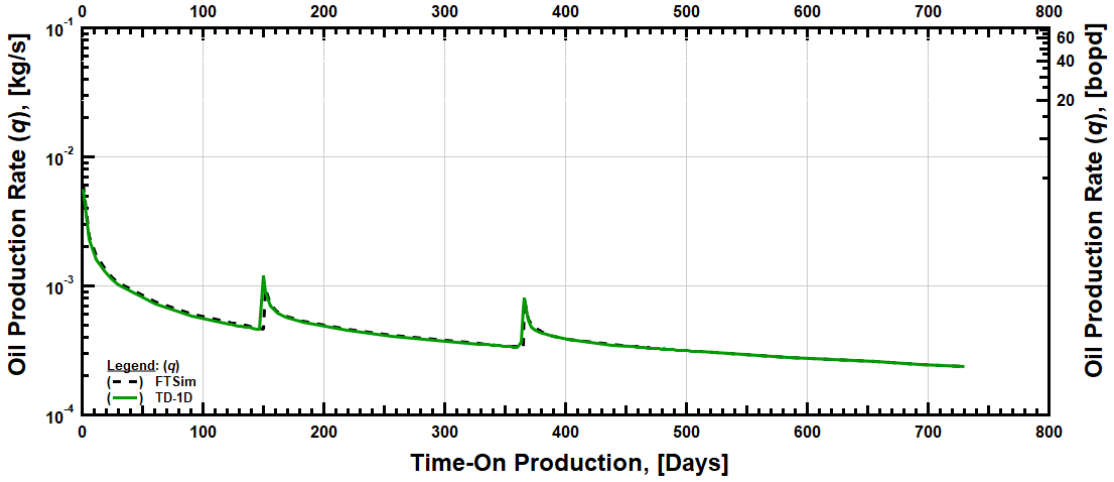

Figure C-6 — Case 8: Evolution of the production rate q over time at $x = 0$ for the step-wise boundary pressure p_{wf} : comparison of the FTSim and TD-1D-DHM with $M_H = 14$.

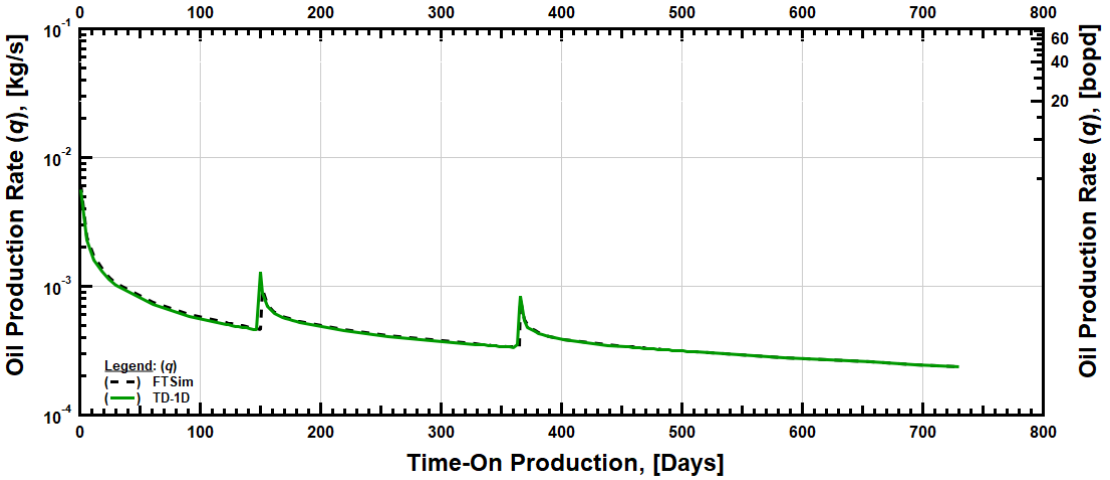

Figure C-7 — Case 8: Evolution of the production rate q over time at $x = 0$ for the step-wise boundary pressure p_{wf} : comparison of the FTSim and TD-1D-DHM with $M_H = 16$.

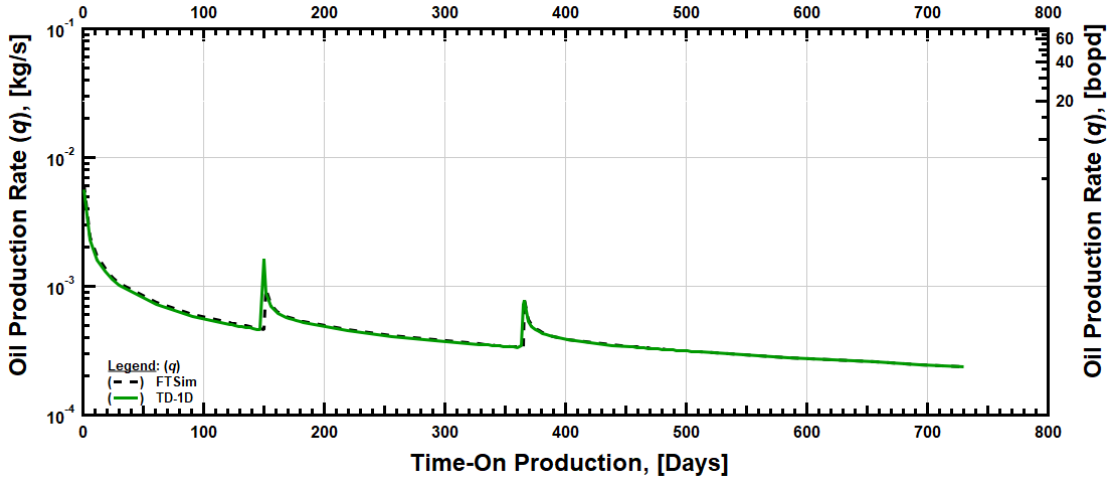

Figure C-8 — Case 8: Evolution of the production rate q over time at $x = 0$ for the step-wise boundary pressure p_{wf} : comparison of the FTSim and TD-1D-DHM with $M_H = 18$.

C.3 Nomenclature

$\mathcal{L}\{\}$	=	denotes the Laplace transform of the quantity within the brackets
$\mathcal{L}^{-1}\{\}$	=	denotes the inverse Laplace transform of the quantity within the brackets
M_H	=	Number of terms for DeHoog Laplace inversion
N_s	=	Number of terms for Stehfest Laplace inversion
P,p	=	pressure, Pa
p_{wf}	=	bottomhole pressure at HF, Pa
q	=	production rate, kg/s
s	=	Laplace space parameter, see Eq. C-2 or C-4
t	=	time, sec
x	=	Cartesian coordinates, m
y	=	Cartesian coordinates, m
z	=	Cartesian coordinates, m